



저작자표시-비영리-변경금지 2.0 대한민국

이용자는 아래의 조건을 따르는 경우에 한하여 자유롭게

- 이 저작물을 복제, 배포, 전송, 전시, 공연 및 방송할 수 있습니다.

다음과 같은 조건을 따라야 합니다:



저작자표시. 귀하는 원저작자를 표시하여야 합니다.



비영리. 귀하는 이 저작물을 영리 목적으로 이용할 수 없습니다.



변경금지. 귀하는 이 저작물을 개작, 변형 또는 가공할 수 없습니다.

- 귀하는, 이 저작물의 재이용이나 배포의 경우, 이 저작물에 적용된 이용허락조건을 명확하게 나타내어야 합니다.
- 저작권자로부터 별도의 허가를 받으면 이러한 조건들은 적용되지 않습니다.

저작권법에 따른 이용자의 권리는 위의 내용에 의하여 영향을 받지 않습니다.

이것은 [이용허락규약\(Legal Code\)](#)을 이해하기 쉽게 요약한 것입니다.

[Disclaimer](#)

Doctoral Thesis

A Wearable Control Interface
for Tele-operated Robots

Yeongtae Jung

Department of Mechanical Engineering

Graduate School of UNIST

2019

A Wearable Control Interface for Tele-operated Robots

Yeongtae Jung

Department of Mechanical Engineering

Graduate School of UNIST

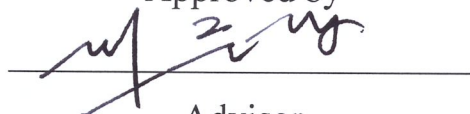
A Wearable Control Interface for Tele-operated Robots

A thesis/dissertation
submitted to the Graduate School of UNIST
in partial fulfillment of the
requirements for the degree of
Doctor of Philosophy

Yeongtae Jung

12/05/2018

Approved by



Advisor

Joonbum Bae

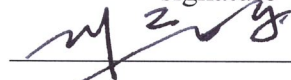
A Wearable Control Interface for Tele-operated Robots

Yeongtae Jung

This certifies that the thesis/dissertation of Yeongtae Jung is approved.

12/05/2018

signature



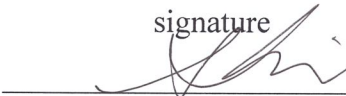
Advisor: Joonbum Bae

signature



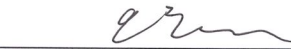
Hungsun Son

signature



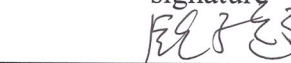
Gwanseob Shin

signature



Hyondong Oh

signature



Tsz-Chiu Au

Abstract

This thesis presents a wearable control interface for the intuitive control of tele-operated robots, which aim to overcome the limitations of conventional uni-directional control interfaces. The control interface is composed of a haptic control interface and a tele-operated display system. The haptic control interface can measure user's motion while providing force feedback. Thus, the user can control a tele-operated robot arm by moving his/her arm in desired configurations while feeling the interaction forces between the robot and the environment. Immersive visual feedback is provided to the user with the tele-operated display system and a predictive display algorithm.

An exoskeleton structure was designed as a candidate of the control interface structure considering the workspace and anatomy of the human arm to ensure natural movement. The translational motion of human shoulder joint and the singularity problem of exoskeleton structures were addressed by the tilted and vertically translating shoulder joint. The proposed design was analyzed using forward and inverse kinematics methods. Because the shoulder elevation affects all of the joint angles, the angles were calculated by applying an inverse kinematics method in an iterative manner. The proposed design was tested in experiments with a kinematic prototype.

Two force-controllable cable-driven actuation mechanisms were developed for the actuation of haptic control interfaces. The mechanisms were designed to have lightweight and compact structures for high haptic transparency. One mechanism is an asymmetric cable-driven mechanism that can simplify the cable routing structure by replacing a tendon to a linear spring, which act as an antagonistic force source to the other tendon. High performance force control was achieved by a rotary series elastic mechanism and a robust controller, which combine a proportional and differential (PD) controller optimized by a linear quadratic (LQ) method with a disturbance observer (DOB) and a zero phase error tracking (ZPET) feedforward filter. The other actuation mechanism is a series elastic tendon-sheath actuation mechanism. Unlike previously developed tendon-sheath actuation systems, the proposed mechanism can deliver desired force even in multi-DOF systems by modeling and feedforwardly compensating the friction. The pretension change, which can be a significant threat in the safety of tendon-sheath actuation systems, is reduced by adopting series elastic elements on the motor side. Prototypes of the haptic control interfaces were developed with the proposed actuation mechanisms, and tested in the interaction with a virtual environment or a tele-operation experiment.

Also, a visual feedback system is developed adopting a head mounted display (HMD) to the control interface. Inspired by a kinematic model of a human head-neck complex, a robot neck-camera system was built to capture the field of view in a desired orientation. To reduce the sickness caused by the time-varying bidirectional communication delay and operation delay of the robot neck, a predictive display algorithm was developed based on the kinematic model of the human and robot neck-camera system, and the geometrical model of a camera. The performance of the developed system was tested by experiments with intentional delays.

Contents

1	Introduction	8
1.1	Motivation	8
1.2	State of the Art	10
1.3	Thesis Overview	15
2	Design of an Upper-limb Exoskeleton	17
2.1	Introduction	17
2.2	Design of the 5 DOF Upper-limb Exoskeleton	19
2.2.1	Anatomical Analysis of the Shoulder	19
2.2.2	Singularity of the Upper-limb Exoskeleton	20
2.3	Kinematic Analysis	23
2.3.1	Forward Kinematics Analysis: DH Parameter	24
2.3.2	Iterative Inverse Kinematics	24
2.4	Performance Verification by Simulation	29
2.4.1	Joint Trajectories	29
2.4.2	Manipulability Analysis	33
2.5	Performance Verification by Experiment	36
2.5.1	Force Analysis	36
2.5.2	Motion Analysis	41
2.6	Summary	41
3	Cable-driven Mechanisms	45
3.1	An Asymmetric Cable-driven Mechanism	45

3.1.1	Introduction	45
3.1.2	Configuration of an Asymmetric Cable-driven Mechanism	46
3.1.2.1	Cable-driven Mechanism	46
3.1.2.2	Spring-actuator Mechanism for Asymmetric Force Requirement	50
3.1.2.3	Rotary Series Elastic Mechanism	50
3.1.2.4	System Configurations	51
3.1.3	Control of the Asymmetric Cable-driven System	51
3.1.3.1	System Modeling	51
3.1.3.2	Controller Design	54
3.1.4	Experimental Verification	58
3.1.4.1	Experimental Setup	58
3.1.4.2	Experimental Verification without Human Interaction	59
3.1.4.3	Experimental Verification with Human Interaction	60
3.2	A Series Elastic Tendon-sheath Actuation Mechanism	69
3.2.1	Introduction	69
3.2.2	Characteristics of a Conventional Tendon-sheath Actuation Mechanism . .	70
3.2.2.1	Analysis	70
3.2.2.2	Simulation	80
3.2.3	Design and Control of a Series Elastic Tendon-sheath Actuation Mechanism	81
3.2.4	Experimental Verifications	85
3.2.4.1	Verification of the Proposed Mechanism	85
3.2.4.2	A Tele-operation Control Interface with the Proposed Mechanism	89
3.3	Summary	98
4	A Display System for Tele-operation	100
4.1	Introduction	100
4.2	Overview of the Display System	104
4.3	A Predictive Algorithm for the Display System	106
4.3.1	A Predictive Display Algorithm	106
4.3.2	Margin Analysis	108
4.4	Experiments	114

4.4.1	Parameter Identification	114
4.4.2	Implementation of the Predictive Display Algorithm	114
4.5	Summary	115
5	Concluding Remarks and Open Issues	116
5.1	Design of Wearable Control Interface Structures	116
5.2	Design and Control of Cable-driven Actuation Mechanisms	117
5.3	A Tele-operated Display System	118
5.4	Issues in Tele-operation	118
	References	120

List of Figures

1-1	Number of natural and man-made disasters.	9
1-2	Concept of the tele-operation system.	10
1-3	End-effector type haptic interfaces.	11
1-4	Exoskeleton type haptic interfaces.	12
2-1	Illustration of the skeletal structure of the shoulder.	19
2-2	Variation of the CGH by arm lifting.	21
2-3	Initial configuration of the upper-limb exoskeleton.	22
2-4	Tilting of the shoulder joint.	23
2-5	Final configuration of the upper-limb exoskeleton.	24
2-6	Geometric relationship of coordinates used for the inverse kinematics.	25
2-7	Flow chart of the iterative inverse kinematics calculation.	30
2-8	Simulation of the kinematic models with and without shoulder elevation.	31
2-9	Joint angles of the fixed or moving shoulder joint models.	32
2-10	Physical interference by extreme tilting angles.	33
2-11	Minimum manipulability of α and β	34
2-12	Change of the singularity position by tilting the shoulder joints.	35
2-13	Manufactured exoskeleton prototype.	37
2-14	Shifted singularity position of the exoskeleton prototype.	38
2-15	Net shoulder elevation and the measured force with the fixed shoulder joint.	39
2-16	Measured forces during arm elevation with the vertically movable shoulder joint.	39
2-17	Statistical analysis of the measured forces during arm elevation.	40
2-18	Performed tasks in the motion capture system.	42
2-19	Height change of each joint.	43
2-20	Statistical analysis of the height change.	44

3-1	Cable-driven mechanisms.	47
3-2	Range of motions of the one actuator mechanism and the spring-actuator type mechanism.	49
3-3	Schematics of the proposed asymmetric cable-driven mechanism.	52
3-4	Determination of u_0 by measured and linearly fitted linear spring length.	55
3-5	Block diagram of the control structure.	55
3-6	Frequency response of the system.	57
3-7	A prototype of the proposed mechanism for the elbow joint.	59
3-8	Frequency response of the system without the torsional spring and human parts.	60
3-9	Position tracking performance without inserting a disturbance.	61
3-10	Position tracking performance and the disturbance observation with a sinusoidal disturbance.	62
3-11	Schematics and parameters for the virtual dumbbell experiment.	63
3-12	Interaction between a robot arm and the exoskeleton.	64
3-13	Backdrivability test of the system.	64
3-14	Torque tracking performance with a human user and a sinusoidal desired torque.	65
3-15	Torque tracking performance of the system in the interaction with a virtual dumbbell.	66
3-16	Torque tracking performance in the interaction with a robot arm.	67
3-17	Configuration of a conventional double-tendon-sheath actuation mechanism and its small element.	72
3-18	A longitudinal cross section of spiral type sheath.	76
3-19	Variations in $\alpha(t) + \beta(t)$ and $ \alpha(t) - \beta(t) $ with changes in $\Theta(t)$ and μ	79
3-20	Simulation results of a double-tendon-sheath actuation system.	79
3-21	Configuration of the proposed mechanism for n-DOFs systems.	81
3-22	Block diagram of the control structure.	83
3-23	A prototype manipulator used to verify the performance of the proposed mechanism.	84
3-24	Identified and modeled friction parameter.	84
3-25	Experimental result in the absence of friction compensation.	87
3-26	Experimental result in the presence friction compensation.	88
3-27	A tele-operation control interface featuring the proposed tendon-sheath actuation mechanism.	90
3-28	Motor torque controller with DOB and ZPET controller.	91

3-29	Back-drivability test results of the tele-operation control interface.	92
3-30	Experimental results obtained during interaction with the virtual walls of the tele-operation control interface.	93
3-31	Experimental settings for the interaction with the virtual walls.	94
3-32	Experimental results with different virtual wall stiffness.	95
3-33	Tele-operation experimental setup.	96
3-34	Interactions with objects that have different stiffness.	97
4-1	Design of a robot neck-camera module based on the kinematic model of human head-neck complex.	101
4-2	Overview of the tele-operated display system.	101
4-3	Simplified camera geometry and image position change of a subject by camera motions	102
4-4	Implementation procedure of the predictive display algorithm	103
4-5	Margin changes by the translation and rotation of the crop area	109
4-6	Experimental setup for the parameter identification	112
4-7	Identification result of camera parameter αd by yaw and pitch motions	112
4-8	Measured network delay	113
4-9	Captured images of the tele-operation experiment	113

List of Tables

2.1	Change of θ_{SC} θ_{AC} by shoulder elevation.	20
2.2	Shoulder range of motion.	23
2.3	DH parameters of the proposed configuration.	25
3.1	Elbow joint torque in flexion and extension.	50
3.2	Specifications of experimental setup.	58
3.3	Root mean square (RMS) errors in the experiments without a user.	61
3.4	Root mean square (RMS) errors in the experiments with a user.	68
3.5	Specifications of the 2-DOFs system	86
4.1	Specifications of the tele-operated display system	105

Chapter 1

Introduction

1.1 Motivation

The number of disasters causing casualties and property damage is increasing [8,9]. Disaster sites are often difficult for humans to access because of the extreme environments, such as in the case of Deepwater Horizon oil spill (2010), Tohoku earthquake and Fukushima nuclear power plant accident (2011) and Tianjin port explosions (2015). Autonomous robots have been researched as an alternative to using human workers in such disaster sites. Despite of drastic improvements over several decades, autonomous robots have not yet shown sufficient performance in working under unstructured and unpredictable situations due to their limited sensing technology and insufficient artificial intelligence.

Tele-operation systems, in which the robot is controlled by human's intelligence, instead of artificial intelligence, may be an alternative solution [10–13]. Tele-operated systems are usually operated in a master-slave mode with simple controllers such as a keyboard or a joystick [10, 11]. However, such non-intuitive control interfaces require long training before using the system, and the performance is also limited even after training because it is difficult to express desired motions with such interfaces. Motion capture systems have been used to utilize the user's motion as the desired motion of the tele-operated robot [12, 13]. By mapping the captured user's motion into the robot's desired motion, the user can control the robot as desired like his/her own body, enhancing the manipulation performance of tele-operated robot. Since the motion capture system and the control strategy is very intuitive and easy to learn, it is quite effective in manipulating objects that does not require advanced interaction force control. However, such uni-directional control strategy limits the performance of the system because force feedback is not provided to the user. Simple tasks

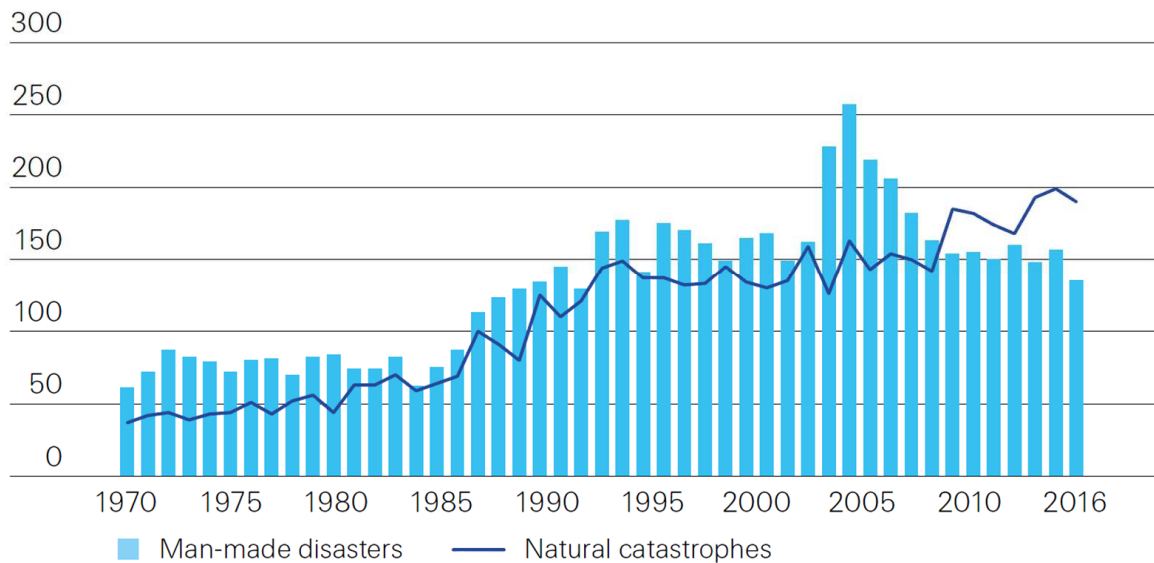


Figure 1-1: Number of natural and man-made disasters [8].

such as 'pick and place' can be easily achieved by position tracking. However, dexterous tasks that require the use of interaction force between the robot and unidentified environment are not easily achievable without detailed interactions between the user and the robot. To enable such tasks, the control interface is required to provide force feedback while measuring user's motion.

Visual feedback is an important feedback as well as the force feedback, since humans highly rely on visual information to get information of the environment. In tele-operated systems, the user observes the field using the images captured by cameras of the robot to control the tele-operated robot. The captured images are typically provided to the user by a monitor in a form of 2D images. However, the performance of tele-operation system is limited in such cases, because the user cannot recognize the distance between objects. 3D visual feedback system with a head mounted display (HMD) and stereo cameras have been used to provide perspective images of the environment [12–14], but delays induced by tele-communication network of the tele-operation system disturb immersive and comfortable use of the system. Such image delay can cause simulator sickness, which makes it difficult to perform tasks for a long time [15–17].

To address these requirements, a wearable control interface is developed for the control of tele-operated robot in this thesis. Fig. 1-2 shows the concept of the tele-operation system using the wearable control interface. The user wears the control interface, which contains the haptic control interface and an HMD. The user's hand position and orientation, and the head orientation are measured by the haptic control interface and the HMD, respectively. The position and orientations

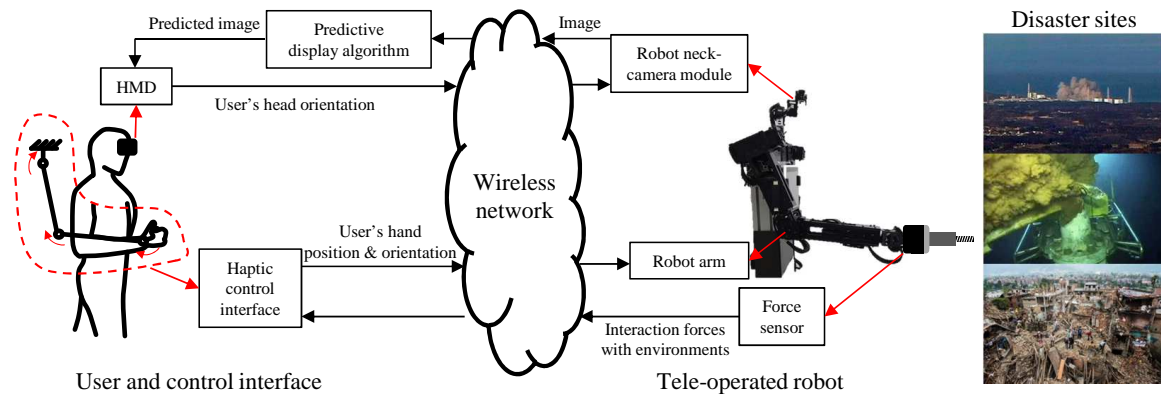


Figure 1-2: Concept of the tele-operation system.

are transmitted to the tele-operated robot via the wireless network. The robot performs tasks by following the user’s motion with the robot arm and robot neck-camera module. The interaction force between the robot and the environment and the vision information captured by a camera in the orientation of user’s head are transmitted to the user side. The user can get force feedback from the haptic control interface. Immersive visual feedback is provided to the user compensating the image delay by a predictive display algorithm. The tele-operation system can perform various tasks with this bidirectional interaction. The haptic control interface, including the kinematic structure and actuation mechanisms, and the tele-operated display system with a predictive display algorithm are developed in this thesis.

1.2 State of the Art

Haptic interfaces have been researched for the tele-operation or for the interaction with virtual environments [18–30]. The performance of tele-operation can be improved by providing force feedback via such haptic interfaces. Fig. 1-3 shows end-effector type haptic interfaces, which provides force feedback to the user’s hands [18–26]. These interfaces can be used as the control interface of tele-operations, since most tasks in tele-operations will be performed by user’s hand. PHANToM haptic interface is a representative commercialized haptic interfaces developed for 3D modeling and design (Fig. 1-3a) [18, 19]. This interface can measure 6-DOF position and orientation of pencil type end-effector and can provide 3-DOF force feedback. Sigma.7, shown in Fig. 1-3b, is a commercialized haptic interface capable of 6-DOF force/torque feedback [20,21] and active grasping capability, designed for the control of surgical robots. Both PHANToM and Sigma.7 are applicable as the control interface of robotic systems, but their applications are limited because of small workspaces. Fig. 1-

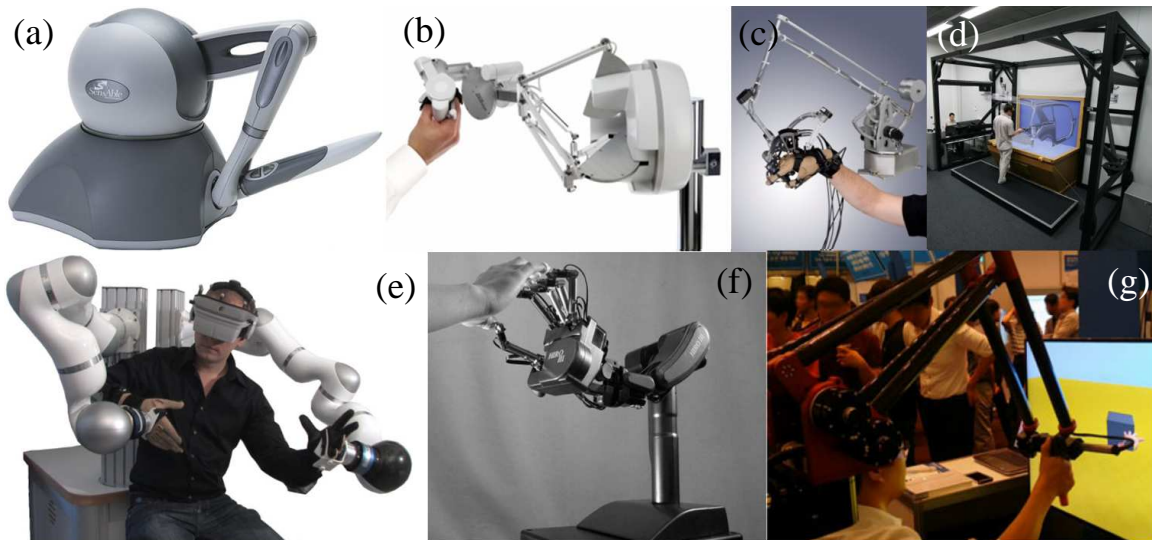


Figure 1-3: End-effector type haptic interfaces. (a) PHANToM haptic interface [18, 19]. (b) Sigma.7 [20, 21]. (c) CyberForce [22]. (d) Inca 6D [23]. (e) DLR haptic device [24]. (f) HIRO III [25]. (g) VirtuaPower [26].

3c shows the CyberForce, which was designed for the interaction with virtual environments [22]. This interface allows 3-DOFs force feedback with 6-DOF position and orientation measurement of user' hand. Force feedback for 5 fingers is also available with a cable(tendon)-driven finger exoskeleton system. It has larger workspace than PHANToM and Sigma.7, but is heavier, which will reduce force transparency. Inca 6D, shown in Fig. 1-3d, was developed for work in virtual reality environments [23]. This interface achieved lightweight of the actuated part compared to the wide workspace, since it adopted parallel cable-driven mechanism and large actuators. However, it required room-size installations to prevent interference between the cables and the user. DLR haptic device, shown in Fig. 1-3e, was developed applying two 7-DOF robot arms [24]. Vibrotactile feedbacks and 3D visual feedbacks are also provided for the immersive interaction with virtual environments or tele-operated robots. User's hands are connected by a set of straps and gloves to the force/torque sensors at the end-effectors of the robot arms. The system provides relatively larger workspace and force capability than those of aforementioned systems, due to large-size redundant robot arms. Fig. 1-3f shows a haptic interface named HIRO III [25]. In this system, five fingertips that have 3 actively controlled joints are connected to a 6-DOF robot arm; thus, the system could provide force feedbacks to each finger. Both DLR haptic device and HIRO III utilized robot arms for the force feedback, but the backlash, friction and large inertia from the geared motors disturb precise force delivery. Fig. 1-3g shows VirtuaPower, which was developed for wide workspace with

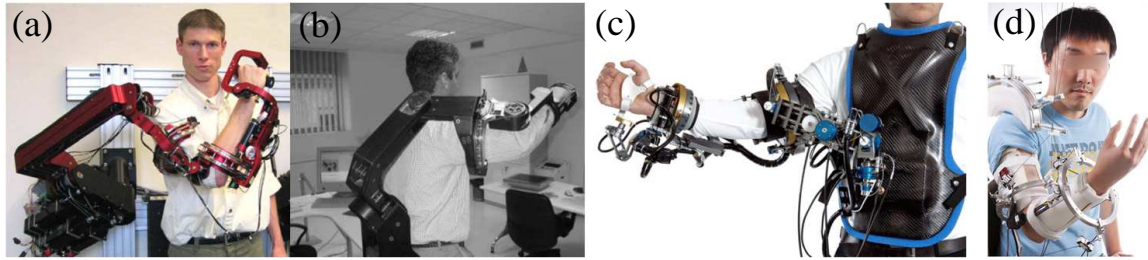


Figure 1-4: Exoskeleton type haptic interfaces. (a) CADEN-7 [27]. (b) L-EXOS [28]. (c) X-Arm-2 [29], (d) CAREX [30].

high force display capability achieved by parallel chain-based kinematic structures and high-power motors with low gear ratio [26]. Although the interface seems somewhat achieved the desired specifications, the user's finger motion is limited since they are required to hold the handle with their fingers.

Aforementioned researches adopted serial or parallel linkage systems that are independent from user's body. Such designs allow users to use device without adjustment regardless to the individual body size difference. Exoskeleton type haptic interfaces have different approach in the design of system. They have been developed by designing joints and links of the interface corresponding to those of human, and attaching them to the user's segments [27–30]. Since exoskeleton systems are placed much closed user's body, compact structure and light weight is required for safety. To satisfy lightweight and compact structure, recently developed exoskeletons have been adopted cable-driven mechanisms. Cable-driven mechanisms can reduce the weight and volume of structure by placing the actuators to the base of the system, rather than the actuated parts. The force or torque can be delivered to the actuated joints via flexible cables. Delivering forces via parallel linkages such as in the PHANToM, CyberForce and VirtuaPower can be an alternative, but parallel linkages are bulky compared to their workspace. Also, it is difficult to apply parallel linkage system in exoskeleton systems making their rotational axis be coincident to those of human joints. Anatomy of shoulder should be considered for natural motion of the arm, because of the translational motion of shoulder caused by the complex musculoskeletal system. Addressing singularity problem is also important, since the exoskeletons can easily reach to kinematic singularity positions due to the overlapping of shoulder joint axis.

CADEN-7 (Fig. 1-4a) and L-EXOS (Fig. 1-4b) were developed adopting pulley-based cable-driven actuation mechanism for lightweight structure [27, 28]. The systems also adopted reduction systems on the actuated joint side to increase joint stiffness. However, the structures are quite bulky

as shown in the Fig. 1-4a and Fig. 1-4b. The systems also did not consider translation of shoulder joint, and were not adjustable for individual body, which may disturb natural motion of the arm. Fig. 1-4c shows X-Arm-2, developed for the tele-operation of space robots. Thanks to the actuation system with redundant DOF, the system can adapt to the body segment length differences or the shoulder translation. Despite of the large number of DOF, its the system is quite compact and lightweight by utilizing tendon-sheath actuation mechanism. CAREX (Fig. 1-4b) was developed for the rehabilitation applications, adopting the parallel cable-driven mechanism. The actuated parts of the system were lightweight since there was no complex cable routing mechanism as aforementioned exoskeleton systems. Exoskeleton type haptic interfaces can provide torque feedback to user's joints, which is difficult to achieve in other haptic interfaces. However, it is also difficult to deliver desired forces to the hand, because the exoskeleton is connected with prior body segments, such as the upper arm and lower arm. Since most required tasks in tele-operation are performed by robot hands, it is important to provide precise force feedback to the hand. Exoskeletons have a disadvantage in such sense, but it would be useful in whole-arm manipulation tasks that require force/torque feedback to each segment or joint of user's arm.

As adopted in the exoskeleton type interfaces and Inca 6D, cable-driven actuation mechanisms have been used to achieve lightweight or compact structures for high force transparency and safety. Cable-driven actuation mechanisms can be classified into three types by the type of cable routing structures: pulley-based cable-driven actuation mechanism, tendon-sheath (bowden cable) actuation mechanism and parallel cable-driven actuation mechanism.

Pulley-based cable-driven actuation mechanism, which was applied in CADEN-7 and L-EXOS, utilizes idler pulleys for the cable routing. The cables are routed through idler pulleys on the intermediate joints. Because the pulleys have low friction, the force can be delivered to the drive joints without large loss. However, the idler pulleys make the system bulky and heavy, since at least three idler pulleys are required for each cable sets to ensure large range of motion. As the DOF of the system increase, more idler pulleys are placed on the prior joints, which lead to bulky and heavy system.

Tendon-sheath actuation mechanism, which was adopted in X-Arm-2, utilizes a flexible sheath for the routing of cables. The tendon (cable) delivers the force and position by sliding inside the core of the sheath. The routing structure is extremely compact and lightweight, thanks to this sliding-based transmission mechanism. However, the friction between the sheath and the tendon disturbs accurate control. In X-Arm-2, a torque sensor was placed on each actuated joints to compensate

the friction with a PID feedback controller, but this caused increased weight of the system. A simple feedforward friction compensator was used together with the feedback controller, but the friction model was not accurate. Feedforward control of the tendon-sheath actuation mechanism has been researched for the precise force/position control [31–34]. However, it was not achieved for tendon-sheath actuation mechanisms in multi-DOF systems, because the friction changes as the sheath configuration changes. Another problem is the pretension change in double tendon-sheath actuation mechanisms. In a double tendon-sheath actuation mechanism, the tendons are pre-loaded to prevent the derailment of the tendon from the joint pulleys. The pretension changes as the sheath configuration changes, due to the geometric characteristics of the sheath. The change of pretension also makes it difficult to analyze the friction, and large change of the pretension can cause safety problems.

In parallel cable-driven mechanism, which was used in Inca 6D and CAREX, the cables are directly connected from the actuators to the actuated joints without a cable routing structure. Therefore, aforementioned disadvantages are not shown in this mechanism. However, the interference between tendons and the user makes it difficult to apply this mechanism in haptic interfaces. The interference problem was addressed by a sliding-based component in CAREX, but this also introduced friction, which is a major disadvantage of the tendon-sheath actuation mechanism.

Since many disturbances, such as inertia, friction of gears, elongation of tendons and human-robot interaction force, are introduced in the haptic interfaces, control algorithm of haptic interfaces are also important. Many of aforementioned systems adopted simple controllers such as a PID controller, compensating the disturbances in feedforward or feedback manners [24–29]. However, such control algorithms can make problems in achieving accurate force/position tracking if there are large uncertainties. Especially, the performance of systems can be affected by human motions, since it is difficult to model or predict human motions.

The performance of the control interface can be improved providing 3D visual feedback to the user, as mentioned in Chapter 1.1. HMDs may be the most applicable 3D image display system, considering its immersive visual feedback capability with head tracking, wide field of view (FOV) and low price. Many HMDs have been launched in recent years thanks to the development of small-size, high-resolution displays [35–37]. HMDs usually contain an inertial measurement unit (IMU) so that it can display the view of a field in the direction of user's head orientation. 3D visual feedback can be provided to the user with the HMDs by providing stereoscopic images captured by two cameras. Several tele-operation systems adopted HMDs for the intuitive control of robot

cameras and to provide the user perspective images [12–14, 24, 38]. In such systems, the images captured by robot cameras are provided to the user so that the user easily understands the work site. However, the user could suffer from network delay that is inevitable in tele-operation systems with long distance. Display algorithms that provide the scene of virtual worlds constructed by point cloud data or image instead of recently captured scene from the robot camera have been developed to reduce such problem [12, 39, 40]. However, such methods require large computational burden or expensive sensors such as LIDAR.

1.3 Thesis Overview

A haptic control interface and a display system are developed for the tele-operation system, to overcome the limitations of aforementioned systems. This thesis aims to develop a lightweight haptic interface that can deliver desired force accurately while measuring the user's hand motion, and a tele-operated display system that provides comfortable use in tele-operation systems. This thesis is organized as follows.

[Chapter 2: Design of an Upper-limb Exoskeleton]

A 5-DOF upper-limb exoskeleton is designed in this chapter, as a candidate of a basic structure of the control interface. By analyzing the anatomy of human shoulder, a vertically translating joint is added to the traditional ball-and socket joint shoulder model so that the exoskeleton can ensure natural motion of user's shoulder. The shoulder joint of the exoskeleton is tilted to move the singularity position outside of the normal range of motion of the arm. Manipulability analysis is applied to determine the tilting angles. The performance of the proposed exoskeleton structure is tested by simulations and experiments with a kinematic prototype.

[Chapter 3: Cable-driven Mechanisms]

For the actuation of haptic control interface, two types of cable-driven mechanisms are developed in this chapter. In Chapter 3.1, an asymmetric pulley-based cable-driven mechanism is proposed for the force control of exoskeleton systems, inspired by the fact that the required forces in human motion are not symmetric in many cases. A compact tendon routing mechanism is achieved by replacing a tendon to a linear spring, which acts as an antagonistic force source to the other tendon. To enable precise force control, the spring-actuator mechanism is combined with the rotary series elastic mechanism. A robust controller based on the disturbance observer (DOB) is applied for high performance in force control. A prototype exoskeleton interface with the proposed mecha-

nism is tested in experiments including a tele-operation experiment with a robot arm.

Then, a new tendon-sheath actuation mechanism is proposed, addressing the limitations of conventional tendon-sheath actuation mechanisms. Tendon-sheath actuation mechanism may be one of the most lightweight actuation mechanisms, but it suffers from the friction between the tendon and the sheath and large pretension change, which are induced by the change of sheath configuration in multi-DOF systems. In chapter 3.2, a new tendon-sheath actuation mechanism, which enables feed-forward torque control in multi-DOF systems and allows low pretension change, is proposed. The friction is feedforwardly compensated using a friction model. The pretension change is reduced by adopting series elastic elements to maintain it an appropriate range. A tele-operation control interface is developed with the proposed mechanism, and its back-drivability and force delivery performance are tested in experiments.

[Chapter 4: A Display System for Tele-operation]

Head mounted display (HMD) is becoming popular as a visual feedback device of tele-operation systems, but the user can suffer from network delay. In this chapter, a vision feedback system for the tele-operation systems is developed with an HMD and a synchronized robot neck-camera module. Network delay is compensated by a practically usable predictive algorithm that utilizes the orientation difference between the user and the robot neck-camera module.

[Chapter 5: Concluding Remarks and Open Issues]

Concluding remarks of this thesis and the remaining issues are discussed in this chapter.

Chapter 2

Design of an Upper-limb Exoskeleton¹

2.1 Introduction

Exoskeletons have been the subject of growing research interest for application in haptic control interface, rehabilitation and power-assistance [27, 27–29, 41–51]. Since the system can directly deliver desired forces to attached body segments, it have a great potential as the control interface of robots, such as for the whole-arm manipulation and delivering collision information to the user. Because exoskeleton systems are worn by a human user, they must be designed carefully so that they move with the natural motion of the users, and do not compromise their safety. Exoskeleton systems are typically designed based on the skeletal system of the human body. However, it may not be possible to mimic the motion of the user’s internal joints using the same number of degrees of freedom (DOFs) during articulation of the exoskeleton joints. The problem is further complicated by the limited locations at which the actuators can be attached. Thus, exoskeleton systems have been designed based on an abstract skeletal model, which aims to mimic the main motions of the human body.

Some lower-limb exoskeletons have actuators only in the sagittal plane while other joints are passively actuated or even neglected [41–44]. In lower-limb exoskeletons, simplified designs based on an abstract skeletal model with reduced DOF may be appropriate because the main motions of the lower limb required for walking or running are in the sagittal plane. However, in upper-limb exoskeleton applications including the haptic control interface, it may not be possible to limit the DOFs in such a manner because the human arm typically requires multiple DOFs to access and

¹The contents of this chapter was published in [1]. Preliminary research results of the paper were published in [2, 3]. Reprinted with permission from IEEE.

manipulate objects in the workspace.

Various configurations have been proposed for upper-limb exoskeleton systems [27, 46, 47, 49, 51–59]; however, many unsolved issues for natural interaction with the human body remain, especially in terms of kinematic singularities and upper-limb biomechanics, such as shoulder elevation. The exoskeletons proposed in [52, 53] and [47] did not consider either the kinematic singularity problem or the shoulder elevation. Also, the exoskeleton in [47] did not properly fit to the arm due to the compact structure of the shoulder section. The singularity problem was considered in [27] and [57] by placing the actuator axis in a tilted orientation; however, the shoulder elevation was not considered. In [56], the singularity problem was considered by restricting the workspace of the exoskeleton, but again, the shoulder elevation was not considered, too. The shoulder elevation was considered in [46, 58, 59] and [51]; however, in these cases, kinematic singularities occurred easily; i.e., the singularity position was placed in the normal workspace of the upper-limb. The shoulder elevation was realized in [46] and [51], but the exoskeleton required a large mechanical structure and different alignments for each patient. In [55], the shoulder elevation was considered by using a dislocated rotation axis, but the shoulder motion was not properly approximated. In [54], both the kinematic singularity and shoulder biomechanics were considered; however, the results were not analyzed or verified kinematically.

In Chapter 2, an upper-limb exoskeleton system is proposed as a candidate of control interface structure. The system is designed for the shoulder and the elbow that uses 5 DOF to mimic the complicated motions that arise from the shoulder structure. The shoulder was modeled as a 4-DOF joint by adding the shoulder elevation as a vertical movement; the elbow was modeled as a 1-DOF hinge joint. To avoid the singularity problem, the shoulder joint was tilted so that the singularity position was placed outside of the workspace of the human arm. The performance of the proposed upper-limb exoskeleton; i.e., whether it could reach all points in the normal range of motion, was analyzed in the framework of forward and inverse kinematics. Because shoulder elevation, which affects the positions of all joints, is considered in this system, the inverse kinematic problem was solved in an iterative manner.

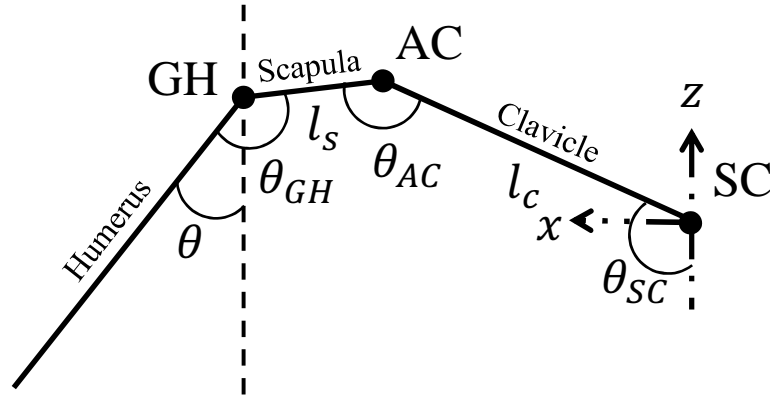


Figure 2-1: Illustration of the skeletal structure of the shoulder. (Edited from [55])

2.2 Design of the 5 DOF Upper-limb Exoskeleton

2.2.1 Anatomical Analysis of the Shoulder

The human arm has been modeled using several kinematic methods. Due to the complexity of the problem, it is usually modeled using a 7-DOF kinematic system by imposing simplifications to the arm joints and segments. The shoulder joint can be considered as a ball-and-socket joint with 3 DOF: flexion-extension, abduction-adduction, and medial rotation. The elbow can be modeled as a single-axis hinge joint with 1 DOF, and the wrist as a ball-and-socket joint with 3 DOF.

From an anatomical point of view, however, the shoulder joint should be modeled using more than 3 DOF, because many muscles and bones are involved in its movement [54, 60]. The shoulder joint is composed of three bones: the clavicle, scapula, and humerus, as shown in Fig. 1, and the movement of the shoulder results from the combined motion of each bone. The main rotation of the shoulder occurs at the glenohumeral (GH) joint of the scapula and the humerus. However, the center of the GH (CGH) moves as a result of the motion of the acromioclavicular (AC) and sternoclavicular (SC) joints. The CGH can be described by the angles of the SC and AC joints, as follows [55]:

$$X_{CGH} = (l_c \cos(\theta_{SC} - 90^\circ) - l_s \sin(\theta_{AC} + \theta_{SC})) \frac{h}{h_{ref}} \quad (2.1)$$

$$Z_{CGH} = (l_c \sin(\theta_{SC} - 90^\circ) + l_s \cos(\theta_{AC} + \theta_{SC})) \frac{h}{h_{ref}} \quad (2.2)$$

where l_c and l_s are the effective lengths of the clavicle and the scapula of the shoulder joint, respectively. Because the magnitude of the shoulder motion is dependent on the body size, the height of the user, h , is added as a scaling factor; $h_{ref} = 180\text{cm}$ was used as a reference value in this analysis

Table 2.1: Change of θ_{SC} θ_{AC} by shoulder elevation.

	$\Delta\theta_{SC}$ (deg)	$\Delta\theta_{AC}$ (deg)
$0^\circ \leq \theta < 30^\circ$	$\frac{4}{30}\theta$	0
$30^\circ \leq \theta < 80^\circ$	$4 + 11 \cdot \frac{\theta-30}{50}$	0
$80^\circ \leq \theta < 140^\circ$	15	$35 \cdot \frac{\theta-80}{60}$
$140^\circ \leq \theta < 180^\circ$	$15 + 9 \cdot \frac{\theta-140}{40}$	35

because the lengths of the bone segments are proportional to the body size [61].

The relationship between the AC and SC angles and the net shoulder elevation angle, θ , is shown in Table 2.1 (Edited from [55]). Using the relationship in Table 2.1, θ_{SC} and θ_{AC} are obtained from the shoulder elevation angle, θ . Then, the position of CGH, X_{CGH} and Z_{CGH} , can be calculated using (2.1) and (2.2) as follows:

$$\Delta X_{CGH} = X_{CGH}(\theta) - X_{CGH}(0) \quad (2.3)$$

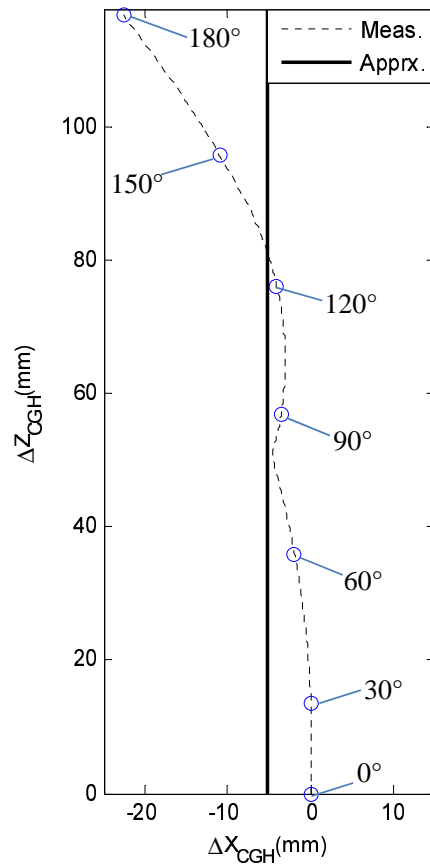
$$\Delta Z_{CGH} = Z_{CGH}(\theta) - Z_{CGH}(0) = d_1 \quad (2.4)$$

As the net shoulder elevation angle changes from 0° to 180° , the variation of CGH is -22.6 mm in the x direction and 117 mm in the z direction for a 170 cm-tall adult, as shown in Fig. 2-2a. The corresponding angle, θ , is indicated by dots in the figure. Because the lateral change is relatively small compared with the vertical change, the CGH motion can be approximated by a vertical displacement, as shown in Fig. 2-2a. In this study, only the vertical movement of the CGH was considered in the design of the upper-limb exoskeleton. The relationship between the vertical movement of CGH and the net shoulder elevation angle used in this analysis is shown in Fig. 2-2b.

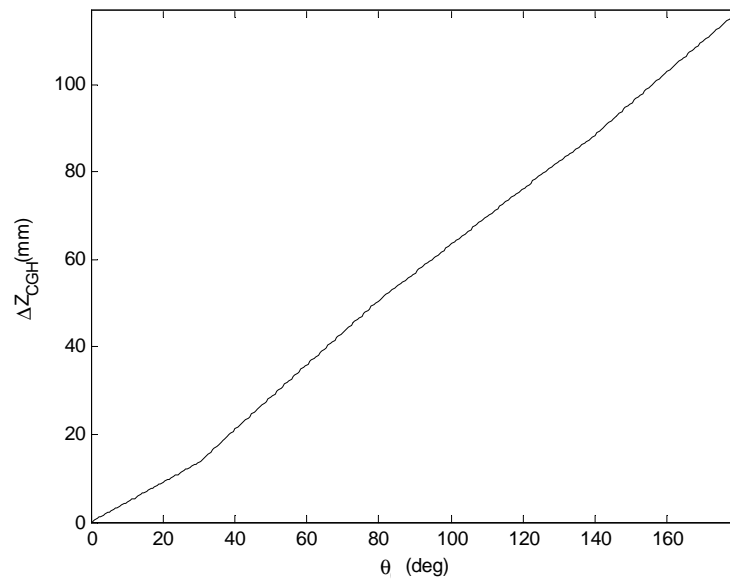
After this anatomical analysis of the shoulder, one DOF was added to account for the vertical movement of the CGH. The 5-DOF upper-limb exoskeleton is shown schematically in Fig. 2-3. θ_1 , θ_2 , and θ_3 describe the shoulder rotation, θ_4 describes the elbow rotation, and d_1 describes the CGH elevation.

2.2.2 Singularity of the Upper-limb Exoskeleton

In the design of mechanical system, singularities should be avoided because the mechanical system cannot move in a certain direction at the singular position [62]. This is especially important in ex-



(a) CGH change by arm lifting



(b) Relationship between the vertical movement of the CGH and the net shoulder elevation angle

Figure 2-2: Variation of the CGH by arm lifting.

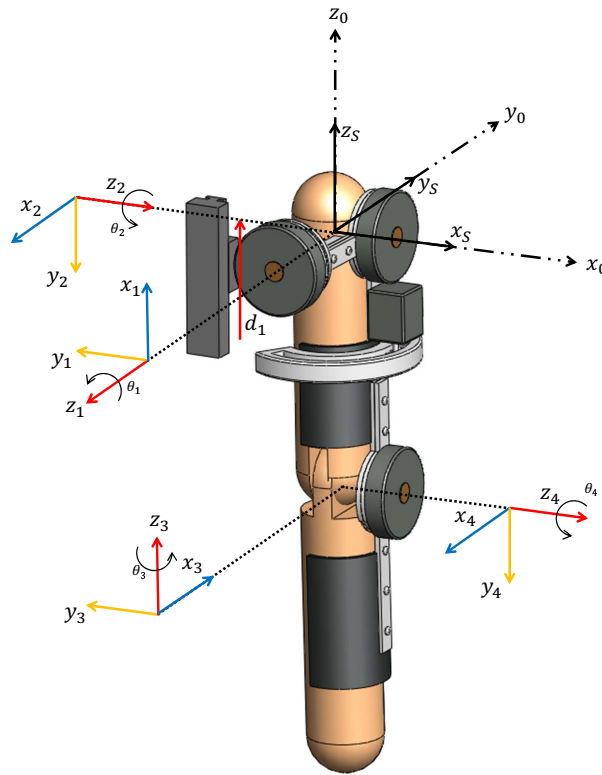


Figure 2-3: Initial configuration of the upper-limb exoskeleton.

oskeleton systems, because the user may become injured without appropriate control at the singular position.

With the configuration shown in Fig. 2-3, the upper-limb exoskeleton is in a singular position when the arm is straight forward, i.e., $\theta_2 = 90^\circ$. In this position, the rotation axes of θ_1 and θ_3 are collinear; thus, cross-body abduction or adduction motions cannot be achieved. Systems using redundant DOFs have been proposed to deal with such singularity issues. However, these systems may result in control issues because they admit an infinite number of kinematic solutions [63]. In this study, the shoulder joint was tilted so that the singularity position occurs outside the normal range of motion of the arm.

The normal range of motion of the arm is specified in Table 2.2 [64]. The shoulder was tilted in two steps: the first was a rotation of the exoskeleton around x_0 by α , as shown in Fig. 2-4a; the second was a rotation about z'_0 by β (Fig. 2-4b). The final configuration of the upper-limb exoskeleton with the tilted shoulder is shown in Fig. 2-5. In this configuration, the singularity that occurs when the arm is in the straight-forward position in the initial model shown in Fig. 2-3, now occurs when the arm is pointing upwards to the left, which is outside of the workspace.

Tilting the shoulder joint to avoid singularity problems in the workspace has been proposed

Table 2.2: Shoulder range of motion.

	Max. range (deg)
Forward flexion and extension	167° / 62°
Abduction	184° / 0°
Cross-body adduction	140° / 0°

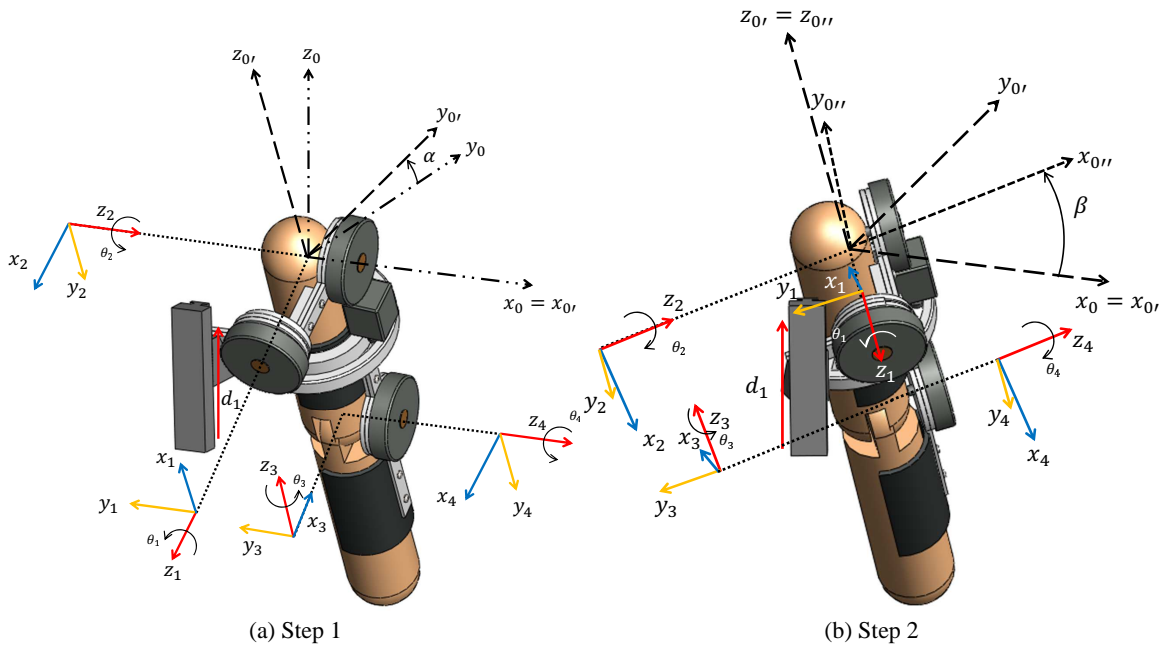


Figure 2-4: Tilting of the shoulder joint.

previously [27, 57]; however, variation of the shoulder elevation has not been considered simultaneously with a tilted shoulder joint. Note that the shoulder elevation is 117 mm for a 170-cm adult while θ is varied from 0° to 180° . Without considering the shoulder elevation, natural motion through the upper-limb exoskeleton is not possible.

2.3 Kinematic Analysis

The proposed 5-DOF upper-limb exoskeleton with a tilted and vertically translating shoulder joint is analyzed by forward and inverse kinematics methods in this chapter. Here, we determine whether the proposed exoskeleton is able to reach all points in the upper-limb workspace.

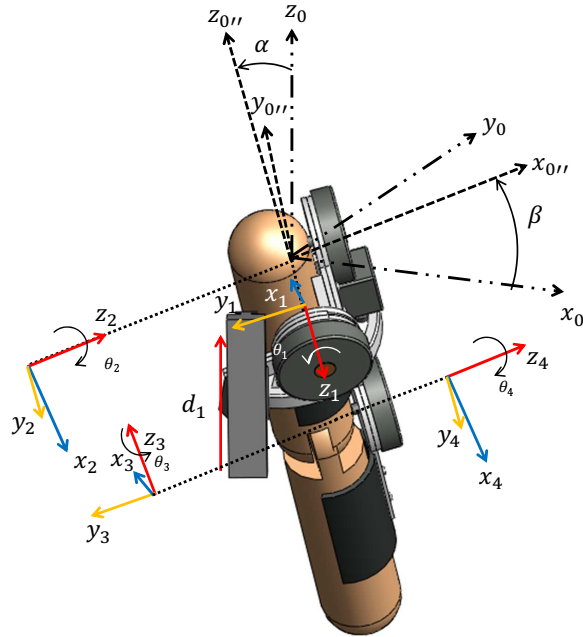


Figure 2-5: Final configuration of the upper-limb exoskeleton.

2.3.1 Forward Kinematics Analysis: DH Parameter

The kinematics of the proposed 5-DOF upper-limb exoskeleton was analyzed by the Denavit-Hartenberg (DH) parameters [62]. Here, S is the initial coordinate, 0 is the moved vertically from S , and $0''$ is tilted, i.e., rotated from 0 by α and β . The remaining coordinates are specified in Fig. 2-5. Using the relationship between the coordinates in the figure, the DH parameters are listed in Table 2.3.

2.3.2 Iterative Inverse Kinematics

Given an arbitrary end-effector position (the wrist position in this configuration), the corresponding joint angles can be calculated using inverse kinematics. The coordinates of each joint are specified in Fig. 2-6; L_u and L_l are the lengths of the upper and the lower arms, and the positions of the wrist and the elbow are given by $\mathbf{p}_w = (x_w, y_w, z_w)$ and $\mathbf{p}_e = (x_e, y_e, z_e)$, respectively. $\mathbf{p}_0 = (x_0, y_0, z_0)$ is the position of the CGH after the shoulder elevation, d_1 , which is determined by the shoulder elevation in Fig. 2-2b. The shoulder elevation affects the positions of all joints; thus the joint angles were calculated iteratively. An iterative method was developed based on the bisection method [65], which guarantees solution convergence. A flowchart of the iterative inverse kinematics calculations is shown in Fig. 2-7.

Table 2.3: DH parameters of the proposed configuration.

Trans. Matrix	α_{i-1}	a_{i-1}	d_i	θ_i
T_{S0}	0°	0	d_1	0°
$T_{00''}$	α	0	0	β
$T_{0''1}$	90°	0	0	$90^\circ + \theta_1$
T_{12}	90°	0	0	$90^\circ + \theta_2$
T_{23}	90°	0	$-L_u$	$180^\circ + \theta_3$
T_{34}	90°	0	0	$-180^\circ + \theta_4$

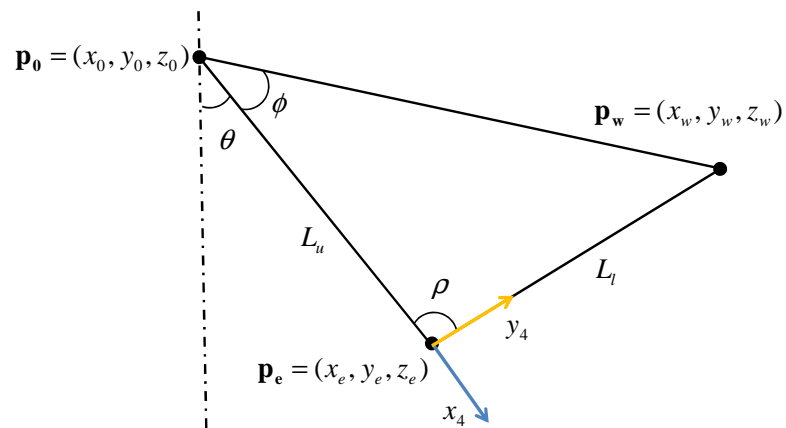


Figure 2-6: Geometric relationship of coordinates used for the inverse kinematics.

First, the initial interval of the vertical CGH displacement d_1 is set to $[v_1, v_2]=[0, v_{max}]$ mm, where v_{max} is the maximum possible vertical translation of CGH. The midpoint is set to $v_3=(v_1 + v_2)/2$. For each of v_1 , v_2 and v_3 , the angles ρ and ϕ in Fig. 2-6 are calculated using the law of cosines based on the following geometric relationships:

$$\rho = \cos^{-1}\left(\frac{L_u^2 + L_l^2 - \|\mathbf{p}_0 - \mathbf{p}_w\|^2}{2L_u L_l}\right) \quad (2.5)$$

$$\phi = \cos^{-1}\left(\frac{L_u^2 + \|\mathbf{p}_0 - \mathbf{p}_w\|^2 - L_l^2}{2L_u \|\mathbf{p}_0 - \mathbf{p}_w\|}\right) \quad (2.6)$$

Then θ_4 can be obtained by ρ as follows:

$$\theta_4 = \pi - \rho \quad (2.7)$$

However, there are an infinite number of solutions for the net shoulder elevation angle, θ . By considering the physical limitations of the arm, the angle of rotation of the elbow about the axis from the shoulder to the end-effector, termed the swivel angle, can be determined [66]. The swivel angle was set to 45° from the sagittal plane to outside of the body. The lowest elbow position was assigned a value of 0° by considering the physical limitations of the elbow. Once the elbow position was determined, the net shoulder elevation angle θ could be calculated as follows:

$$\theta = \cos^{-1}\left(\frac{L_u^2 + \|\mathbf{p}_0\|^2 - \|\mathbf{p}_0 + \mathbf{p}_e\|^2}{2L_u \|\mathbf{p}_0\|}\right) \quad (2.8)$$

The transformation of coordinate matrix 4 with respect to S can be specified as follows:

$$T_{S4} = \begin{pmatrix} x_{41} & y_{41} & z_{41} & x_e \\ x_{42} & y_{42} & z_{42} & y_e \\ x_{43} & y_{43} & z_{43} & z_e \\ 0 & 0 & 0 & 1 \end{pmatrix} \quad (2.9)$$

where

$$z_4 = \frac{\mathbf{p}_e \times \mathbf{p}_w}{\|\mathbf{p}_e \times \mathbf{p}_w\|} \quad (2.10)$$

$$y_4 = \frac{\mathbf{p}_w - \mathbf{p}_e}{\|\mathbf{p}_w - \mathbf{p}_e\|} \quad (2.11)$$

$$x_4 = y_4 \times z_4 \quad (2.12)$$

The transformation matrix from S to $0''$, $T_{10''}$, can be determined by the shoulder elevation, d_1 , and the tilting angles, α and β , as follows:

$$T_{S0''} = \begin{pmatrix} \cos\beta & -\sin\beta & 0 & 0 \\ \cos\alpha\sin\beta & \cos\alpha\cos\beta & -\sin\alpha & 0 \\ \sin\alpha\sin\beta & \sin\alpha\cos\beta & \cos\alpha & d_1 \\ 0 & 0 & 0 & 1 \end{pmatrix} \quad (2.13)$$

Since the transformation matrices T_{S4} and $T_{S0''}$ are determined by (2.9) and (2.13), the transformation matrix from $0''$ to 4 can be calculated as follows:

$$T_{S4} = T_{S0''}T_{0''4} \quad (2.14)$$

$$T_{0''4} = T_{S0''}^{-1}T_{S4} \quad (2.15)$$

Suppose the transformation matrix from $0''$ to 4 obtained by (2.15) is

$$T_{0''4,Inv} = \begin{pmatrix} x''_{41,Inv} & y''_{41,Inv} & z''_{41,Inv} & x''_{e,Inv} \\ x''_{42,Inv} & y''_{42,Inv} & z''_{42,Inv} & y''_{e,Inv} \\ x''_{43,Inv} & y''_{43,Inv} & z''_{43,Inv} & z''_{e,Inv} \\ 0 & 0 & 0 & 1 \end{pmatrix} \quad (2.16)$$

The transformation matrix from $0''$ to 4 can also be calculated from the DH parameters:

$$T_{0''4,DH} = \begin{pmatrix} x''_{41,DH} & y''_{41,DH} & z''_{41,DH} & x''_{e,DH} \\ x''_{42,DH} & y''_{42,DH} & z''_{42,DH} & y''_{e,DH} \\ x''_{43,DH} & y''_{43,DH} & z''_{43,DH} & z''_{e,DH} \\ 0 & 0 & 0 & 1 \end{pmatrix} \quad (2.17)$$

where

$$x''_{41,DH} = c\theta_4(s\theta_1s\theta_2c\theta_3 + s\theta_3c\theta_1) + s\theta_1s\theta_4c\theta_2 \quad (2.18)$$

$$x''_{42,DH} = -c\theta_2c\theta_3c\theta_4 + s\theta_2s\theta_4 \quad (2.19)$$

$$x''_{43,DH} = c\theta_4(s\theta_1s\theta_3 - s\theta_2c\theta_1c\theta_3) - s\theta_4c\theta_1c\theta_2 \quad (2.20)$$

$$y''_{41,DH} = s\theta_1(c\theta_2c\theta_4 - s\theta_2s\theta_4c\theta_3) - s\theta_3s\theta_4c\theta_1 \quad (2.21)$$

$$y''_{42,DH} = s\theta_4c\theta_2c\theta_3 + s\theta_2c\theta_4 \quad (2.22)$$

$$y''_{43,DH} = s\theta_4(s\theta_2c\theta_1c\theta_3 - s\theta_1s\theta_3) - c\theta_1c\theta_2c\theta_4 \quad (2.23)$$

$$z''_{41,DH} = c\theta_1c\theta_3 - s\theta_1s\theta_2s\theta_3 \quad (2.24)$$

$$z''_{42,DH} = s\theta_3c\theta_2 \quad (2.25)$$

$$z''_{43,DH} = s\theta_2s\theta_3c\theta_1 + s\theta_1c\theta_3 \quad (2.26)$$

$$x''_{e,DH} = L_u s\theta_1 c\theta_2 \quad (2.27)$$

$$y''_{e,DH} = L_u s\theta_2 \quad (2.28)$$

$$z''_{e,DH} = -L_u c\theta_1 c\theta_2 \quad (2.29)$$

$s(\theta)$ and $c(\theta)$ represent $\sin(\theta)$ and $\cos(\theta)$, respectively. Then, the rest angles, θ_1 , θ_2 and θ_3 , are calculated by comparing (2.16) and (2.17) as follows :

$$\theta_2 = \sin^{-1}\left(\frac{y''_{e,Inv}}{L_u}\right) \quad (2.30)$$

$$\theta_3 = \sin^{-1}\left(\frac{z''_{42,Inv}}{\cos\theta_2}\right) \quad (2.31)$$

$$\theta_1 = \sin^{-1}\left(\frac{x''_{e,Inv}}{L_u \cos\theta_2}\right) \quad (2.32)$$

After calculating the net shoulder elevation angles for the initial vertical CGH displacements v_1 , v_2 and v_3 , the new vertical displacements v_{1n} , v_{2n} and v_{3n} are calculated using the relationships shown in Fig. 2-2b. The next step follows the iterative procedure described in Fig. 2-7, which was constructed based on the bisection method. The procedure continues until the following convergence criterion is satisfied:

$$|v_1 - v_2| < \varepsilon \quad (2.33)$$

where ε is a specified tolerance. In the simulations, the tolerance was set to 0.001 mm.

2.4 Performance Verification by Simulation

The proposed 5-DOF upper-limb exoskeleton and the kinematic analysis methods were verified by simulations. A linear path trajectory of the end effector was specified in a normal workspace. The user's height h was set to 170 cm, and the length of the clavicle l_c and scapula l_s were set to 149.4 mm and 66.8 mm, respectively [55, 61]. The lengths of the upper arm L_u and lower arm L_l were both set to 285 mm.

2.4.1 Joint Trajectories

Both kinematic models, i.e., with and without shoulder elevation, were tested. Figure 2-8 shows the arm motions of each model for the given end-effector trajectory. Both simulated datasets indicated smooth motion; however, the kinematic model with shoulder elevation better approximated human arm motion.

Figure 2-9 shows the joint angles of the kinematic model with a fixed shoulder joint (black) and a vertically translating shoulder joint (red). The joint angles of the vertically translating shoulder joint were calculated using the iterative inverse kinematics method. The average number of iteration of each point was 17, which means that the proposed analysis methods can be implemented in real time. The circles in the figure correspond to the intermediate points, which are marked as blue circles in Fig. 2-8b. Note that the shoulder elevation of the moving shoulder joint shown in Fig. 2-9(e) was about 50 mm, which represents a significant deviation from the conventional model, in which the elevation of the shoulder joint is fixed. Due to the difference in the shoulder elevation, other joints moved along different trajectories, as shown in Fig. 2-9(a) to (d), which produced an unnatural motion of the upper limb.

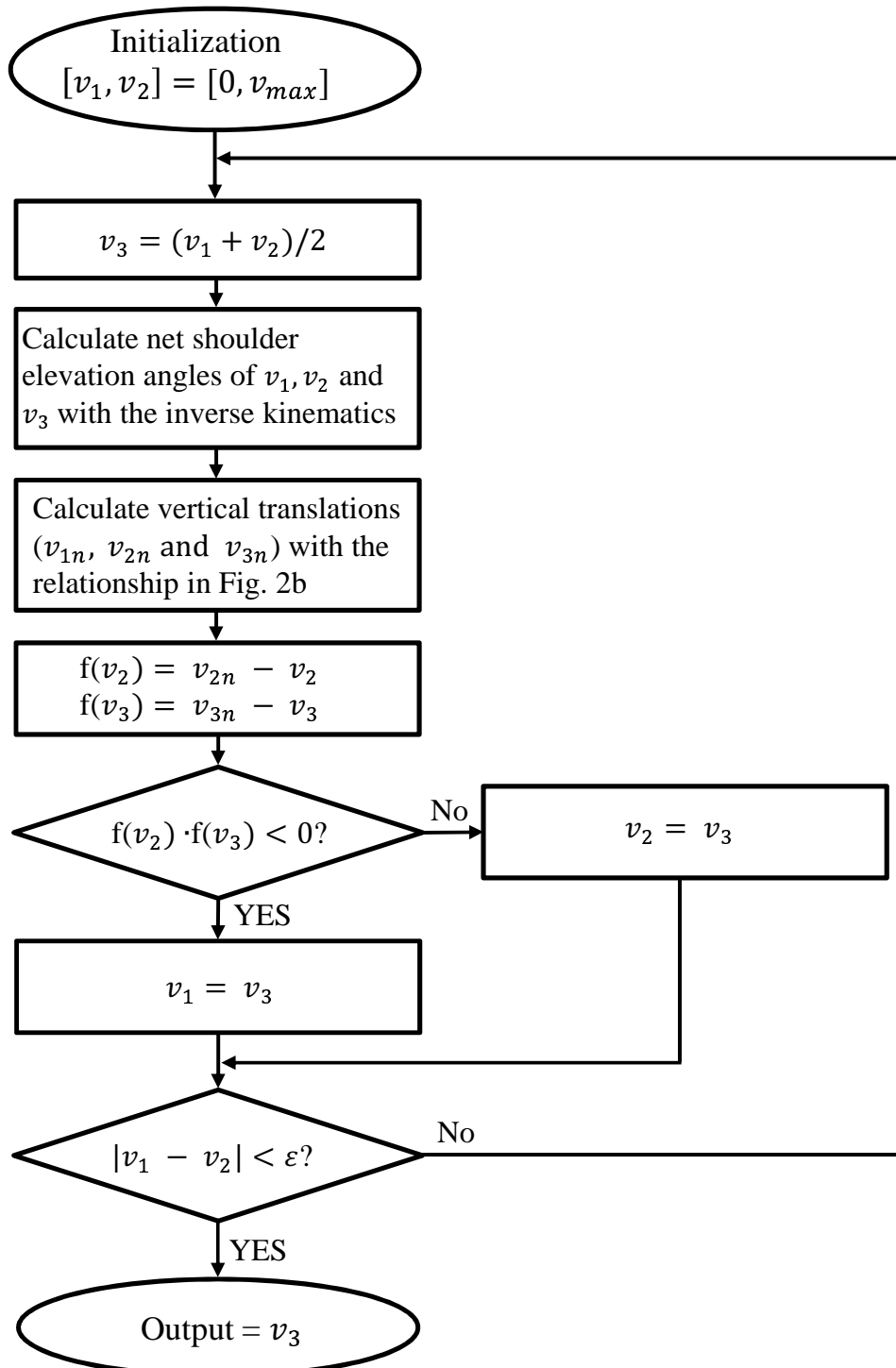
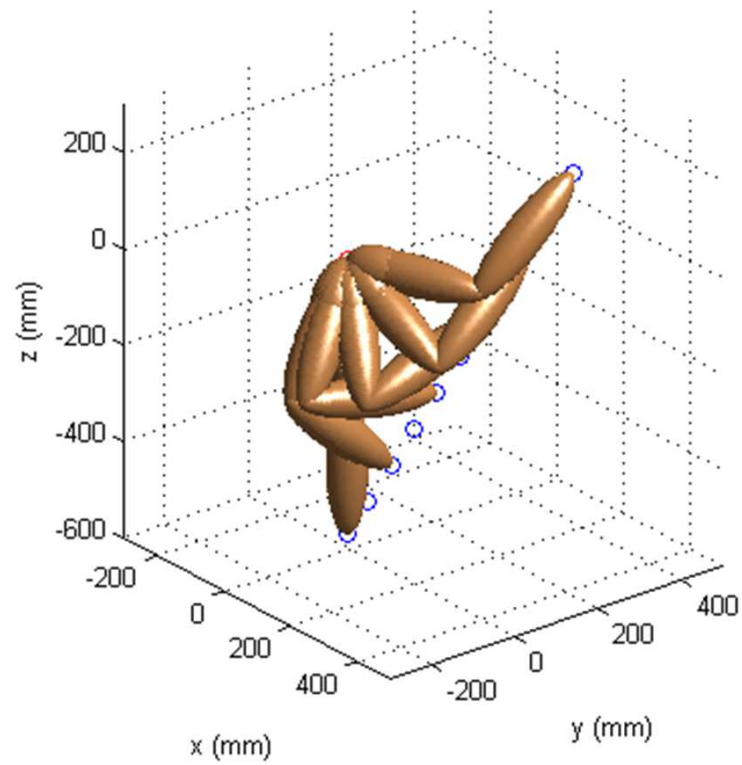
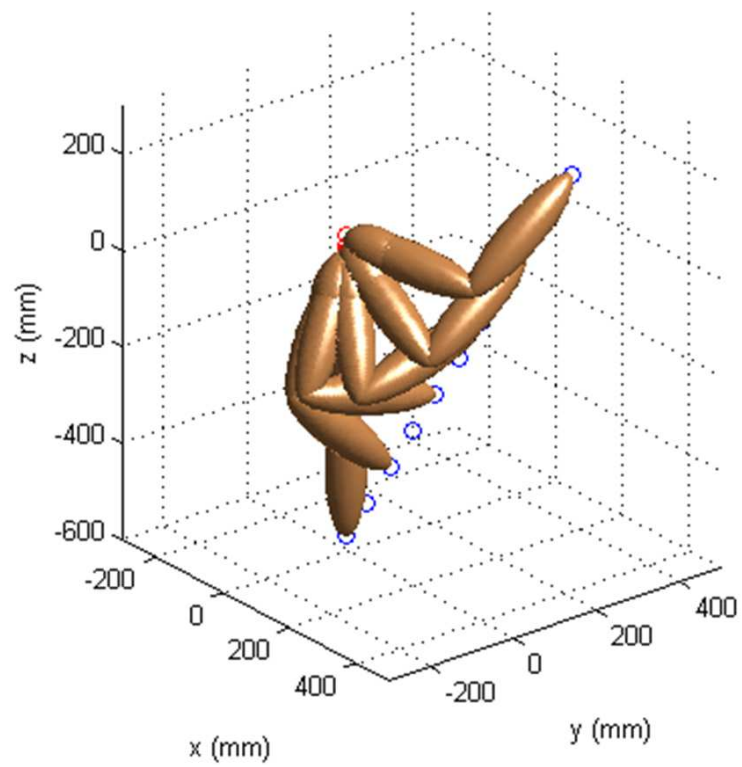


Figure 2-7: Flow chart of the iterative inverse kinematics calculation.

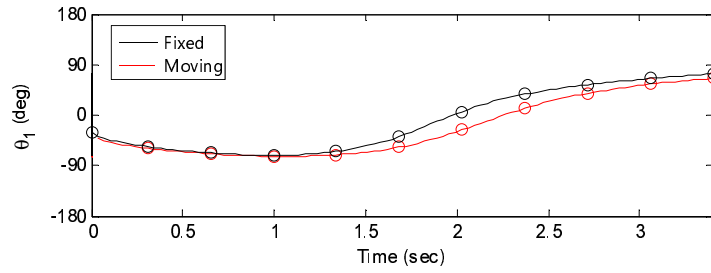


(a) Simulation of the kinematic models without shoulder elevation

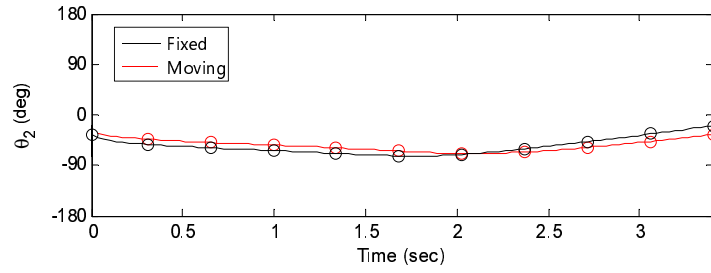


(b) Simulation of the kinematic models with shoulder elevation

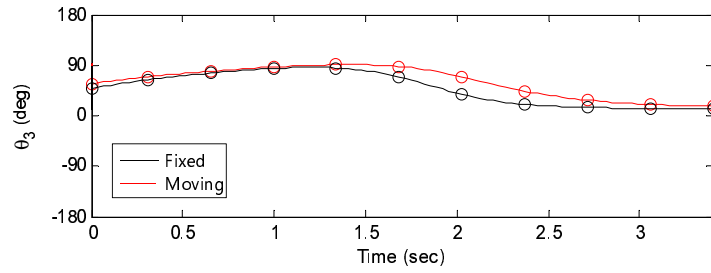
Figure 2-8: Simulation of the kinematic models with and without shoulder elevation.



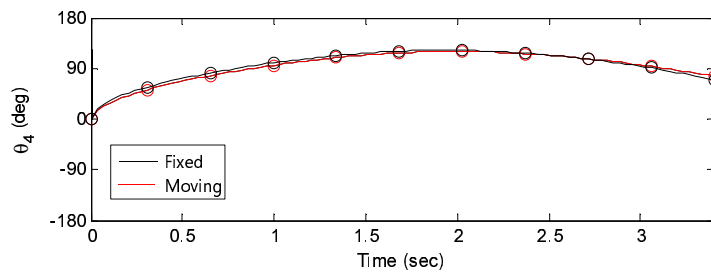
(a) θ_1



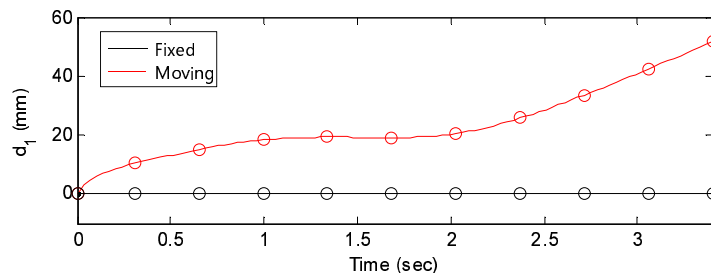
(b) θ_2



(c) θ_3



(d) θ_4



(e) d_1

Figure 2-9: Joint angles of the fixed or moving shoulder joint models.

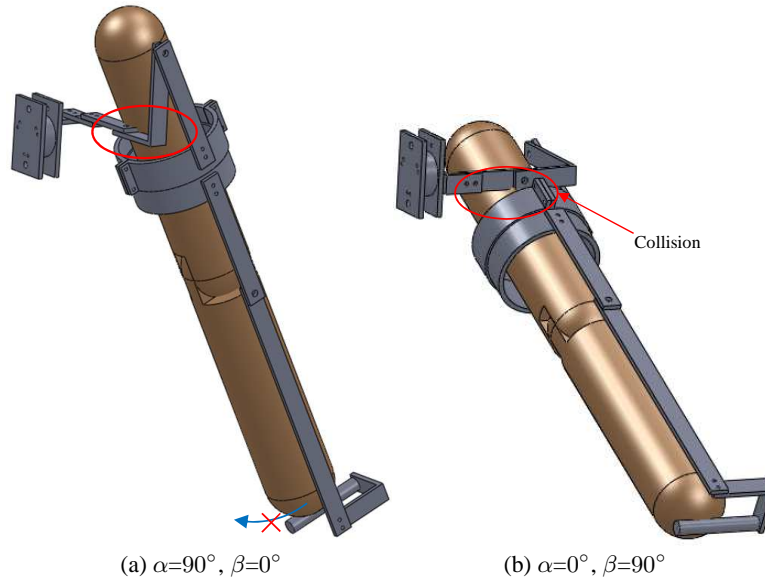


Figure 2-10: Physical interference by extreme tilting angles.

2.4.2 Manipulability Analysis

In the proposed design, the shoulder joint is tilted so that the singularities happens outside of the normal workspace of the upper limb. A manipulability analysis was performed to determine the tilting angles. The manipulability is a quantitative measure of end-effector manipulation ability, which is defined as follows [62]:

$$w(\theta) = \sqrt{\det(J(\theta)J^T(\theta))} \quad (2.34)$$

where θ is a joint angle vector and J is the Jacobian. The manipulability vanished at a singular configuration; thus, the singularities can be analyzed by comparing the manipulability values of each point in the workspace.

Because the exoskeleton is worn by a human, the shoulder tilting angles α and β should be determined by considering the physical interference between the human user and the exoskeleton structure. The arm cannot be rotated backward if α is too large, and abduction is not possible if β is too large because of a collision. Two extreme cases are illustrated in Fig. 2-10. In both cases, the exoskeleton structure interferes with the user's arm. Thus, the tilting angles α and β were restricted to values between 0° and 50° .

The simulation conditions were set as follows. The user's height h was set to 170 cm, and the lengths of the clavicle l_c and scapula l_s were set to 149.4 mm and 66.8 mm, respectively [55,61]. The

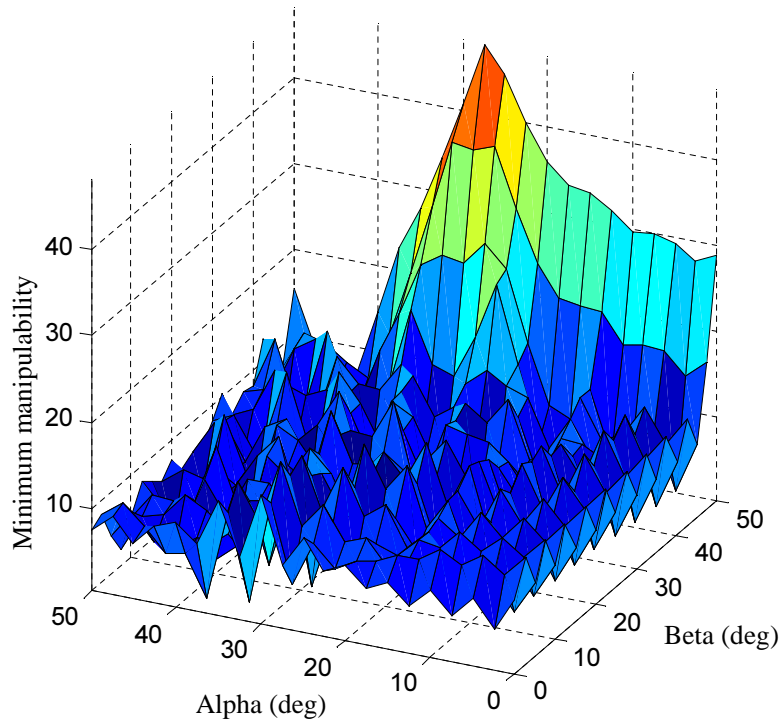


Figure 2-11: Minimum manipulability of α and β .

lengths of upper arm L_u and lower arm L_l were both set to 285 mm. In this simulation, 1180 points were placed on the surface of the workspace, considering the motion range of a normal upper limb specified in Table 2.2. The workspace surface was prepared by considering the vertical shoulder elevation. The distance from CGH to each point was set to 565 mm, which is almost identical to the length of a fully stretched arm in the simulation.

The joint angles at each point were calculated using the proposed iterative inverse kinematics method. Using these, the Jacobian and manipulability at each point were derived. The manipulability calculations were repeated to determine the appropriate tilting angles of the shoulder joint to avoid singularities. The tilting angles were varied from 0° to 50° in 2.5° increments, and the manipulability of all points on the workspace surface at these angles were calculated. The minimum manipulability was chosen to represent the performance of the tilting angle set because a larger minimum manipulability implies that the singularity position is farther from the workspace.

Figure 2-11 shows the results of the manipulability analysis. The maximum value among the minimum manipulability measures appeared at $\alpha = 27.5^\circ$ and $\beta = 50^\circ$. Therefore, these values were chosen for the shoulder tilting angles.

To verify that a singularity did not occur in the workspace of the upper-limb, the manipulability values of the points on the workspace surface were visualized. The manipulability of each point was

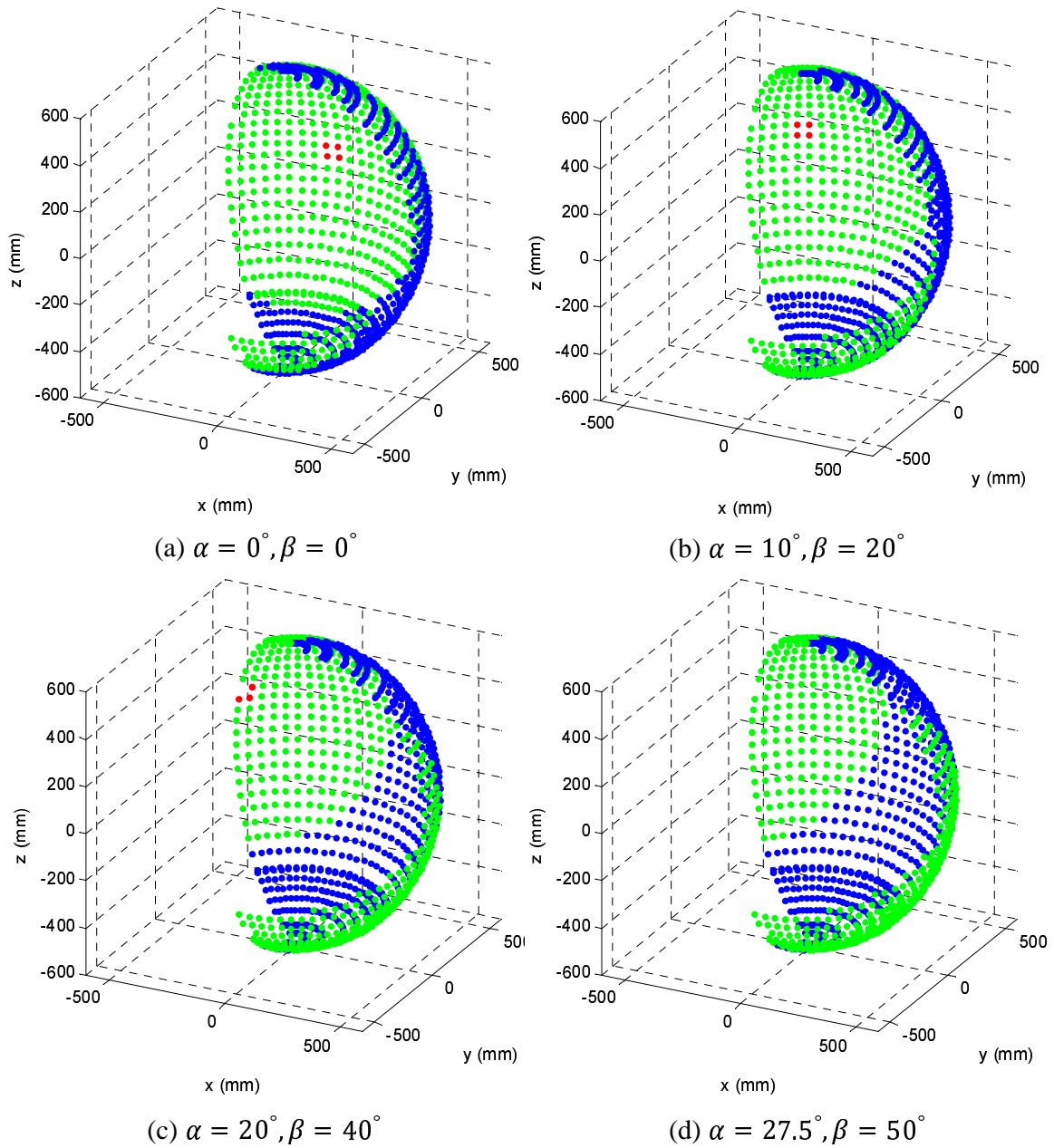


Figure 2-12: Change of the singularity position by tilting the shoulder joints.

calculated and normalized by the maximum manipulability value among all the points at a given α and β . The normalized manipulability measure M is shown in Fig. 2-12, using a three-color coding scheme. The points $0.0 < M \leq 0.1$, $0.1 < M \leq 0.9$, and $0.9 < M \leq 1.0$ are coded in red, green, and blue, respectively. The red dots indicate areas which are more likely to have singularities.

The singularity position was shifted by changing the tilting angles. The red zone, which represents the area close to singularity positions, appeared at $\alpha = 0^\circ$, $\beta = 0^\circ$ in the straight-forward posture. The red zone was shifted as α and β are changed as shown in Fig. 2-12b and Fig. 2-12c. Finally, the red zone disappeared at $\alpha = 27.5^\circ$, $\beta = 50^\circ$, which were chosen as the final tilting angles; i.e., the singularities did not occur in the workspace for the tilting angles.

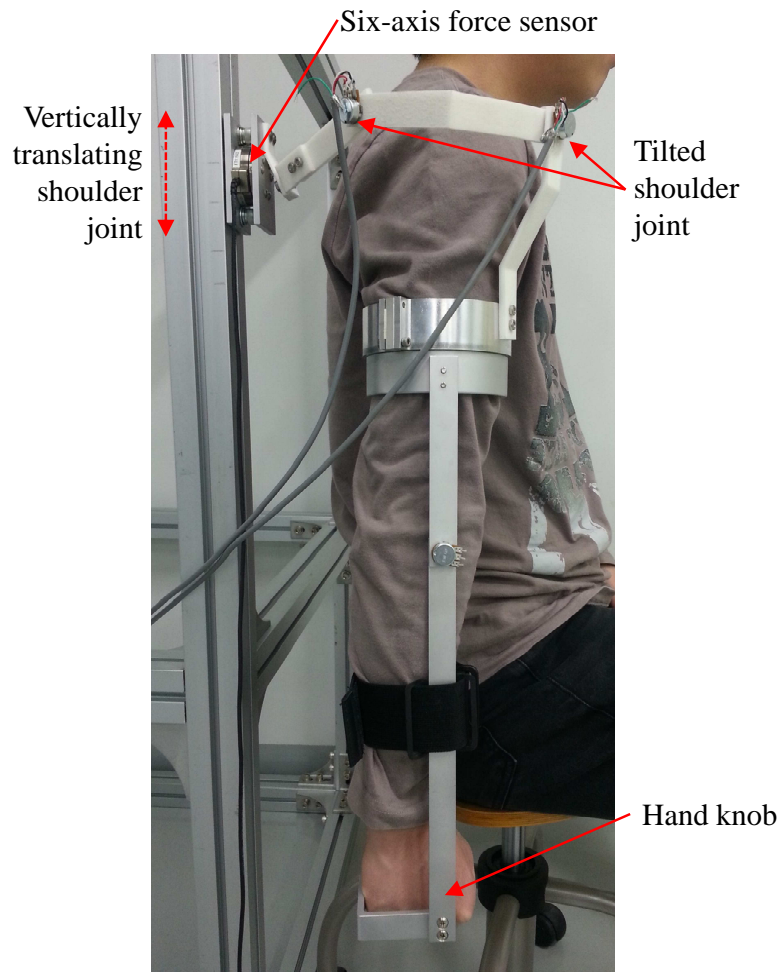
2.5 Performance Verification by Experiment

2.5.1 Force Analysis

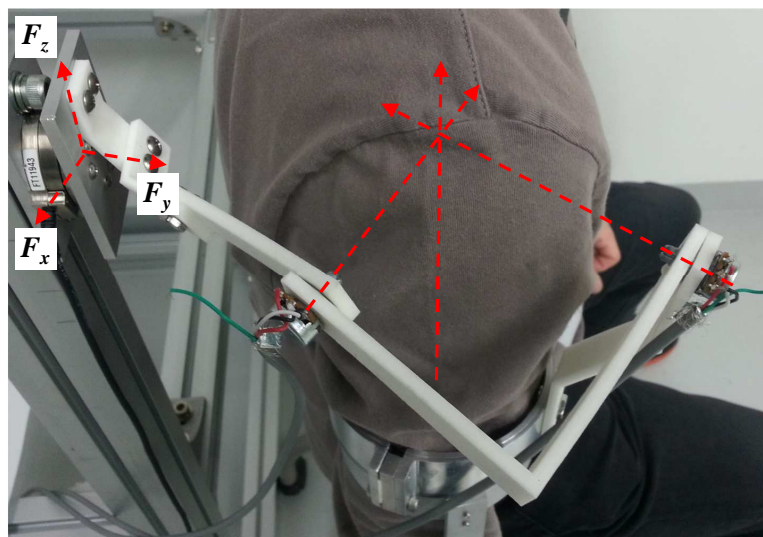
An unactuated 5-DOF upper-limb exoskeleton was manufactured as a prototype of the proposed exoskeleton, as shown in Fig. 2-13. The shoulder joint was tilted as shown in Fig. 2-5 and was able to move vertically using a linear guide rail. A six-axis force sensor (ATI, Mini45 [67]) was installed at the mounting part of the exoskeleton to measure the force applied to the shoulder joint. The net shoulder elevation was calculated by measuring the tilted shoulder joint angles with potentiometers.

Figure 2-14a shows the exoskeleton in a straight forward position, which is the singularity position of the conventional upper-limb exoskeleton shown in Fig. 2-3. As analyzed in Chapter 2.4.2, the proposed upper-limb exoskeleton did not have a kinematic singularity at the straight forward position; i.e., the user was able to move his arm in the transversal plane even in this posture. Figure 2-14b shows an arm posture that was closed to the shifted singularity position. However, as observed in the figure, the shifted singularity position was difficult to reach because it was outside of the normal workspace of the upper limb. Thus, kinematic singularities did not occur in the normal workspace of the upper limb using the proposed upper-limb exoskeleton.

The performance of the proposed system was verified by measuring applied force to the shoulder joint while lifting the arm. Five healthy subjects (three males and two females, age: 23.2 ± 0.45 , height: 166.4 ± 2.2 cm) were participated for the experiment. The participants wore two different upper-limb exoskeletons; upper-limb exoskeletons with a fixed shoulder joint and a freely movable shoulder joint. They were asked to raise their arm in the sagittal plane while holding the hand knob tightly. The applied force to the shoulder joint while lifting the arm was measured by the



(a) Side view of the exoskeleton prototype

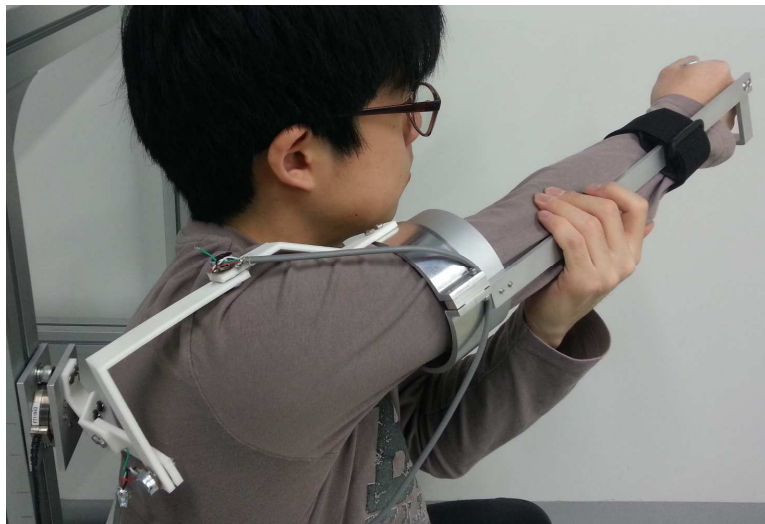


(b) Tilted shoulder joint of the exoskeleton prototype

Figure 2-13: Manufactured exoskeleton prototype.

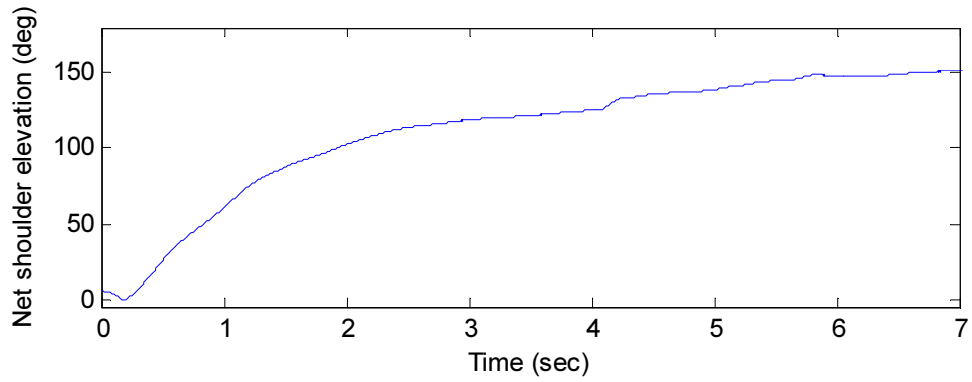


(a) Straight forward position of the exoskeleton prototype

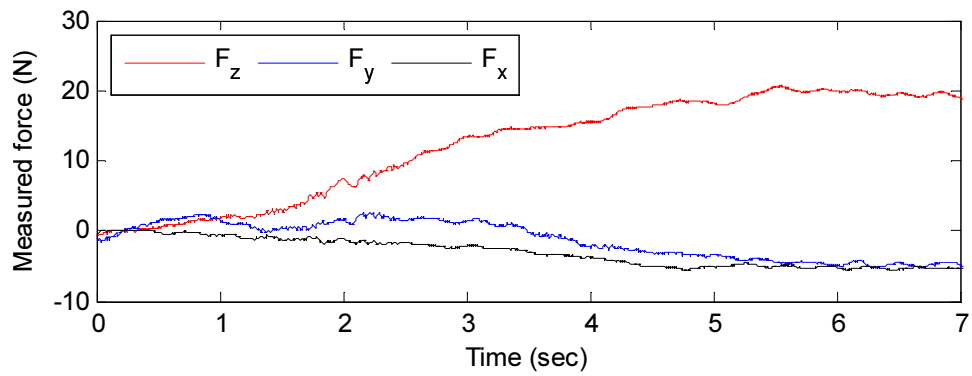


(b) Singularity position of the exoskeleton prototype

Figure 2-14: Shifted singularity position of the exoskeleton prototype.



(a) Net shoulder elevation (θ) during arm elevation



(b) Measured force during arm elevation

Figure 2-15: Net shoulder elevation and the measured force with the fixed shoulder joint.

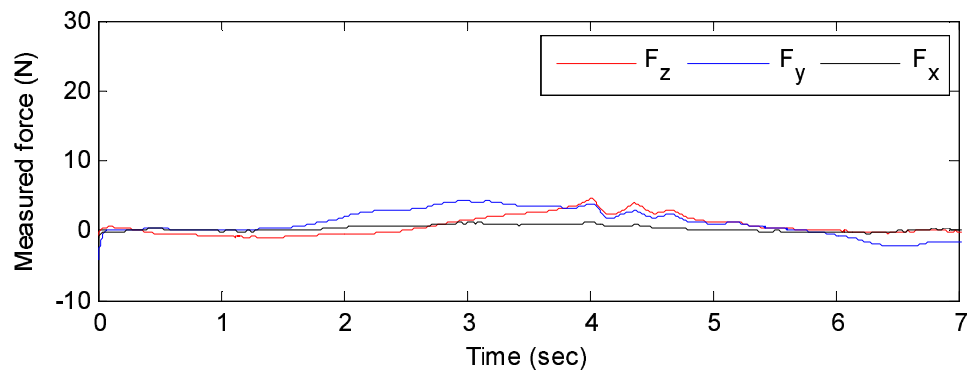


Figure 2-16: Measured forces during arm elevation with the vertically movable shoulder joint.

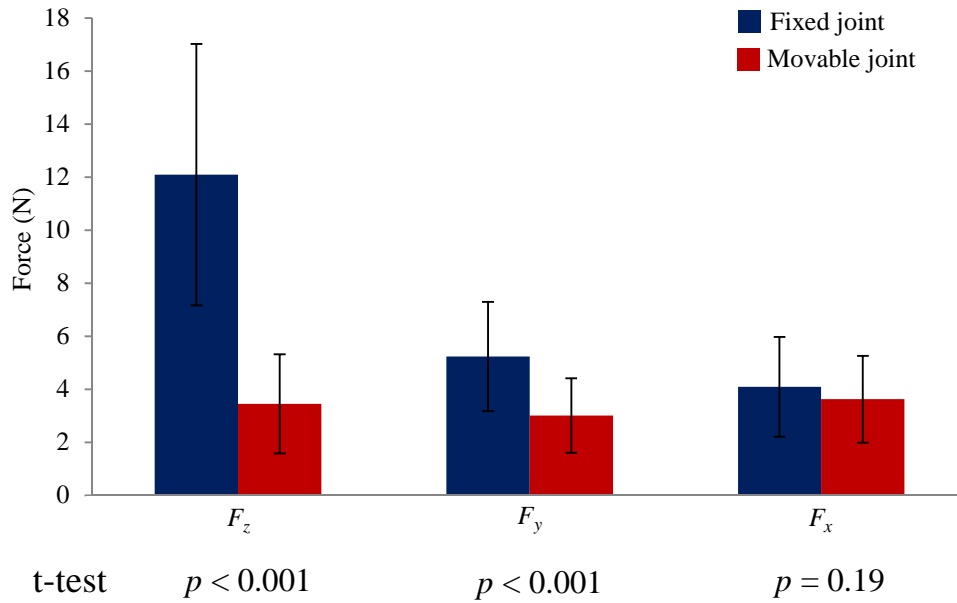


Figure 2-17: Statistical analysis of the measured forces during arm elevation.

installed force sensor. The weight of the force sensor and the exoskeleton itself were compensated by subtracting the weight of itself from the measured force in the z -direction. Each participant performed the experiment ten times.

Figure 2-15 shows one representative result of the calculated net shoulder elevation angle and measured force changes. The directions are specified in Fig. 2-13b. The z direction force force increases as the net shoulder elevation angle increases, which means the arm cannot be moved naturally by the fixed shoulder joint(Fig. 2-15b). Figure 2-16 shows a typical measured forced during arm elevation with the vertically movable joint. The vertical force (F_z) decreased significantly, compared with that of the fixed joint case.

Figure 2-17 shows the statistical analysis of the upper-limb exoskeletons with a fixed or vertically movable shoulder joint. The thick bars show mean values and the thin lines represent standard deviations of the data. The p -values from t-test were written below each graph. Note that the average of the maximum force in the vertical direction (F_z) of the fixed joint case was 12.09 N, which restricted the natural motion of the upper limb seriously. For the vertically movable joint case, the average of the maximum force in the vertical direction was much smaller. Also, it was shown that the difference of vertical forces was statistically significant indicated as the p -values in the figure. The vertical force of the vertically movable joint may be caused by friction of the guide rail, but it could be reduced in an actuated version of the exoskeleton.

The forces in the forward direction (F_y) were statistically different as shown in Fig. 2-17. Since

the vertically movable shoulder joint allowed free motion of the shoulder joint, the force might be less exerted than that of the fixed joint case even in the forward direction. The forces in the side direction (F_x) were not much different as shown in the figure.

These results imply that the proposed exoskeleton structure with the vertically movable shoulder joint can allow more natural upper-limb motion than the conventional exoskeleton structure with the fixed shoulder joint by reducing the compression force applied to the user's shoulder.

2.5.2 Motion Analysis

A camera-based motion capture system [68] was used to analyze the upper-limb movement with the proposed exoskeleton structure. The experimental setup and the analyzed tasks are shown in Fig. 2-18. The same participants of the force analysis experiments were asked to perform three tasks; forward flexion/extension, abduction/adduction and cross-body adduction/abduction, 1) wearing the exoskeleton with the fixed shoulder joint, and 2) wearing the exoskeleton with the vertically movable shoulder joint. Markers for the motion capture system were attached to the user's shoulder, elbow and wrist. The positions of these markers were captured while the participants were performing the tasks. To allow comparison of the three cases, each test was performed during the same time. The participants repeated the task for five times, and the position changes were normalized by the height of each participant. The normalized data of the fixed and vertically movable shoulder joints were compared using t-test. One of the representative results is shown in Fig. 2-19. As shown in the figure, the height changes of each joint using the exoskeleton with the vertically movable shoulder joint is larger than those of the vertically fixed shoulder joint case. The statistical analysis results for both cases are shown in Fig. 2-20. The mean values of height changes for all joints using the exoskeleton with the vertically movable shoulder joint were greater than those of the vertically fixed shoulder joint case. Also, the t-test demonstrated that these differences were statistically significant. These results imply that the proposed exoskeleton structure with the vertically movable shoulder joint allowed more natural upper-limb motion than the conventional exoskeleton structure with the fixed shoulder joint.

2.6 Summary

In this chapter, a 5-DOF upper-limb exoskeleton with a tilted shoulder joint that could be vertically translated was proposed and analyzed. The biomechanics of the shoulder joint were studied, and the

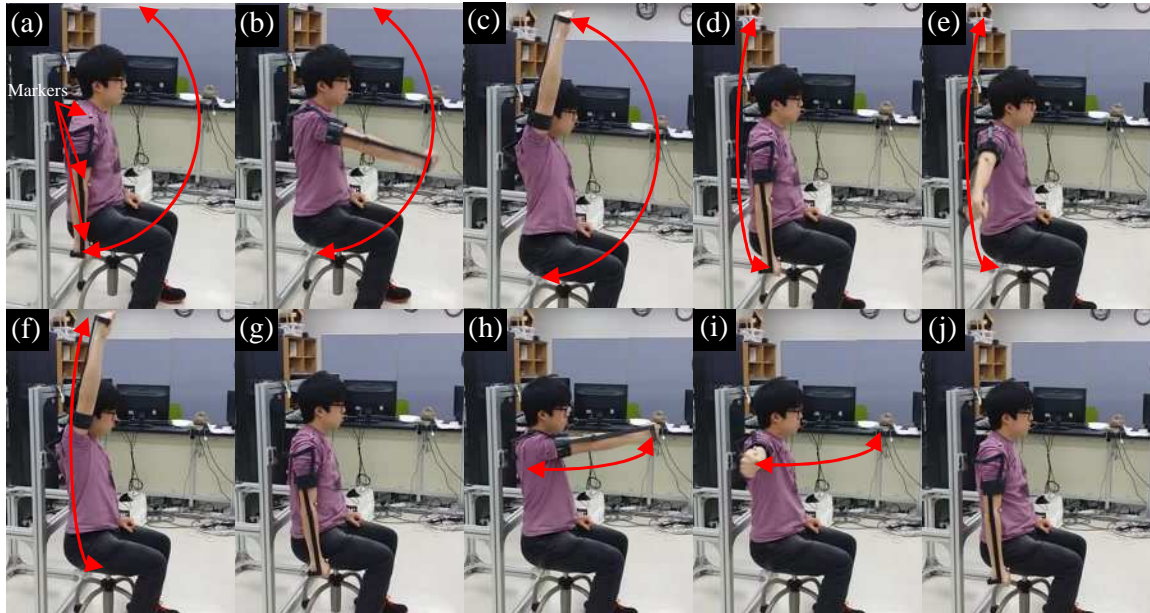
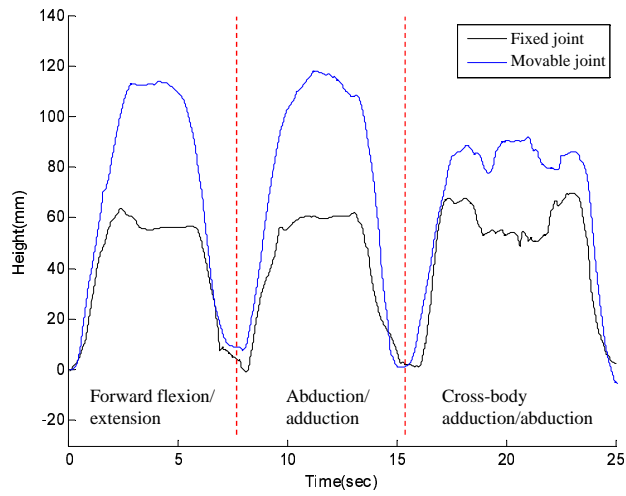
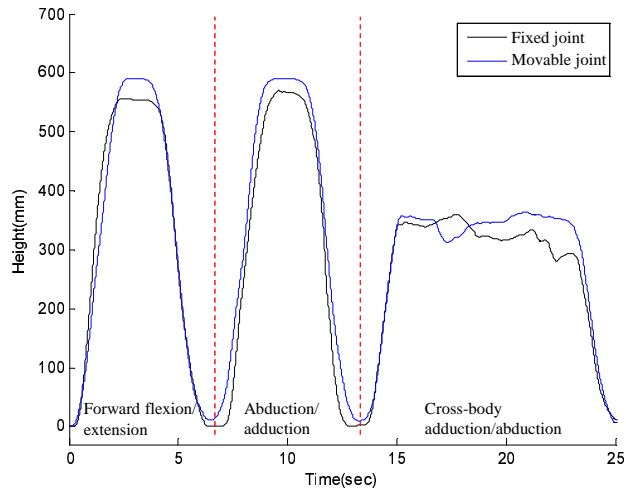


Figure 2-18: Performed tasks in the motion capture system : Forward flexion/extension ((a)-(d)), Abduction/adduction ((d)-(g)) and Cross-body adduction/abduction ((g)-(j))

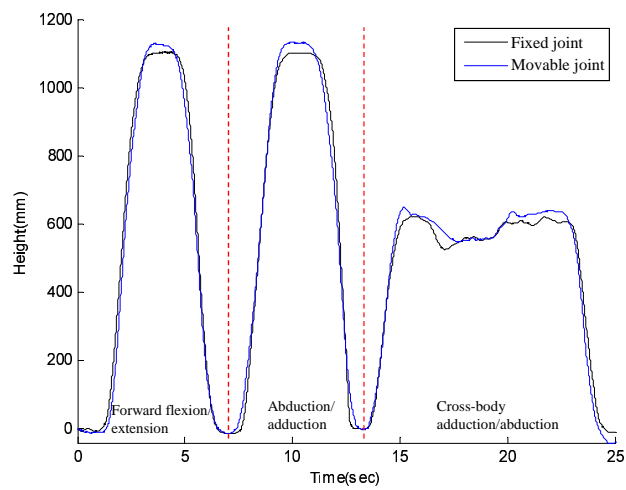
shoulder joint movement was approximated to a vertical motion. Additionally, the shoulder joint was tilted to have the singularity position outside of the arm workspace. Thus, a 5-DOF upper-limb exoskeleton with 4-DOF shoulder joint and 1-DOF elbow joint, was proposed. To verify that the proposed system was able to reach all points in the workspace, forward and inverse kinematics were applied. The joint positions changed with the shoulder elevation; thus, the joint angles were calculated iteratively. The simulated data showed that the full range of motion was accessible using the proposed upper-limb exoskeleton geometry. The experimental results showed that the proposed upper-limb exoskeleton with a vertically translating shoulder joint allowed for more natural motion of the arm, compared with an exoskeleton with a vertically fixed shoulder joint.



(a) Shoulder

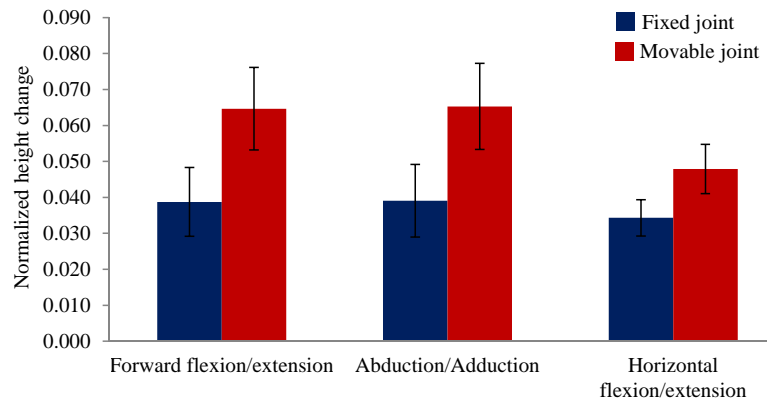


(b) Elbow



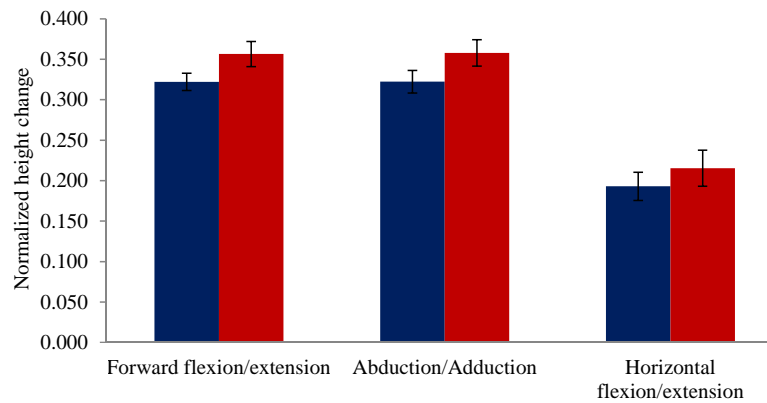
(c) Hand

Figure 2-19: Height change of each joint.



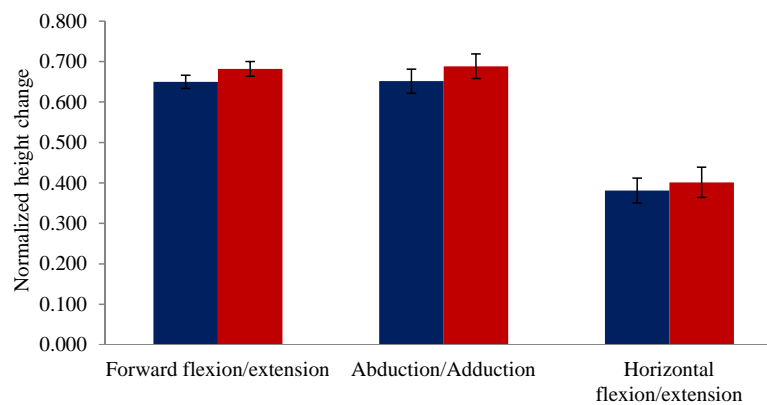
t-test $p < 0.001$ $p < 0.001$ $p < 0.001$

(a) Shoulder



t-test $p < 0.001$ $p < 0.001$ $p < 0.001$

(b) Elbow



t-test $p < 0.001$ $p < 0.001$ $p = 0.039$

(c) Hand

Figure 2-20: Statistical analysis of the height change.

Chapter 3

Cable-driven Mechanisms

Inertia and weight of a haptic control interface negatively affect to the force transparency and actuation bandwidth of a haptic control interface. The interface must be lightweight in order to deliver desired forces to the user precisely. Also, compact structure is required to prevent the interference with user's body. Cable-driven mechanisms have been used to satisfy such requirements, but they have suffered from many problems in multi-DOF systems, such as bulky cable routing structure, friction and pretension change. In this chapter, two cable-driven mechanisms are developed to achieve lightweight and compact actuation system addressing the limitation of conventional cable-driven mechanisms.

3.1 An Asymmetric Cable-driven Mechanism¹

3.1.1 Introduction

Most of the weight of multi-degrees of freedom (DOFs) actuation systems comes from directly mounted actuators. They become even heavier in case of series manipulators, because the proximal actuators are required to hold the weight of the distal actuators. To remove the heavy actuators and associated structures, cable-driven mechanisms have been adopted in many robotic manipulation systems [69–77]. In such cable-driven mechanisms, the actuators are placed at the base, and the force is transmitted through cables. Cable-driven mechanisms have also been widely applied in human-robot interaction systems, such as exoskeleton systems, because they enable a light and compact wearable structure [27,57]. Such exoskeleton systems were usually developed as rehabilitation

¹The contents of this chapter was published in [4]. A preliminary research result of the paper was published in [5]. Reprinted with permission from IEEE and Elsevier.

and haptic devices for the communication with a virtual environment, which require precise force control. Also, their structures have to be compact to ensure safety of the users from collision, and to enhance the performance of system with less inertia. In many cable-driven systems, cables are routed through low-friction idler pulleys. Neglecting the inertia of idler pulleys, such pulley-based cable mechanisms can deliver the desired force without large loss. However, their complex cable routing mechanism can make the systems bulky and heavy in case of multi-DOF systems, because idler pulleys are required for every tendon sets at each intermediate joints. Also, flexible cables that can transmit only pulling forces provide challenges in delivering precise force to the human user.

In Chapter 3.1, a spring-actuator type cable-driven mechanism is proposed for force control of exoskeleton systems with compact cable routing structures, addressing the limitations of conventional pulley-based cable-driven mechanisms. In the proposed system, a linear spring acts as a power source as well as a tensioner by pulling the cable against the actuator. Because the required joint torques of human motions are not symmetric in many cases [78–80], the spring-actuator mechanism is a feasible solution with a simple cable routing structure and a self-tension mechanism. A rotary series elastic mechanism and robust control algorithms were applied with the cable-driven mechanism to enable high performance force control. Since the desired force can be delivered precisely with a simple cable routing structure, the proposed system is expected to be used in the exoskeleton systems for haptic and rehabilitation purpose that require lightweight and compact structures and precise force control.

3.1.2 Configuration of an Asymmetric Cable-driven Mechanism

3.1.2.1 Cable-driven Mechanism

In a pulley-based cable-driven system, the torque generated by an actuator is transmitted through flexible cables. Because the cables can transmit forces only in the pulling direction, the cables pulled in two different directions are required for the actuation of one DOF rotational joint. To satisfy such requirements, the three structures in Fig. 3-1 have been used as basic pulley-based cable-driven mechanisms.

In the first mechanism, two actuators pull each cable independently (Fig. 3-1a). This mechanism provides high performance and a relatively easy cable routing structure because the tensions of both cables are controlled by different actuators. Also, the joint stiffness can be adjusted easily by antagonistic control of the two actuators [69, 81]. However, the number of required actuators is

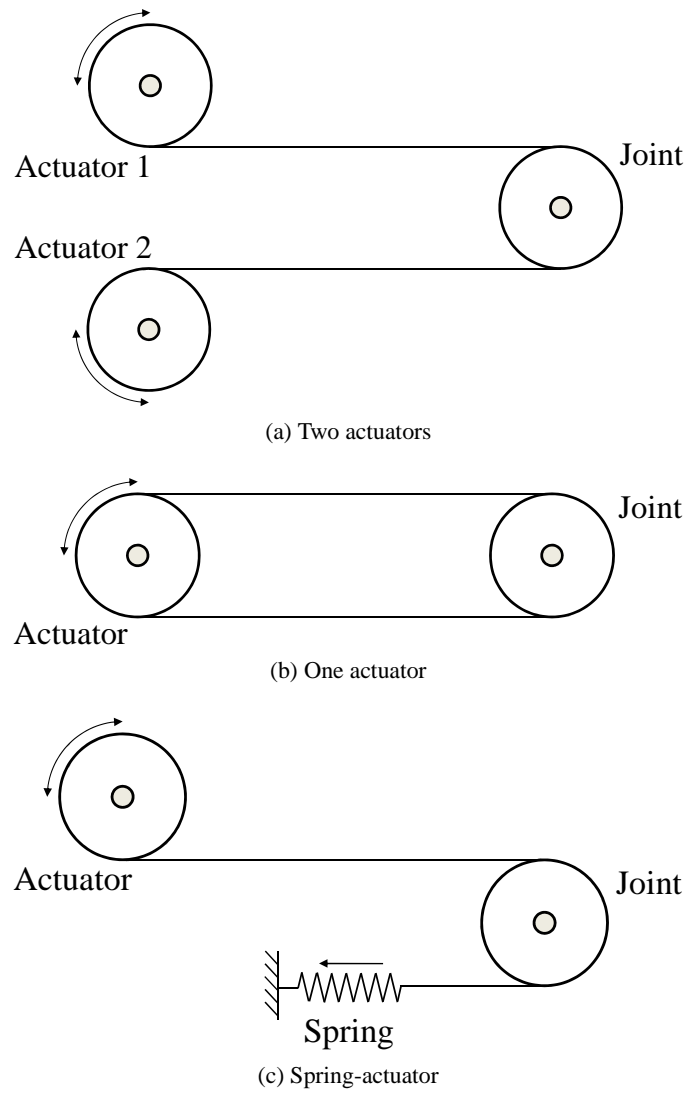


Figure 3-1: Cable-driven mechanisms.

doubled compared with other mechanisms.

In contrast, the mechanism shown in Fig. 3-1b can actuate one joint with one actuator. Due to its simple structure, it has been used for several robotic manipulators including exoskeleton systems [27, 30, 57, 70]. Due to the nature of the mechanism, idler pulleys are required for routing the cables through other joints. However, one idler pulley cannot enlarge the range of motion sufficiently (Fig. 3-2a). The middle joint cannot be rotated further clockwise in this figure, because the lower routed cable will be separated from the idler pulley. Small additional idler pulleys can enlarge the motion range of joints (Fig. 3-2b), but this requires bulky structures in series manipulators with many DOFs. For example, a serial type 7-DOF exoskeleton may require six main idler pulleys and 12 small idler pulleys just at the first joint for the routed cable of the next six joints. Also, the cable of the non-pulled side is easily slackened, which causes backlash and slow responses. Thus, pretensioning mechanisms in the hardware and/or software are essential. For the pretension of cable-driven mechanisms, mechanical components, such as spring, idler pulleys and screws, were typically used [34, 82–84]. Such tensioners made the cable-driven structure bulky and heavy, and required frequent adjustment for maintaining appropriate tension. Slack enable mechanisms were developed to use cable-driven systems in soft wearable robots without pretension in [85, 86]. However, they are not applicable for pulley-based cable-driven systems, because the slacked cable could be derailed from the pulley.

The spring-actuator mechanism, shown in Fig. 3-1c, uses an antagonistic spring for the actuation of one side, while the other side is driven by an actuator. The spring is pretensioned by pulling it with the actuator to apply two directional forces to the joint. The amount of force to the spring side is determined by this pretension and the stiffness of spring. The available actuator force is smaller than other mechanisms when the same actuator is used, because the actuator is required to pull the spring. However, as the spring naturally pulls the cable, the cable tension can always be maintained appropriately without additional components. More important thing is that its cable routing mechanism is much simpler than other mechanisms. The mechanism provides an almost full range of motion in the flexion direction without additional idler pulleys (Fig. 3-2c). When the joint requires extension motions, just one additional idler pulley for each proximal joint and itself is sufficient to enlarge the range of motion (Fig. 3-2d). Due to the simple cable routing mechanism of the spring-actuator mechanism, it was adopted in some hand exoskeletons and robotic hands that requires compact structures [71–73, 87–89].

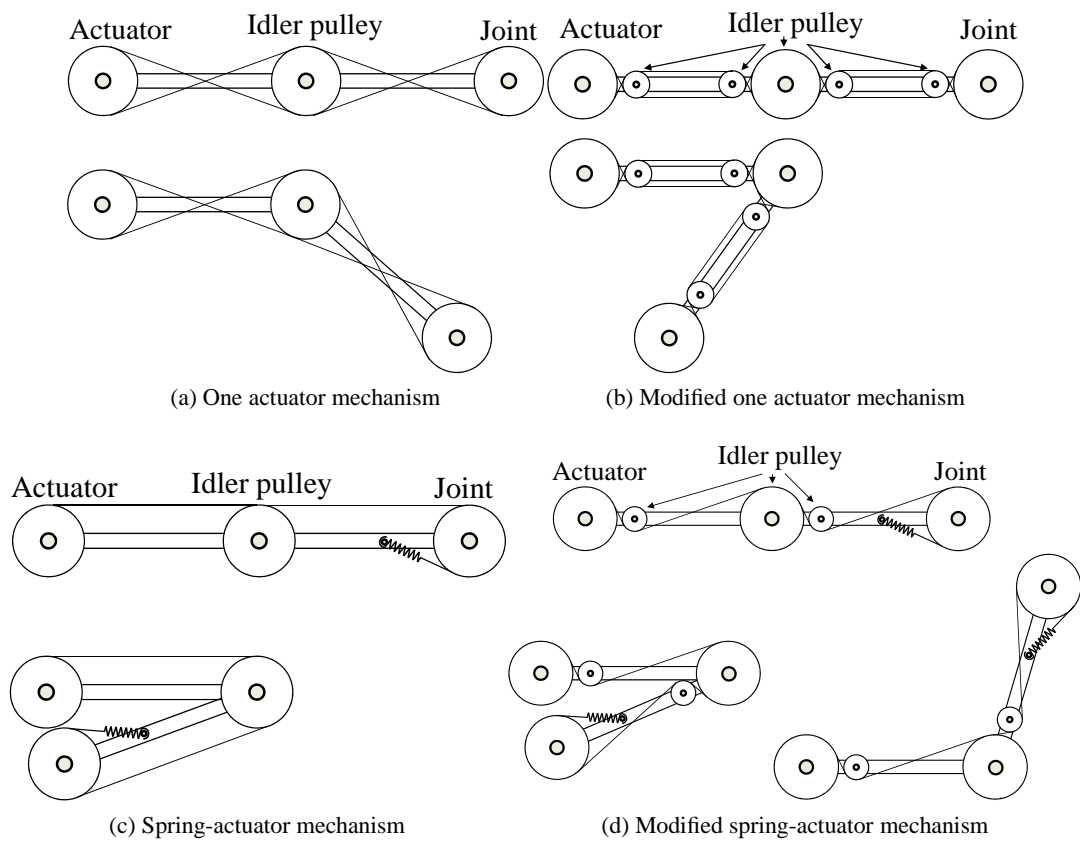


Figure 3-2: Range of motions of the one actuator mechanism and the spring-actuator type mechanism.

Table 3.1: Elbow joint torque in flexion and extension.

	Flexion (kg·cm)	Extension (kg·cm)
Men	725±154	421±109
Woman	336±80	210±61

3.1.2.2 Spring-actuator Mechanism for Asymmetric Force Requirement

The required joint torques of human motion are not symmetric in many cases, which inspired us to design an asymmetric actuating mechanism. One example of asymmetric joint torques is shown in Table 3.1 [79]. As shown in the table, the flexion torque of the human elbow joint is much larger than the extension torque, because the elbow joint is usually used to lift and carry objects against the gravity, which requires the flexional torque of elbow joint [79]. This asymmetry appears not only in the elbow, but also in the knee joint [78] and the finger [80] due to similar reasons.

Among the cable-driven mechanisms mentioned above, the first two mechanisms try to rotate the joint with the same force in both directions, but the spring-actuator mechanism can adjust the asymmetric force using a linear spring with an appropriate spring constant. As mentioned in the previous chapter, the motor is required to pull the linear spring at all time in the spring-actuator mechanism; thus, the available force is smaller than other cable-driven mechanisms. Therefore, the advantage, i.e. simple and light cable routing structures, may be shaded by the disadvantage. However, the asymmetry of the spring-actuator mechanism allows compensating the disadvantage by properly setting its asymmetry similar to the asymmetry of required torque.

Human joints are asymmetric in most cases, and the exoskeletons for human limbs usually require multiple DOFs in series, which leads to bulky and heavy cable routing structures. Thus, in this study, the spring-actuator mechanism, which allows a simple cable routing structure, was selected for the exoskeleton actuation mechanism.

3.1.2.3 Rotary Series Elastic Mechanism

In human-robot interaction systems, force control is essential for intelligent interaction such as impedance control [90]. In this chapter, a rotary series elastic mechanism is combined with a spring-actuator type cable-driven mechanism for force control. The series elastic mechanism has been widely used for human-robot interaction systems for force control and improved safety [44,91–94].

In the series elastic mechanism, an elastic element (i.e., a spring) is installed between the human and exoskeleton joint. By controlling the spring deflection, the force transmitted to the human can be controlled. In this proposed mechanism, a torsional spring is directly applied to the joint.

3.1.2.4 System Configurations

A schematic of the proposed system is shown in Fig. 3-3. In this system, the drive pulley is rotated by a cable whose one end is connected with a motor and the other end is connected with a linear spring. As the motor rotates to the counterclockwise direction, the drive pulley is rotated in clockwise direction, and the linear spring is extended. In similar way, the linear spring pulls the drive pulley when the motor rotates to the clockwise direction. This drive pulley is connected with the exoskeleton frame via a torsional spring, which makes a rotary series elastic mechanism. By controlling the drive pulley angle to have an appropriate torsional spring deflection with respect to the exoskeleton frame worn by a human user, the series elastic mechanism enables to deliver the desired force accurately to the human user.

Because the linear spring is needed to prevent the cable slack and pull the cable, the spring is pretensioned as $L_1 - L_0$, where L_0 and L_1 are the free and pretensioned lengths of the linear spring, respectively. Thus, the linear spring generates the pulling force at least T_i as:

$$T_i = k_L(L_1 - L_0) \quad (3.1)$$

where k_L is the spring constant of the linear spring. Because the amount of pretension determines the force asymmetry, the pretension should be carefully designed considering required asymmetry force and structure stiffness.

3.1.3 Control of the Asymmetric Cable-driven System

3.1.3.1 System Modeling

In the proposed system, the motor should be able to control the drive pulley position precisely so that the desired force can be transmitted to the human through the rotary series elastic mechanism. To find the relationship between the motor torque, τ_M , and the drive pulley angle, θ_D , the system in

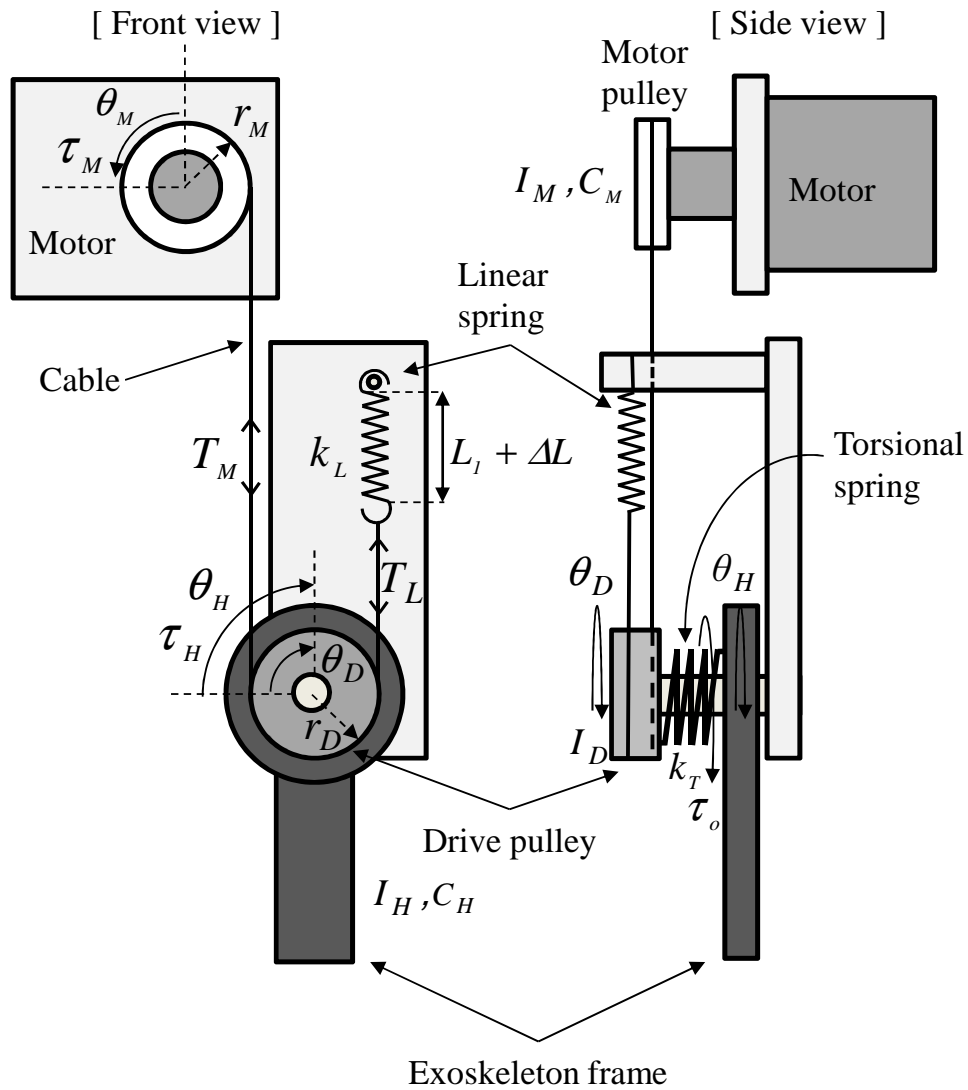


Figure 3-3: Schematics of the proposed asymmetric cable-driven mechanism. [Refer Chapter 3.1.3.1. for the notations in the figure.]

Fig. 3-3 is modeled as follows:

$$I_M \ddot{\theta}_M + C_M \dot{\theta}_M = \tau_M - T_M r_M \quad (3.2)$$

$$I_D \ddot{\theta}_D = r_D (T_M - T_L) + k_T (\theta_H - \theta_D) \quad (3.3)$$

$$I_H \ddot{\theta}_H + C_H \dot{\theta}_H = k_T (\theta_D - \theta_H) + \tau_H \quad (3.4)$$

where I_M and C_M are the inertia and damping coefficient of the motor, I_H and C_H are those of human, I_D is the inertia of the drive pulley, θ_M , θ_D and θ_H are the rotation angle of the motor, drive pulley and human, respectively, k_T is the spring constant of the torsional spring, r_M and r_D represent the pulley radius of the motor and drive pulley, respectively, T_M and T_L are the tension of each cable, τ_M is the motor torque and τ_H is the human torque.

By assuming that the appropriate cable tension is maintained by the linear spring, the relationship between the motor angle, θ_M , and the drive pulley angle, θ_D , is obtained kinematically as follows:

$$r_D \theta_D = r_M \theta_M \quad (3.5)$$

The linear spring is extended by ΔL from the pretensioned position, and the cable tension by the linear spring, T_L , is calculated by Hooke's law as follows:

$$\begin{aligned} T_L &= k_L (L_1 - L_0 + \Delta L) \\ &= k_L (L_1 - L_0 + r_D \theta_D) \end{aligned} \quad (3.6)$$

The output torque, τ_o , from the rotary series elastic mechanism is also calculated by deflection of the torsional spring as follows:

$$\tau_o = k_T (\theta_D - \theta_H) \quad (3.7)$$

By integrating (3.2)-(3.7), the drive pulley angle is expressed in the Laplace domain as follows:

$$\theta_D(s) = \frac{\frac{1}{r_M I'}}{s^2 + \frac{C'}{I'} s + \frac{k' + k_H}{I'}} (\tau_M(s) - \tau_i(s) + \tau_H'(s)) \quad (3.8)$$

where

$$I' = \frac{r_D}{r_M^2} I_M + \frac{1}{r_D} I_D \quad (3.9)$$

$$C' = \frac{r_D}{r_M^2} C_M \quad (3.10)$$

$$k' = k_L r_D \quad (3.11)$$

$$k_H(s) = \frac{1}{r_D} k_T (1 - k_T G_H) \quad (3.12)$$

$$G_H(s) = \frac{1}{I_H s^2 + C_H s + k_T} \quad (3.13)$$

$$\tau_i(s) = \frac{1}{s} r_M T_i \quad (3.14)$$

$$\tau'_H(s) = r_M G_H(s) \tau_H(s) \quad (3.15)$$

Note that G_H contains human-related parameters such as I_H and C_H , which are difficult to be measured. Even more, they are not constant values because physical properties of human muscle changes [95]. Thus, the nominal model of the system was obtained by letting I_H and C_H to zero for simplicity, and variation of such variables were dealt as modeling uncertainties. Then, G_H and k_H become to $\frac{1}{k_T}$ and 0, respectively. Thus, the nominal model of drive pulley angle is simplified as follows:

$$\theta_D(s) = \frac{\frac{1}{r_M I'}}{s^2 + \frac{C'}{I'} s + \frac{k'}{I'}} (\tau_M(s) - \tau_i(s) + \tau''_H(s)) \quad (3.16)$$

where $\tau''_H(s) = \frac{r_M}{k_T} \tau_H(s)$. The last term in (3.16) which is by human joint torque is treated as external disturbance to the controller. Both the modeling uncertainties and external disturbances caused by the interaction with human are compensated by robust control algorithms discussed in next chapter.

3.1.3.2 Controller Design

A model-based robust control structure is proposed in this chapter for force control of the system. Because the system delivers the desired force to the human via the series elastic mechanism, the position control of drive pulley angle, θ_D , may be the main issue of the proposed control algorithms.

Before system identification, the initial linear spring force T_i was measured to compensate $\tau_i(s)$ from the system model in (3.16). As the motor input was increased gradually, the lengths of the

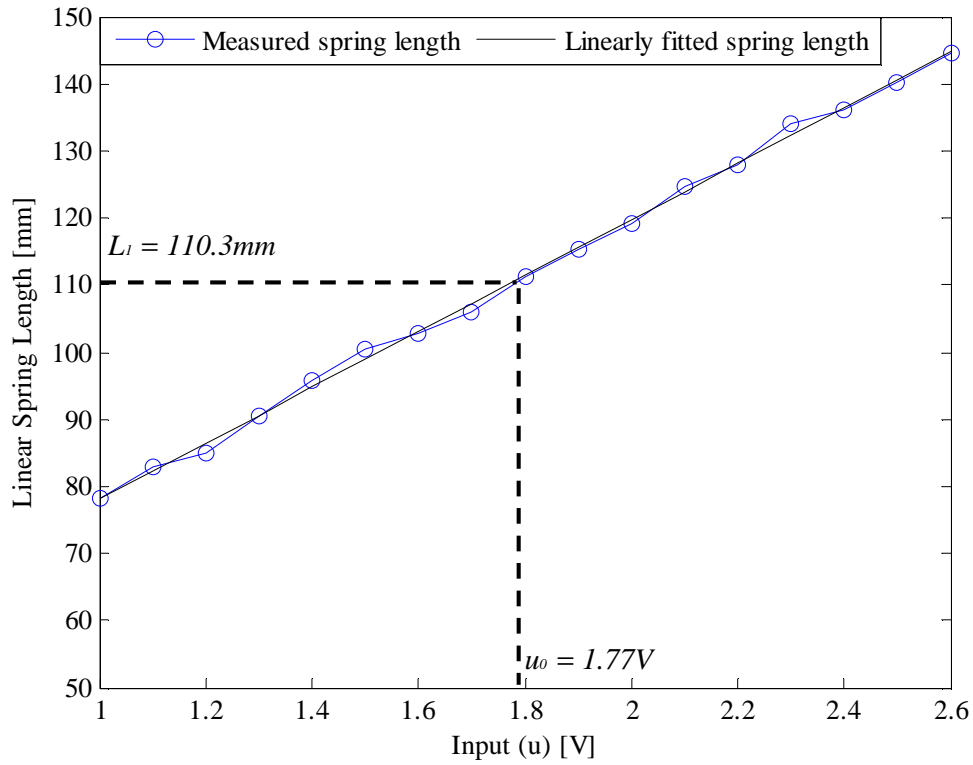


Figure 3-4: Determination of u_0 by measured and linearly fitted linear spring length.

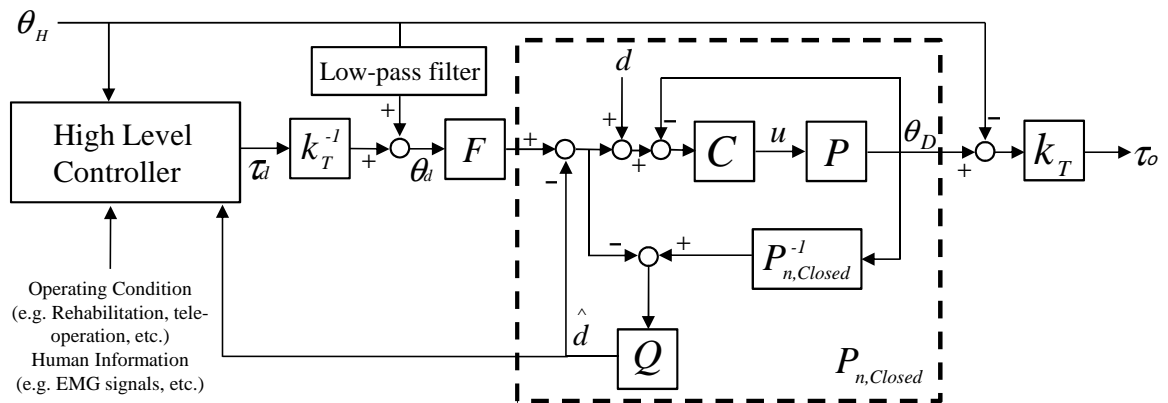


Figure 3-5: Block diagram of the control structure. [θ_H is the position of exoskeleton in human side, d is a disturbance, τ_d is the desired torque determined by the high level controller, k_T is the torsional spring stiffness, F denotes the feedforward filter, C is the PD controller, P is the plant model of motor, $P_{n,Closed}^{-1}$ is the inverse of closed-loop transfer function of C and P , Q is the low-pass filter for the disturbance observer and τ_o denotes the output torque.]

linear spring in the stationary state was measured. In a stationary state, T_L and T_M can be assumed to be equal. Thus, the generated τ_M by the control inputs is the required torque to generate the same magnitude of T_M as T_L . Consequently, the input shows a linear relationship with the linear spring length as shown in Fig. 3-4. To calculate the input magnitude for compensating τ_i , the measured data were linearly fitted. The motor input to extend the linear spring to L_1 was calculated inversely from the fitted equation, and it is denoted by u_0 (i.e. u_0 generates T_M with the magnitude of T_i). In the system identification and the following experiments, the motor input, u , was set as :

$$u = u_c + u_0 \quad (3.17)$$

where u_c is the control input from the controller and u_0 is the input for compensating τ_i . Because u_0 generates motor torque with a magnitude of $r_M T_i$, the motor torque is expressed as :

$$\tau_M = \tau_c + \tau_i \quad (3.18)$$

Then, the system model in (3.16) is simplified to:

$$\theta_D(s) = \frac{1}{s^2 + \frac{C'}{I}s + \frac{k'}{I}} (\tau_c(s) + \tau_H''(s)) \quad (3.19)$$

The torsional spring was excluded during system identification because $\tau_H''(s)$ is treated as a disturbance in the position control. Thus, the system consisting of the motor, drive pulley, linear spring and cables was identified by sweeping sinusoidal signals, which have frequency from 1 Hz to 60 Hz with 2.5 V of magnitude. By fitting the parameters in (3.19) to the measured data as in Fig. 3-6, the nominal model of the system was identified as follows:

$$P_n(s) = \frac{15.41}{s^2 + 3.545s + 6.39} \quad (3.20)$$

As a basic controller, a proportional-differential (PD) controller was applied, whose gains were obtained by the linear quadratic (LQ) method. The LQ performance index is defined as follows:

$$J = \int_0^{\infty} (x^T Q x + u^T R u) dt \quad (3.21)$$

where x denotes the state, including the position and velocity of the motor, and u is the input. Q

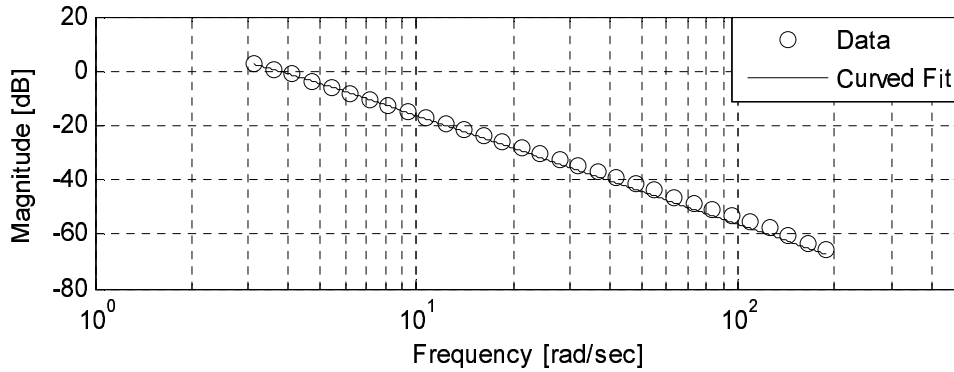


Figure 3-6: Frequency response of the system.

and R in (3.21) present the weighting factors of the position and speed of the drive pulley and of the control input, respectively. Using the performance index, the optimal PD gain was calculated for the controllable canonical form of (3.20).

The PD controller may not be sufficiently robust for this application, because an external disturbance and modeling uncertainties are introduced by interaction with human as in (3.19). Unlike the linear spring force, the disturbance introduced by human force and the modeling uncertainties cannot be directly compensated. Thus, a robust control algorithm is applied with the nominal model in (3.20). Disturbance observer (DOB) is one of the representative robust control algorithms, which can estimate and compensate the external disturbance [96]. The modeling uncertainties from a nominal model can be also compensated by dealing with the modeling uncertainties as equivalent disturbances. Thus, it is expected that the induced modeling uncertainties by in (3.19) can be canceled by the DOB.

To implement the DOB, we need to properly design the Q -filter to make the DOB algorithm realizable. Because the inverse of $P_{n,Closed}^{-1}(s)$ is not realizable, the Q -filter must have equal or higher relative order than that of $P_{n,Closed}$. Thus, $Q(s)$ was designed to have the same relative order of $P_{n,Closed}^{-1}(s)$ in this study. Because the maximum bandwidth of the human elbow is 4-6 Hz [97], the Q -filter was designed as a low-pass filter with a 10 Hz of cutoff frequency. The entire system was discretized with a sampling time of 1 ms for implementation in the digital control system.

Once the robustness of the closed-loop plant is secured by the DOB, a significant improvement in tracking performance can be expected by introducing a feedforward controller. In this study, the zero phase error tracking (ZPET) method was used [98]. Because the nominal model of the

Table 3.2: Specifications of experimental setup.

	Specification
Motor	Maxon EC-4pole Gear ratio : 74:1 Nominal speed : 22.5 rad/s Nominal torque : 6.767 Nm
Driver	Maxon ESCON 70/10
DAQ	National Instruments PCIe-7841R
Encoder	US Digital, Incremental, 1250 CPR
CPU	Intel i7-3770
Operating System	Microsoft Windows 7
Softwares	National Instruments LabVIEW 2015

closed-loop is known, the ZPET controller, F , was designed as:

$$F = P_{n,Closed}^{-1} z^{-1} \quad (3.22)$$

The overall controller structure is shown in Fig. 3-5. Suppose the desired torque, τ_d , is given by a high level controller, which could be for rehabilitation or tele-operation, etc. Then, the desired drive pulley angle, θ_d , is calculated by the series elastic mechanism with the measured human joint angle, θ_H . By the DOB algorithm, the closed loop system is expected to act as $P_{n,Closed}$, and the ZPET controller, F , drastically improves the tracking performance. The measured drive pulley angle, θ_J , is used to make the output torque, τ_o with the measured human joint. A low-pass filter was applied to θ_H in determining θ_d , to reduce high frequency movement that may cause the instability of the DOB.

3.1.4 Experimental Verification

3.1.4.1 Experimental Setup

A one DOF upper limb exoskeleton with the proposed system was manufactured for the elbow as shown in Fig. 3-7. A linear spring, which generates a smaller force than the motor, was used for flexion motion, but it can also be positioned for extension motion for a different purpose. The

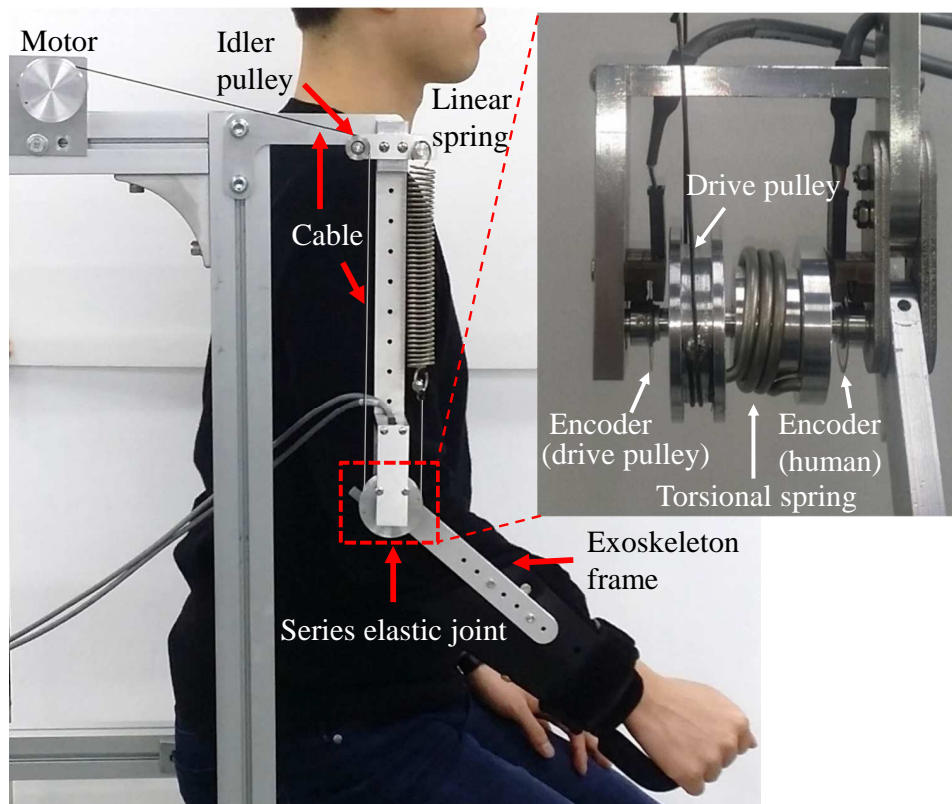


Figure 3-7: A prototype of the proposed mechanism for the elbow joint.

specifications of equipments in the experiment are shown in Table 3.2. The torsional spring was designed to have a spring constant of 1.17 Nm/rad, and the linear spring was designed to have a spring constant of 1.19 N/mm with initial length of 52.5 mm. The motor pulley and drive pulley had a radius of 21 mm. The pretension length was set to 110.3 mm considering the average required torque of the elbow joint in daily life, 1.4 Nm, could be generated at all times [27]. The maximum torque of the spring is 2.6 Nm at the maximum extension of the elbow. The expanded image in Fig. 3-7 shows the series elastic joint of the system. A torsional spring was placed between the drive pulley and the exoskeleton, and two encoders for the human joint and drive pulley were used to measure the spring deflection, thus torque transmitted to the human joint can be calculated.

3.1.4.2 Experimental Verification without Human Interaction

The bandwidth of the closed loop system with proposed control algorithms was verified as shown in Fig. 3-8. The frequency response of the closed system was flat until about 10 Hz. Thus, the performance of the actuation part was sufficient to follow the motion of the elbow, which is up to 4~6 Hz [97].

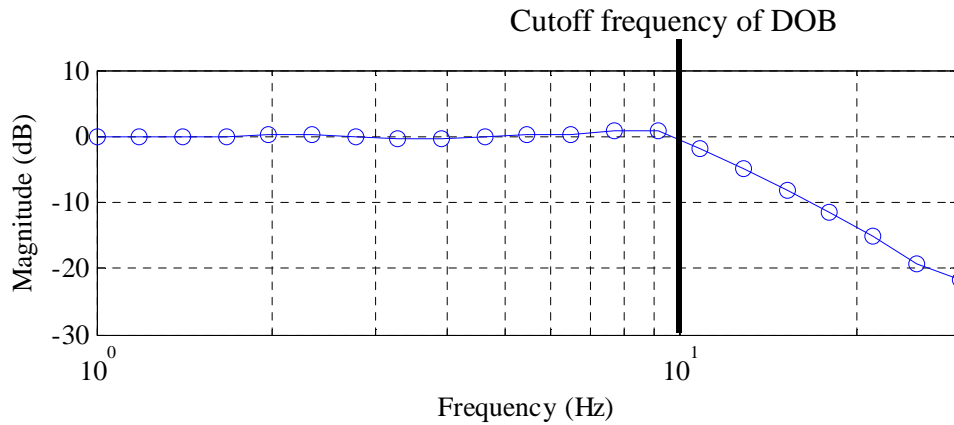


Figure 3-8: Frequency response of the system without the torsional spring and human parts.

The position tracking performance of the system was tested with and without an intentional disturbance with three control methods: (a) PD controller, (b) PD controller and DOB, (c) PD controller, DOB and ZPET. In this experiment, the desired drive pulley angle was provided as pre-programmed arbitrary trajectory. The drive pulley was not connected to the torsional spring or human part. As shown in Fig. 3-9 and Table 3.3, the tracking errors of PD and PD plus DOB control were quite small; however, the tracking error of the PD, DOB plus ZPET control was extremely small compared with those of PD and PD plus DOB.

However, the results changed significantly when an external disturbance was introduced. A sinusoidal disturbance was inserted in the digital controller as d in Fig. 3-5. Figure 3-10 and Table 3.3 shows the experimental results with the same desired angle, with the intentional sinusoidal disturbance. In the PD controller case, the tracking error under PD control increased significantly. However, PD plus DOB controller maintained a similar level of tracking error as that without a disturbance. These results show that the DOB is capable of observing and rejecting the disturbance. The last graph in Fig. 3-10 compares the inserted disturbance and estimated disturbance by the DOB, confirming the performance of the DOB. Thanks to the robustness of the DOB, the use of the feedforward filter, ZPET, significantly increased the tracking performance similar to the previous experiment.

3.1.4.3 Experimental Verification with Human Interaction

In the previous chapter, performance of the proposed mechanism without a human user was verified. However, its performance may depreciate if unknown disturbances are introduced by human interaction. To confirm that the system can transmit desired torque even with human interaction, the

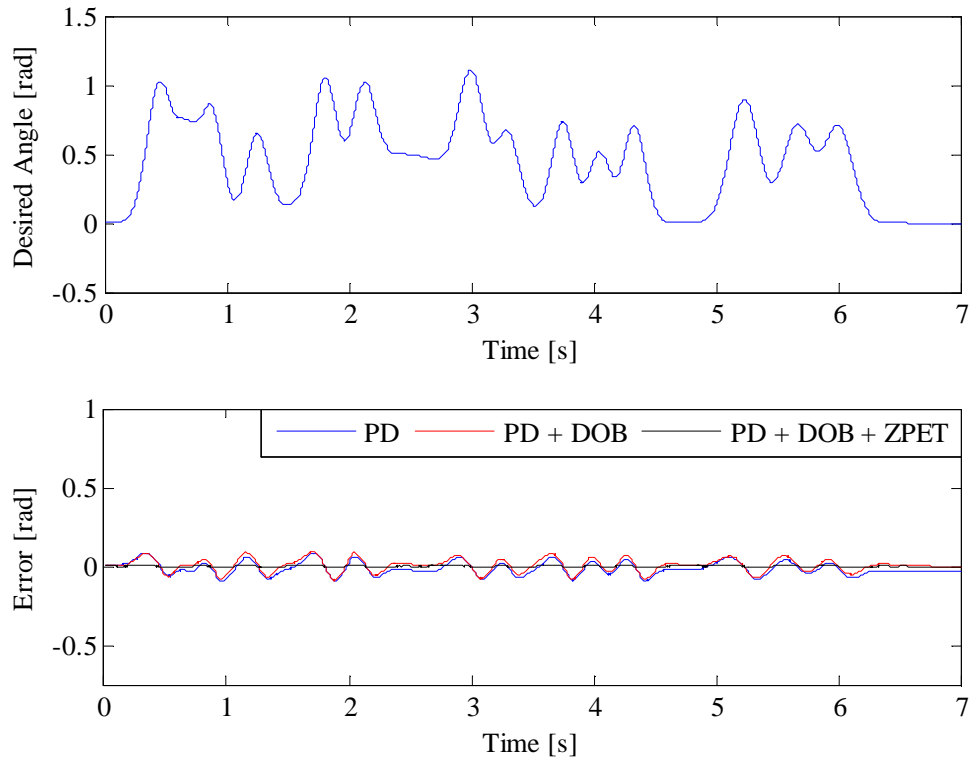


Figure 3-9: Position tracking performance without inserting a disturbance. The torsional spring and human parts are excluded, i.e., no interaction with the user.

Table 3.3: Root mean square (RMS) errors in the experiments without a user.

Controller	Without disturbance (rad)	With disturbance (rad)
PD	0.0434	0.3587
PD+DOB	0.0419	0.0455
PD+DOB+ZPET	0.0045	0.0188

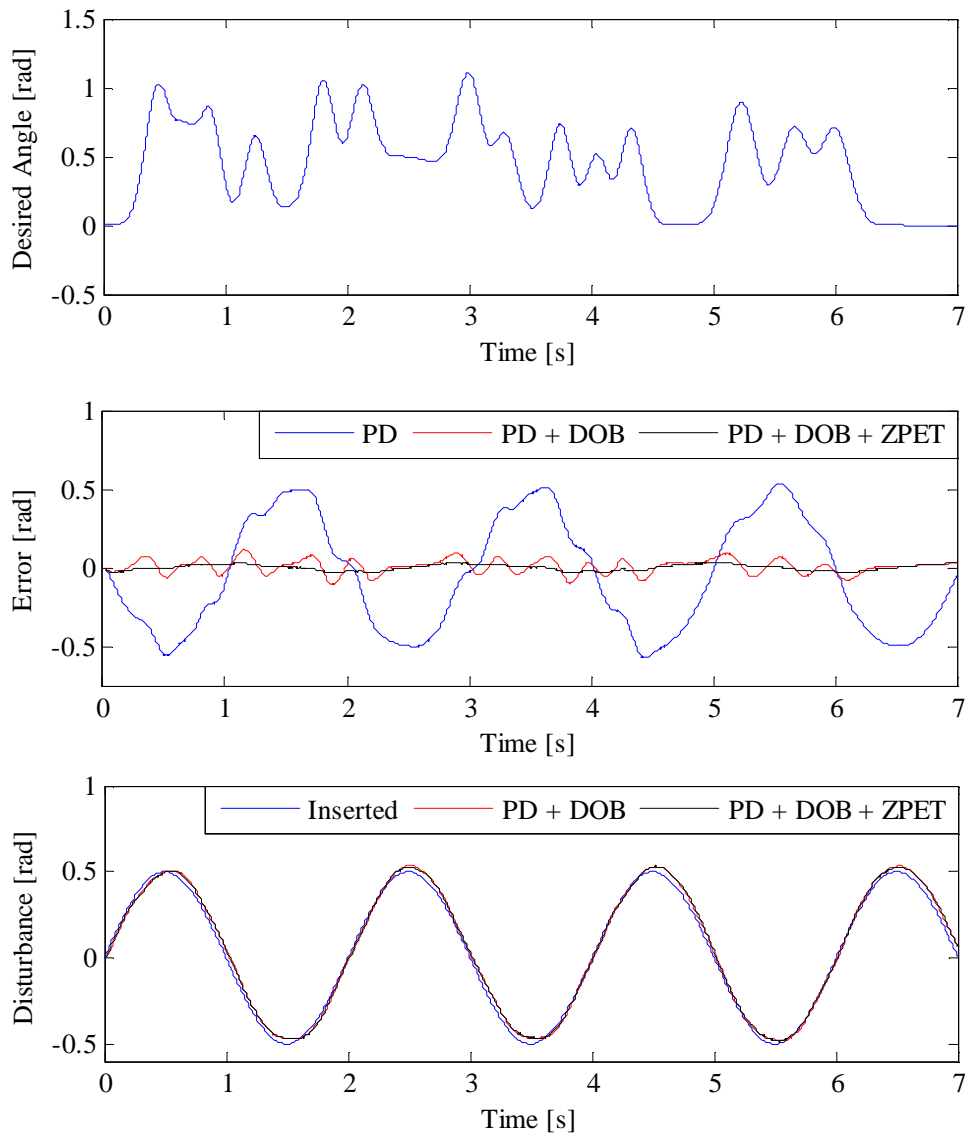


Figure 3-10: Position tracking performance and the disturbance observation with a sinusoidal disturbance. The torsional spring and human parts are excluded, i.e., no interaction with the user.

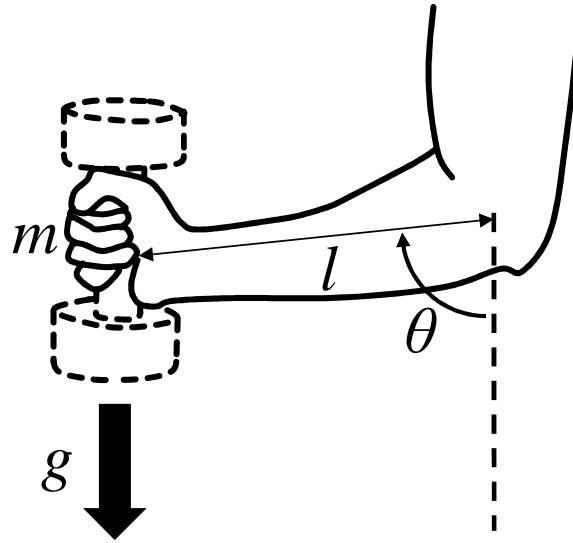


Figure 3-11: Schematics and parameters for the virtual dumbbell experiment. m : mass of a virtual dumbbell, g : gravity, l : distance between the center of rotation of elbow joint and the hand, θ : elbow flexion angle.

experiment with a human user was performed. As mentioned earlier, this mechanism is developed for the haptic interface with an exoskeleton structure; thus, the experiment with a human user is highly necessary.

In the experiments, the user wore the proposed exoskeleton system and moved arbitrarily. Four types of torques were applied to the system. First, the desired torque was set to zero to prove that this mechanism is enough back-drivable to ensure free motion of the user. The second type of torque was set as a sinusoidal torque, to verify that this mechanism can generate torque to both directions with given frequency. The third type of torque was set to the force from a virtual dumbbell as shown in Fig. 3-11, supposing the mechanism was applied in a haptic device for the communication with a virtual reality. Considering the inertia and gravity of the virtual dumbbell, the desired torque was set as follows, by assuming point mass.

$$\tau_d = ml^2\ddot{\theta} + mgl \sin \theta \quad (3.23)$$

The mass of the dumbbell, m , was set to 0.8kg, and the distance between the center of rotation of elbow joint and the hand, l , was set to 0.35m in the experiment. The range of elbow flexion angle, θ , was set to 0° to 135° .

In the last experiment, the desired torque was set to a measured torque of a robot arm, to test the feasibility as a haptic control interface with a robot arm. As shown in Fig. 3-12, a robot arm

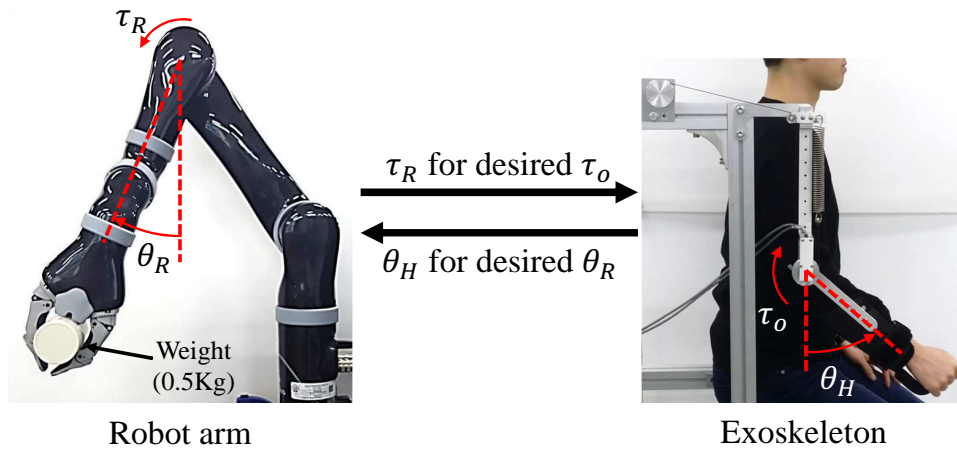


Figure 3-12: Interaction between a robot arm and the exoskeleton]. θ_R and θ_H are joint angles of the robot joint and the human elbow, τ_R is the measured reaction torque of the robot joint, and τ_o is the generated torque by the exoskeleton system.

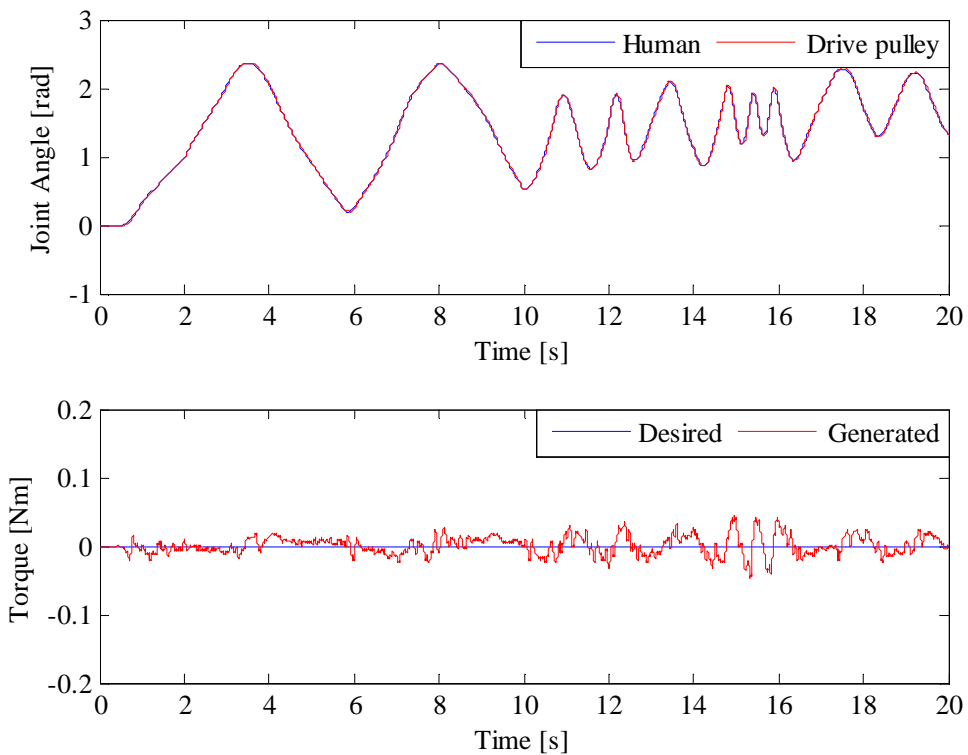


Figure 3-13: Backdrivability test of the system.

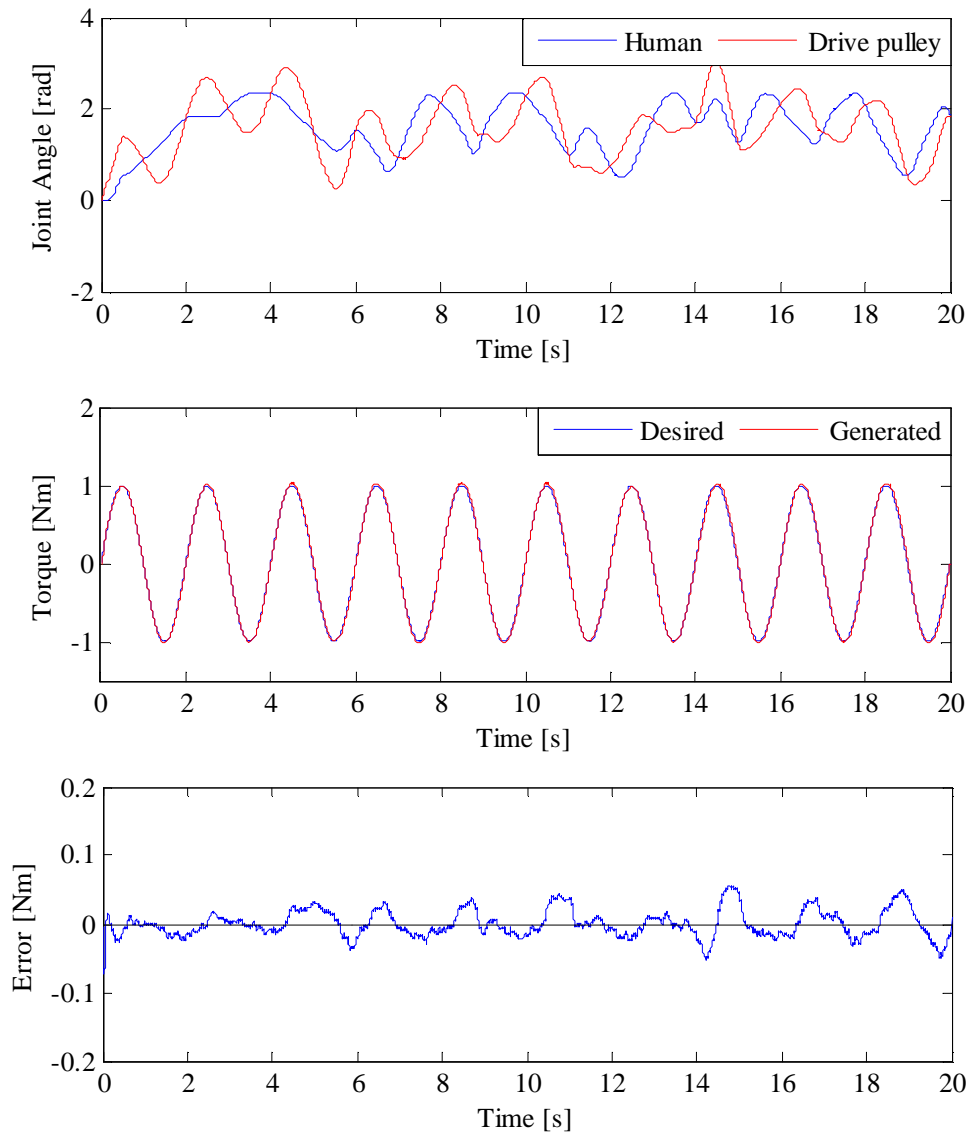


Figure 3-14: Torque tracking performance with a human user and a sinusoidal desired torque.

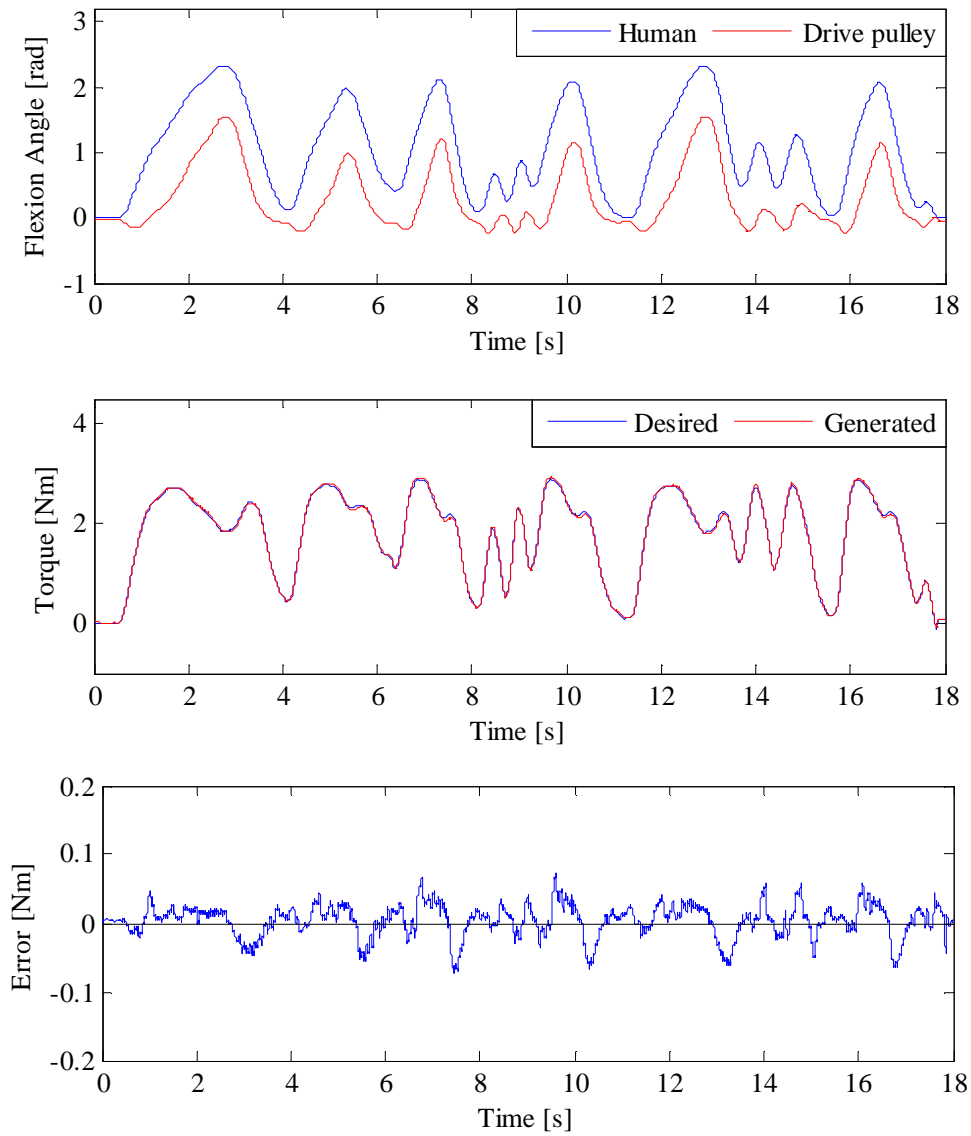


Figure 3-15: Torque tracking performance of the system in the interaction with a virtual dumbbell.

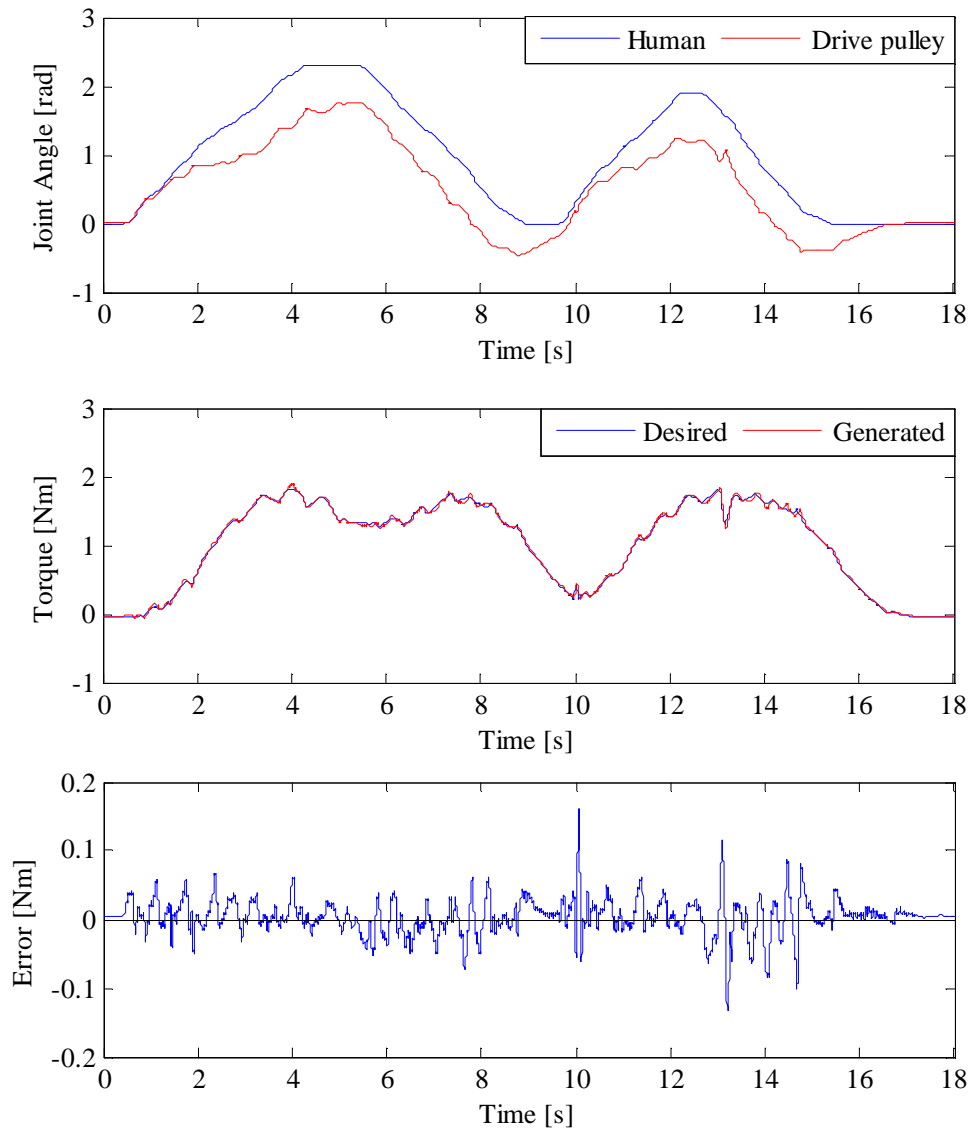


Figure 3-16: Torque tracking performance in the interaction with a robot arm.

Table 3.4: Root mean square (RMS) errors in the experiments with a user.

Experiment	RMS error (Nm)
Backdrivability	0.0133
Sinusoidal desired torque	0.0201
Interaction with a virtual dumbbell	0.0239
Interaction with a robot arm	0.0258

(Kinova, MICO [99]) was set to follow the motion of human elbow with holding a weight (0.5 Kg) using the measured elbow flexion angle from the exoskeleton. Meanwhile, the exoskeleton was set to generate the torque measured from the robot arm. The measured torque of the robot arm was scaled to 1/3 for this application. Because the robot arm and the exoskeleton were controlled by one computer, no time delay between them was occurred. In all experiments, the PD and DOB plus ZPET controllers were used to control the exoskeleton system.

The experimental results are shown in Fig. 3-13, 3-14, 3-15 and 3-16 and summarized in Table 3.4. As shown in the experimental results, the system was back-drivable and could generated the desired torque accurately, even with the unpredictable and aperiodic human motion. The experimental results imply that the proposed mechanism and control strategy are suitable for force reflection to the joints that require asymmetric torque, and confirms that the user can feel the environment in the virtual space or around the robot through the proposed system.

Although the proposed asymmetric cable-driven mechanism has relatively compact cable routing structure than conventional mechanisms, the linear spring requires certain amount of place, which could make the system bulky. Decision of the asymmetry of actuation forces also require careful considerations in the required joint force analysis, because it has different value by individual users and joints. Also, the motor side cable can be easily derailed from the idler pulley when the power is off, since it is not pulled by the motor when the motor is off. Such disadvantages make practical application of the proposed mechanism in multi-DOF systems difficult. Thus, a different type of cable-driven mechanism is developed in Chapter 3.2.

3.2 A Series Elastic Tendon-sheath Actuation Mechanism²

3.2.1 Introduction

Tendon-sheath actuation mechanisms afford more lightweight and compact tendon routing than pulley-based cable-driven mechanisms. In a tendon-sheath actuation mechanism, the tendon delivers the force by sliding through the hollow core of a flexible sheath. Thus, tendon routing does not feature a complex pulley system on the actuated structure. It has often been adopted in robotic systems such as multi-DOFs exoskeletons and manipulators, because its tendon routing is extremely simple and lightweight [29, 44, 87, 88, 100–103]. However, friction between the tendon and sheath cause many undesirable phenomena, such as hysteresis and backlash of the force, compromising precise control.

The behaviors of tendon-sheath actuation systems have been researched to overcome the disadvantages. Kaneko *et al.* developed an analytical model of friction in a single-tendon system based on the Coulomb friction model [31]. Palli *et al.* developed a LuGre-like friction model and a compensation algorithm for control of output force [32]. Both studies were limited in a single-tendon-sheath actuator, which is not enough to drive a one-DOF joint. Agrawal *et al.* developed an analytical model of a double-tendon-sheath actuation system using partial differential equations that require information on the external environment; such model is difficult to implement in real-time control systems [33]. Wu *et al.* developed an analytical model and compensation algorithms for force and position transmission by a double-tendon-sheath actuation system applicable to real-time control systems [34]. A feedforward friction compensation algorithm was developed and verified via simulation and experiment.

All of the cited studies assumed that the sheath configuration remained constant during actuation, which is not the case in multi-DOFs systems; the sheath configuration changes as the position and orientation of the distal joint changes. Such changes create uncertainties in friction models, compromising accurate control. Torque sensing elements (such as torque sensors and series elastic elements) can be placed on the output side for the feedback torque control, but they increase the weight of the actuated structure, require fast data acquisition rates and add to costs [29, 44, 100–102]. Do *et al.* modeled friction using a modified Bouc-Wen model, and developed an adaptive algorithm with position feedback to allow precise position control under varied sheath configurations, but

²Preliminary research results of this chapter were published in [6, 7]. Reprinted with permission from IEEE.

frictional torque was not compensated [104, 105].

Sheath configuration changes affect not only the friction models but also to the pretension. A pretension is a pre-loaded tensile force that prevents tendon derailment. As sheath configuration changes, the pretension is affected by changes in the lengths of the tendon paths caused by inconsistencies between the neutral axes of the sheaths and tendons. Such pretension changes can cause tendon derailment or the sheath deformation, which can severely damage the system. However, the aforementioned studies assumed that pretension was maintained within an appropriate range. This assumption is not reasonable for multi-DOFs double-tendon-sheath actuation systems, because sheath configurations vary in such systems. Changes in both friction parameters and the pretension, caused by changes in sheath configuration, must be considered in the design and control of multi-DOFs tendon-sheath actuation systems.

In Chapter 3.2, a series elastic tendon-sheath actuation mechanism for multi-DOFs systems is developed affording feedforward distal joint torque control and low pretension change during actuation. In the proposed actuation system, series elastic elements are placed on the motor side to reduce the pretension change and to control the input torque precisely. An analytic friction model of the series elastic tendon-sheath system is developed, and used to feedforwardly control the torque of the distal joint. To estimate the friction parameter, the sheaths are tightly routed through the intermediate joints via sheath holders, rendering the sheath configurations dependent on the intermediate joint angles. The performance of the proposed system was verified in experiments with a prototype manipulator. An interface for control of a tele-operation system is developed with the proposed mechanism. The force delivery performance of the interface was experimentally evaluated.

3.2.2 Characteristics of a Conventional Tendon-sheath Actuation Mechanism

In this chapter, the characteristics of a conventional double-tendon-sheath actuation mechanism are described, with a focus on torque delivery and changes in pretension. A simulation is performed based on the analysis result.

3.2.2.1 Analysis

In this analysis, Coulomb friction model was assumed among the friction models because of its simplicity and low computational burden in the real-time implementation [106]. The schematic of a conventional double-tendon-sheath actuation system composed of tendons a and b is shown in

Fig. 4-1. The tendons are routed through the hollow cores of sheaths to connect the motor- and distal-side pulleys. The length of a tendon path in the sheath is denoted by $l(t)$. As the tendon path is changed by several factors such as the tensioner and configuration changes of the sheath, $l(t)$ is assumed to be a time-variable length. A small element of tendon a is also shown in Fig. 4-1. In the figure, $f(s, \dot{\xi}, t)$ is the friction applied to the small element, caused by the normal force $dN(s, t)$. The friction can be calculated as follows:

$$f(s, \dot{\xi}, t) = \mu dN(s, t) \text{sign}(\dot{\xi}) \quad (3.24)$$

where μ is the friction coefficient and $\text{sign}()$ is the signum function. $\dot{\xi}$ can be replaced by $\omega_J(t)$ assuming that the moving direction of the tendon is determined by the rotational direction of joint. Using the force equilibrium of the small element in x and y directions, two equations are obtained as follows:

$$dT(s, t) = \mu \sigma dN(s, t) \quad (3.25)$$

$$T(s, t) d\Theta(s, t) = dN(s, t) \quad (3.26)$$

where $\sigma = \text{sign}(\omega_J(t))$, and $T(s, t)$ is the tendon tension. Combining (3.25) and (3.26) yields:

$$\frac{dT(s, t)}{T(s, t)} = \mu \sigma d\Theta(s, t) \quad (3.27)$$

By integrating both sides of (3.27) from $s = 0$ to an arbitrary point $s = s$, the force transmission equation of tendon a from $s = 0$ to $s = s$ is obtained as follows:

$$\frac{T(s, t)}{T_1(t)} = e^{\sigma \mu \int_{s=0}^{s=s} \kappa(s, t) ds}, \quad \omega_J(t) \neq 0 \quad (3.28)$$

Next, the force transmission equation from $s = 0$ to $s = l(t)$ can be derived as follows:

$$\frac{T_2(t)}{T_1(t)} = e^{\sigma \mu \Theta(t)}, \quad \omega_J(t) \neq 0 \quad (3.29)$$

where the bending angle of the entire tendon path, $\Theta(t)$, is defined as follows:

$$\Theta(t) = \int_{s=0}^{s=l(t)} d\Theta(s, t) = \int_{s=0}^{s=l(t)} \kappa(s, t) ds \quad (3.30)$$

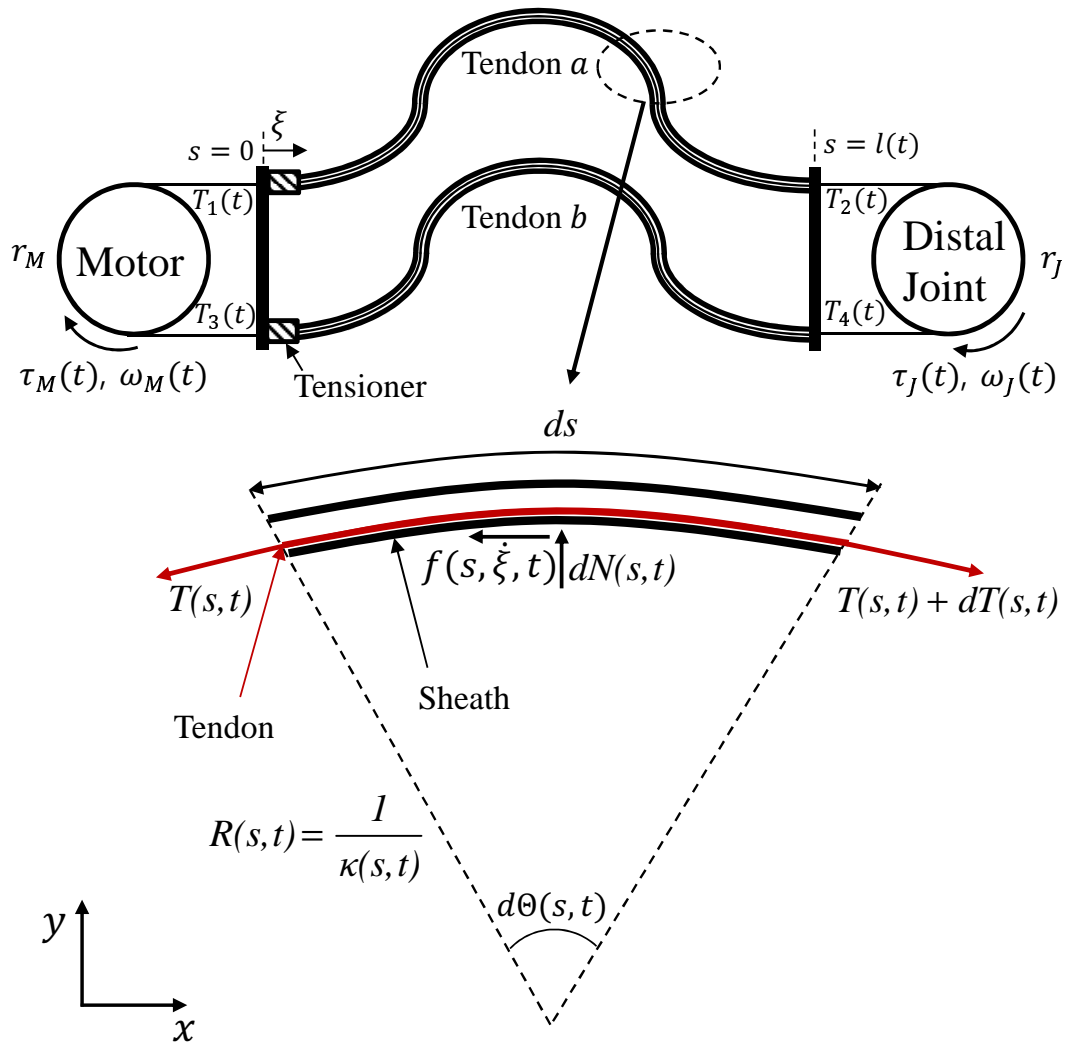


Figure 3-17: Configuration of a conventional double-tendon-sheath actuation mechanism and its small element. [r_M , $\omega_M(t)$ and $\tau_M(t)$ are the radius, angular velocity, and torque of the motor-side pulley, and r_J , $\omega_J(t)$ and $\tau_J(t)$ are the values of the same parameters for the distal joint. s , ξ , and t represent the position on the tendon path, the relative displacement of the tendon for the sheath, and time, respectively. $R(s, t)$, $\kappa(s, t)$ and $d\theta(s, t)$ are the radius, curvature, and central angle of the small element of the tendon-sheath system. T represents tendon tension].

(3.29) describes force delivery by a single-tendon-sheath actuation system featuring several parameters. Of these, $\mu\Theta(t)$ is difficult to measure directly using a sensor, because $\Theta(t)$ depends on the sheath configuration. Note that the equation is only available when the system is moving. In static state, the output force varies by the output side environment. In this case, the input force is not transmitted to the output side until the difference between input and output forces overcomes the friction. Since the aim of this research is the feedforward control of output torque, which is available in moving state, further analysis is carried out with a focus on the state in which $\omega_J \neq 0$.

The tendon is elongated when tension is applied. The elongation of tendon can be analyzed by assuming the tendon is elastic. The elongation of a small tendon element can be derived as follows:

$$d\delta(s, t) = \frac{T(s, t)}{EA} dl_{us}(s, t) \quad (3.31)$$

where $\delta(s, t)$ is the tendon elongation, E and A are the elastic modulus and the cross-sectional area of the tendon, respectively. $dl_{us}(s, t)$ represents the unstrained length of the small tendon element. $dl_{us}(s, t)$ is always less than or equal to ds , because only pulling forces can be applied to the tendon. $dl_{us}(s, t)$ can be expressed by $d\delta(s, t)$ and ds as follows:

$$dl_{us}(s, t) = ds - d\delta(s, t) \quad (3.32)$$

Integration of $dl_{us}(s, t)$ from $s = 0$ to $s = s$ follows:

$$l_{us}(s, t) = \int_{s=0}^{s=s} dl_{us}(s, t) \quad (3.33)$$

where $l_{us}(s, t)$ at $s = l(t)$ is l_{us} (a constant). In terms of the elongation of tendon a , a combination of (3.28) and (3.31) yields:

$$d\delta_a(s, t) = \frac{T_1(t)}{EA} e^{\mu\sigma \int_{s=0}^{s=s} \kappa(s, t) ds} dl_{us}(s, t) \quad (3.34)$$

By integrating (3.34) along the tendon path [i.e., from $s = 0$ to $s = l(t)$], the elongation of tendon a can be calculated as follows:

$$\delta_a(t) = \frac{T_1(t)}{EA} \alpha(t) \quad (3.35)$$

where $\alpha(t)$ is defined as:

$$\alpha(t) = \int_{l_{us}(s,t)=0}^{l_{us}(s,t)=l_{us}} e^{\mu\sigma \int_{s=0}^{s=s} \kappa(s,t)ds} dl_{us}(s,t) \quad (3.36)$$

It is difficult to simplify (3.35) further, because $\int_{s=0}^{s=s} \kappa(s,t)ds$ depends on the configuration of sheath, which cannot be expressed using a specific function. Wu *et al* simplified (3.35) by assuming that the sheath curvature was constant along the entire sheath, but this is valid in only a few circumstances [34]. In (3.35), $\alpha(t)$ represents the degree of difference between the tendon elongation under zero friction and actual friction. If μ or $\kappa(s,t)$ is zero, $\alpha(t)$ becomes equal to the unstrained tendon length l_{us} , and $\delta_a(t)$ is the elongation of tendon a under zero friction. An increase in μ or $\kappa(s,t)$ increases the difference between $\delta_a(t)$ and the elongation under zero friction.

The analysis of a single-tendon-sheath system can be extended to a double-tendon-sheath actuation system. Assuming that the two sheaths have same configurations, the force delivery equation for tendon b is as follows:

$$\frac{T_4(t)}{T_3(t)} = e^{-\sigma\mu\Theta(t)} \quad (3.37)$$

, and the elongation of tendon b is:

$$\delta_b(t) = \frac{T_3(t)}{EA} \beta(t) \quad (3.38)$$

where $\beta(t)$ is:

$$\beta(t) = \int_{l_{us}(s,t)=0}^{l_{us}(s,t)=l_{us}} e^{-\mu\sigma \int_{s=0}^{s=s} \kappa(s,t)ds} dl_{us}(s,t) \quad (3.39)$$

(3.35), (3.38) and the geometry of the system imply that a tendon can be slacked from the pulleys during the actuation of the double-tendon-sheath actuation system, because one tendon is loosened at the time that the other is tensioned. To prevent this slack, both tendons must be tensioned prior to system actuation. In this research, the pretension is defined as the average tendon tensile forces of the motor side, as follows:

$$T_p(t) = (T_1(t) + T_3(t))/2 \quad (3.40)$$

Since the two sheaths are assumed to have identical configurations, the lengths of tendon paths are also identical. Considering the geometry of the system, the relationship between the tendon elongations and the length changes of these tendon paths can be obtained as follows:

$$\delta_a(t) + \delta_b(t) = 2\Delta l(t) \quad (3.41)$$

where the length change of a tendon path by reference to the unstrained tendon length is defined as:

$$\Delta l(t) = l(t) - l_{us} \quad (3.42)$$

If sheath configurations are constant, the tendon path lengths retain their initial values. In such cases, $\Delta l_t(t)$ can be assumed to be constant, as follows:

$$\Delta l(t) = \Delta l(0) \quad (3.43)$$

where $\Delta l(0)$ is the initial value of $\Delta l(t)$. Then, (3.41) can be reformulated as:

$$\delta_a(t) + \delta_b(t) = 2\Delta l(0) \quad (3.44)$$

The torque on the motor and distal joint sides are:

$$\tau_M(t) = r_M(T_3(t) - T_1(t)) \quad (3.45)$$

$$\tau_J(t) = r_J(T_4(t) - T_2(t)) \quad (3.46)$$

Combining (3.29), (3.35)-(3.39) and (3.42)-(3.46) yields the relationship between $\tau_M(t)$ and $\tau_J(t)$:

$$\tau_J(t) = \frac{r_J}{\alpha(t) + \beta(t)} \left(\frac{\tau_M(t)}{r_M} (\alpha(t)e^{-\sigma\mu\Theta(t)} + \beta(t)e^{\sigma\mu\Theta(t)}) - 4EA \sinh(\sigma\mu\Theta(t)) \Delta l(0) \right) \quad (3.47)$$

The pretension can be reformulated as a function of $\tau_M(t)$ by combining (3.35), (3.38), (3.40), (3.44) and (3.45), as follows:

$$T_p(t) = \frac{2EA}{\alpha(t) + \beta(t)} \Delta l(0) + \frac{(\alpha(t) - \beta(t)) \tau_M(t)}{(\alpha(t) + \beta(t)) 2r_M} \quad (3.48)$$

Unknown parameters in (3.47), including μ , $\Theta(t)$, $\alpha(t)$ and $\beta(t)$, can be identified if the sheath configuration does not change as assumed; these parameters depend on sheath curvature. However, the sheath curvature changes in multi-DOFs systems because of changes in distal joint position and orientation, varying the model parameters. The changes introduce uncertainties into the friction model. Therefore, applications of the feedforward distal-side torque control are confined to systems featuring constant sheath configurations.

A sheath configuration change also triggers a pretension change. If a tendon path coincident to

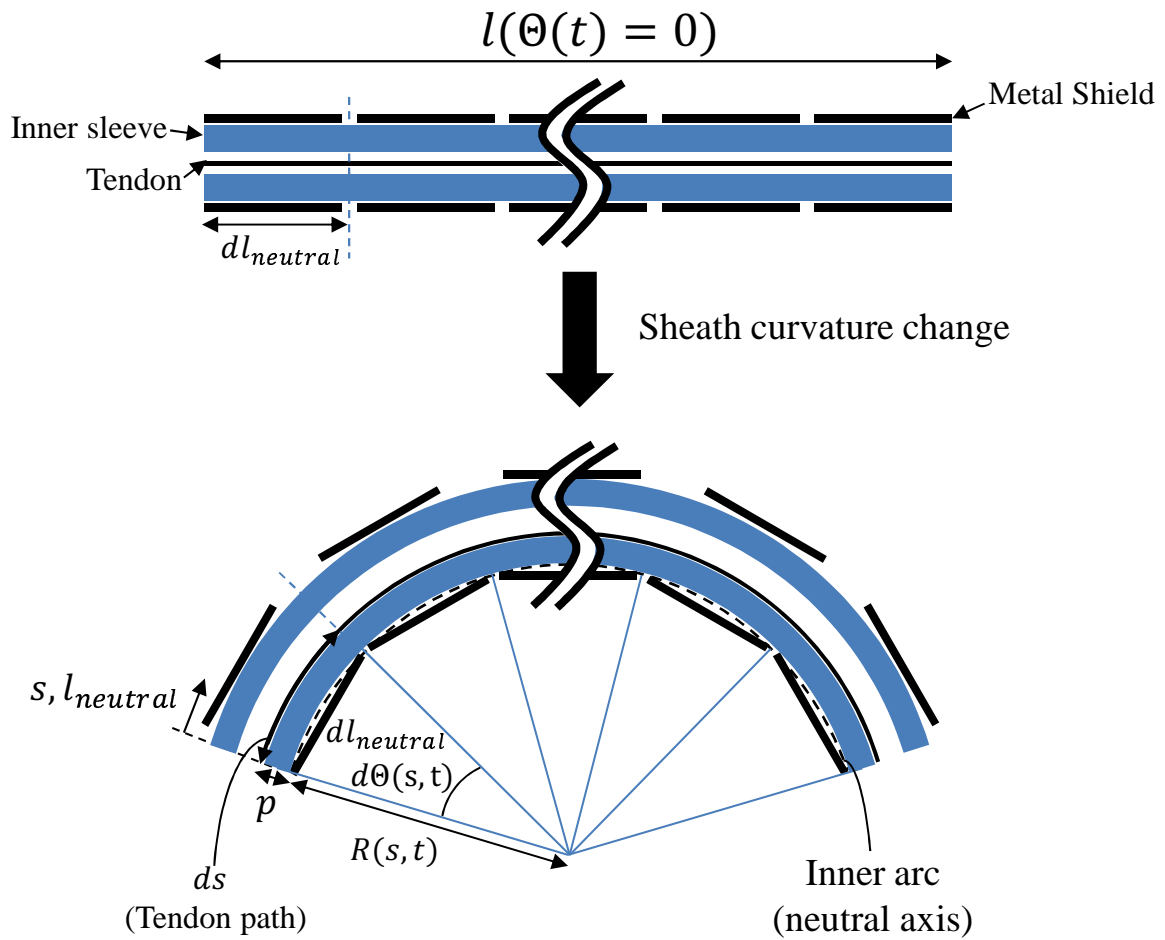


Figure 3-18: A longitudinal cross section of spiral type sheath. (s and $l_{neutral}$ are the positions on the tendon path and neutral axis, respectively. $l(\Theta(t) = 0)$ is the flat sheath length; $dl_{neutral}$, ds , $R(s, t)$ and $d\Theta(s, t)$ are the longitudinal coil with, the tendon path, and the radius and bending angle of a small sheath element, respectively. p is the distance from the tendon-inner sleeve contact line to the inner arc of the sheath.)

the neutral axis of a sheath, the tendon path length ($l(t)$) is preserved when the bending of sheath. However, the tendon path does not lie on the neutral axis in most systems. Thus, the tendon path length changes as the sheath configuration varies. When exploring such length changes, the sheath structure must be considered. A sheath is composed of an inner sleeve and a metal shield. The inner sleeve, usually made of a low-friction material such as polytetrafluoroethylene (PTFE), contacts the tendon within its hollow core. The metal shield wraps the inner sleeve and withstands the tendon-imparted compressive so that the sheath configuration is maintained under such load. Any change in the length of tendon path depends on the type of sheath employed. Spiral type sheath is popular in robotic applications; the metal shield is a helical coil (Fig. 3-18). Since the metal shield has low bending stiffness but have high compressive and extensional stiffness, the neutral axis of the sheath lies on the inner arc of the metal shield, shown as a dashed line in Fig. 3-18. In this analysis, the longitudinal width of the spiral metal shield is assumed to be $dl_{neutral}$, and the pitch also takes this value. The sheath length is assumed to $l(\Theta(t) = 0)$ when the sheath is not bent. If the sheath is bent, the system can be divided into small elements featuring small arcs, with inner-arc radii of $R(s, t)$ and corresponding bending angles $d\Theta(s, t)$. The tendon path then lies on the outer side of the neutral axis, and the length of the small element can be calculated as follows:

$$ds = (R(s, t) + p + \frac{d}{2})d\Theta(s, t) \quad (3.49)$$

where p is the distance from the tendon-inner sleeve contact line to the inner arc of the sheath, and d is the diameter of the tendon. Assuming that $d\Theta(s, t)$ is very small, $R(s, t)d\Theta(s, t)$ can be approximated by $dl_{neutral}$. Then, the length of the entire tendon path can be derived by integrating (3.49) as follows:

$$l(t) = \int_{l_{neutral}=0}^{l_{neutral}=l(\Theta(t)=0)} ds = l(\Theta(t) = 0) + (p + \frac{d}{2})\Theta(t) \quad (3.50)$$

which means that the tendon path length is affected by the change in $\Theta(t)$, defined as follows:

$$\Delta\Theta(t) = \Theta(t) - \Theta_{us} \quad (3.51)$$

where Θ_{us} is the bending angle of the sheath that renders the tendon unstrained. Then, the length

change of a tendon path within a sheath from unstrained state to a state in time t is:

$$\Delta l(t) = \left(p + \frac{d}{2}\right) \Delta \Theta(t) \quad (3.52)$$

Modeling errors may affect the accuracy of (3.52), and the equation differs by the type of sheath used. The important point is that the length of tendon path changes as the configuration of sheath changes, because the neutral axis of tendon and the sheath are difficult to be coincident. Thus, (3.44) is not available when sheath configuration varies, but (3.41) is available under such circumstances. Thus, (3.47) and (3.48) can be reformulated as follows:

$$\tau_J(t) = \frac{r_J}{\alpha(t) + \beta(t)} \left(\frac{\tau_M(t)}{r_M} (\alpha(t)e^{-\sigma\mu\Theta(t)} + \beta(t)e^{\sigma\mu\Theta(t)}) - 4EA \sinh(\sigma\mu\Theta(t)) \Delta l(t) \right) \quad (3.53)$$

$$T_p(t) = \frac{2EA}{\alpha(t) + \beta(t)} \Delta l(t) + \frac{(\alpha(t) - \beta(t)) \tau_M(t)}{(\alpha(t) + \beta(t)) 2r_M} \quad (3.54)$$

It is difficult to understand (3.53) and (3.54) intuitively because the equations contain complex terms related to $\alpha(t)$ and $\beta(t)$. Both (3.53) and (3.54) can be simplified by modifying $\alpha(t)$ and $\beta(t)$ terms. First, assume $\sigma = 1$ and an arbitrary sheath curvature $\kappa(s, t)$. If $\mu = 0$ or $\Theta(t) = 0$ (i.e. friction is zero), $\alpha(t)$ and $\beta(t)$ are both equal to l_{us} . As μ and $\Theta(t)$ increase, the effect of friction increases, and, thus, $\alpha(t)$ becomes greater than l_{us} and $\beta(t)$ becomes less than l_{us} . At a given $\Theta(t)$, the maximum of $\alpha(t)$ and the minimum of $\beta(t)$ appear when the curvature is concentrated at $s = 0$ [i.e. $\kappa(s = 0, t) = \infty$ and $\kappa(s > 0, t) = 0$], because all tendon elements except those at $s = 0$ are elongated by $T_2(t)$ or $T_4(t)$, which includes all friction forces acting on each tendon. Thus, this condition maximize the difference between $\alpha(t)$ and $\beta(t)$ at a given $\Theta(t)$. When $\sigma = -1$ (i.e. the direction of the friction is now opposite to that considered above), friction inversely affect $\alpha(t)$ and $\beta(t)$, but the difference between these values is also the same maximum noted above.

Fig. 3-19 shows a simulation performed with the extreme condition. In this simulation, the sums of $\alpha(t)$ and $\beta(t)$ ($\alpha(t) + \beta(t)$) and the difference between $\alpha(t)$ and $\beta(t)$ ($|\alpha(t) - \beta(t)|$) are simulated at varying $\Theta(t)$ and μ . $\Theta(t)$ is varied from 0 to $\pi/2$ considering the application of tendon-sheath actuation mechanism, and μ is varied from 0.01 to 0.05 in steps of 0.01 by reference to the friction between steel and lubricated low-friction polymers [107]. Both $\alpha(t) + \beta(t)$ and $|\alpha(t) - \beta(t)|$ are calculated in the unit of l_{us} . $\alpha(t) + \beta(t)$ is very closed to $2l_{us}$; this, which is the value when the friction is zero, because the tendons are tensioned or loosened antagonistically. Also, $|\alpha(t) - \beta(t)|$ is very small, indicating that $\alpha(t)$ and $\beta(t)$ have similar values. In real applications, $|\alpha(t) - \beta(t)|$ is

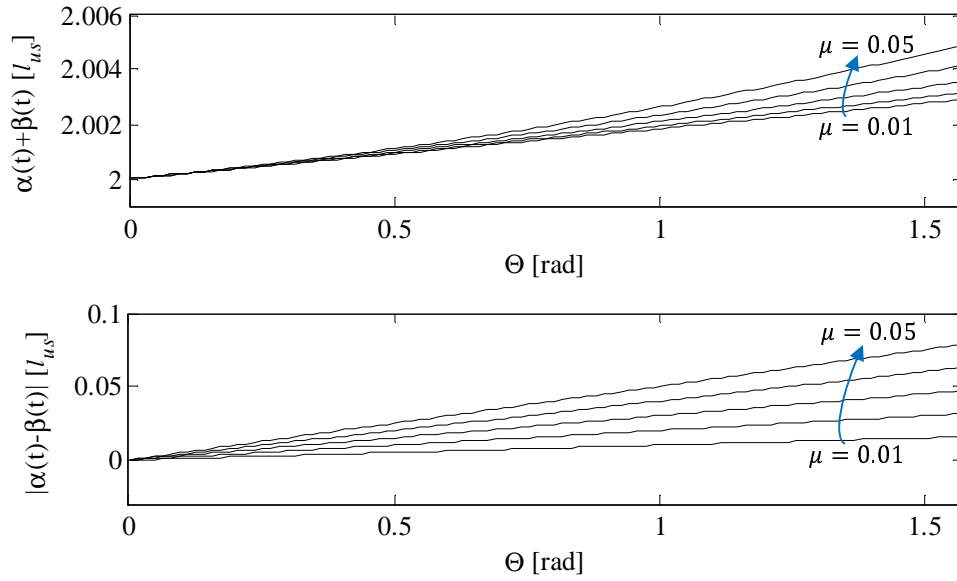
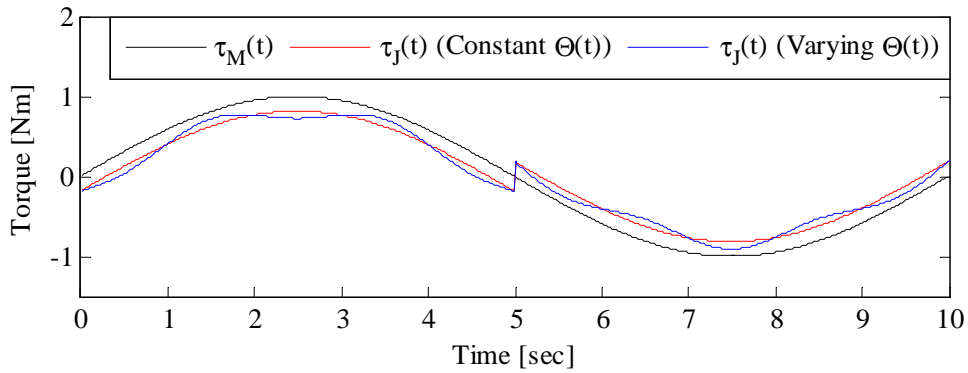
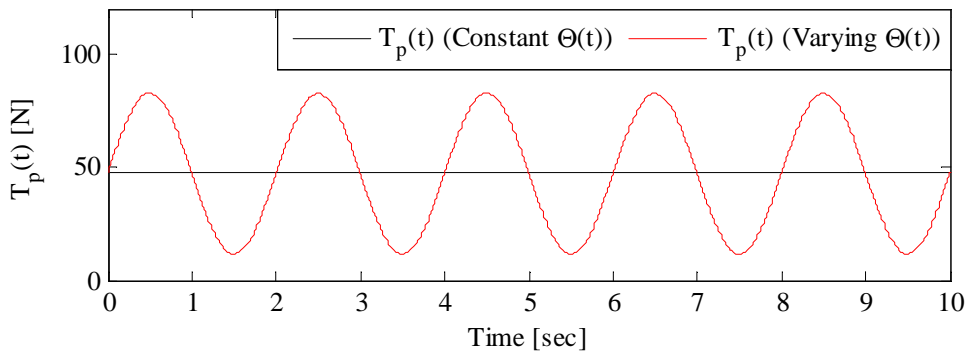


Figure 3-19: Variations in $\alpha(t) + \beta(t)$ and $|\alpha(t) - \beta(t)|$ with changes in $\Theta(t)$ and μ .



(a) Motor-side and distal joint-side torque



(b) Pretension

Figure 3-20: Simulation results of a double-tendon-sheath actuation system.

smaller than the simulation result, because the curvature cannot be concentrated to a point. Thus, it is reasonable to assume $\alpha(t)$ and $\beta(t)$ are both closed to u_s . Applying this assumption and allowing small modeling errors, (3.53) and (3.54) can be simplified as follows:

$$\tau_J(t) = r_J \left(\frac{\tau_M(t)}{r_M} \cosh(\sigma \mu \Theta(t)) - 2T_p(t) \sinh(\sigma \mu \Theta(t)) \right) \quad (3.55)$$

$$T_p(t) = \frac{EA}{l_{us}} \Delta l(t) \quad (3.56)$$

The simplified equations imply that the pretension change depends on the length change of tendon path, which in turn varies with changes in sheath configuration. The pretension change may lie outside the appropriate range, because EA is much larger than l_{us} in most tendon-sheath actuation systems. As the distal joint torque contains a pretension-related term, the pretension change also affect to the torque transmission, as $\mu\Theta(t)$ does in (3.55).

3.2.2.2 Simulation

A simulation is performed using (3.55) and (3.56) for a conventional double-tendon-sheath actuation system. The motor-side torque is set to a sinusoidal torque with a maximum amplitude of 1 Nm and a frequency of 0.1 Hz. The tendons are assumed to be steel cables with $d = 0.8$ mm, $E = 200$ GPa, and $l_{us} = 1$ m; the radii of the motor- and distal-side pullies are set to 50 mm. The sheath is assumed to be of the spiral type and cylindrical in configuration. Θ_{us} is set to 0, and $\Theta(t)$ is either maintained at the initial value ($\pi/4$) or changed sinusoidally with a maximum amplitude of $\pi/6$ and a frequency of 0.5 Hz. μ is set to 0.05, assuming that the inner liner of the sheath is a low-friction material such as PTFE. The distance from neutral axis to the tendon-sheath contact line (p) was set to 0.5 mm. σ is assumed to be 1 and -1 before and after $t = 5$ sec, respectively.

The simulation results are shown in Fig. 3-20. Figure 3-20a shows the motor-side and distal joint-side torques during simulation. It is apparent that $\tau_J(t)$ assumes values distinct from those of $\tau_M(t)$, because of friction. When the sheath configuration is constant, the shape of $\tau_J(t)$ is similar to that of $\tau_M(t)$, because all parameters of (3.55) are constant, given that the sheath configuration-related value [i.e. $\Theta(t)$] is constant. On the other hand, when the sheath configuration varies, $\tau_J(t)$ behaves quite unlike $\tau_M(t)$, because of the changes in $\Theta(t)$ and $T_p(t)$. In both cases, the direction of frictional torque changes as σ changes at $t = 5$ sec. The pretension also differs by sheath configuration, as shown in Fig. 3-20b. $T_p(t)$ remains constant when $\Theta(t)$ is constant, but changes

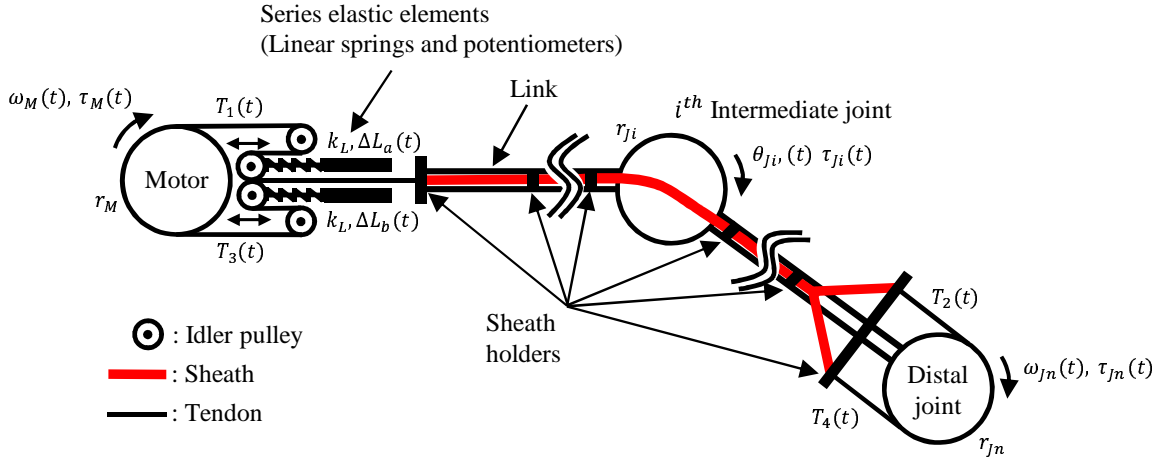


Figure 3-21: Configuration of the proposed mechanism for n -DOFs systems. r_M , $\omega_M(t)$ and $\tau_M(t)$ are the radius, angular velocity, and torque of the motor-side pulley, r_{J_i} , $\omega_{J_i}(t)$ and $\tau_{J_i}(t)$ are the values of those parameters for the i^{th} intermediate joint. $\Delta L_a(t)$, $\Delta L_b(t)$ and k_L are the displacements and the spring constant of linear springs, and $T_i(t)$ is the tendon tension.

significantly as $\Theta(t)$ varies.

The simulation implies that friction depends on the sheath configuration-related parameter $\Theta(t)$, which is difficult to measure directly. Also, a change in tendon paths during operation, induced by a sheath configuration change, can cause the pretension to vary significantly, because the spring constant of a tendon (EA/l_{us}) is very high. The studies reviewed in Chapter 3.2.1 assumed that the pretension was maintained within an appropriate range. However, this is not the case in many applications of tendon-sheath actuation mechanisms; the sheath configurations change when intermediate joints are actuated. A low pretension can cause slack of the system, triggering tendon derailment from pulleys. A large pretension enables large torque transmission without any slack, but also increase friction, negatively affecting the torque bandwidth and power transmission efficiency. Moreover, the sheath or tendon may wear or become deformed if the pretension is large. Changes in friction parameter and large changes in pretension, caused by the sheath configuration changes, compromise accurate output torque control and cause safety problems.

3.2.3 Design and Control of a Series Elastic Tendon-sheath Actuation Mechanism

To overcome the two issues (changes in the friction parameter and the pretension) induced by sheath configuration changes, we designed a series elastic tendon-sheath actuation mechanism (Fig. 3-21). The mechanism was designed for n -DOFs systems in which the distal joint position and orientation are varied by actuation of intermediate joints. To reduce pretension changes, a compressive linear

spring is attached to each idler pulley of all tendons on the motor side, where the tendons are routed. The degree of pretension change can be adjusted by selection of appropriate linear springs of spring constants k_L . The length of each spring is measured using a potentiometer; tendon tension is derived by calculating the compressive spring force. Pretension is measurable in realtime using the series elastic element, and the initial pretension is adjustable by changing its position. Accurate input torque control and safety in interactions with human users are achieved by these series elastic elements.

The tendons are routed through the sheaths from the motor side to the distal; routing is compact. To allow estimation of friction parameters, the sheaths are routed through intermediate joints, rather than routing freely from the motor side to the distal side as in most conventional tendon-sheath actuation mechanisms. The sheath configuration can be assumed to be dependent on the intermediate joint angles, because the sheaths are tightly attached to the links via the sheath holders.

The torque delivery equation can be derived by analyzing the system as described in Chapter 3.2.2. As the system features two tendons and sheaths, as does the conventional system analyzed in Chapter 3.2.2, (3.24)-(3.40) and all associated assumptions and notations are available. Assuming that the spring displacements have linear relationships with the spring forces, $T_1(t)$ and $T_3(t)$ can be calculated as follows:

$$T_1(t) = -k_L \Delta L_a(t) / 2 \quad (3.57)$$

$$T_3(t) = -k_L \Delta L_b(t) / 2 \quad (3.58)$$

where $\Delta L_a(t)$ and $\Delta L_b(t)$ are the displacement of the linear springs from their natural lengths. Given the geometry of the system, the relation between the tendon elongations, length change of tendon paths and the linear spring displacements, can be derived as follows:

$$\delta_a + \delta_b = 2\Delta l(t) + 2(\Delta L_a(t) + \Delta L_b(t)) \quad (3.59)$$

Combining (3.59) with (3.35), (3.38), (3.57) and (3.58) yields:

$$T_1(t) \left(\frac{\alpha(t)}{EA} + \frac{4}{k_L} \right) + T_3(t) \left(\frac{\beta(t)}{EA} + \frac{4}{k_L} \right) = 2\Delta l(t) \quad (3.60)$$

The motor- and distal-joint-side torques can be calculated as follows:

$$\tau_M(t) = r_M(T_3(t) - T_1(t)) \quad (3.61)$$

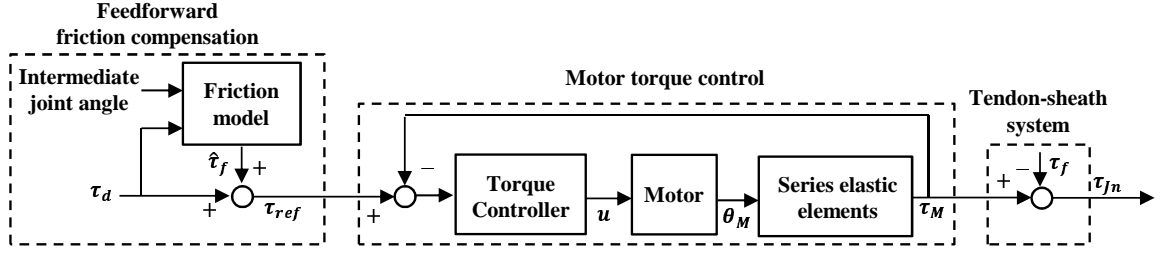


Figure 3-22: Block diagram of the control structure.

$$\begin{aligned}\tau_{Jn}(t) &= r_J(T_4(t) - T_2(t)) \\ &= r_J(T_3(t)e^{-\sigma\mu\Theta(t)} - T_1(t)e^{\sigma\mu\Theta(t)})\end{aligned}\quad (3.62)$$

$T_1(t)$ and $T_3(t)$ in (3.60) can be removed by modifying (3.61) and (3.62) in terms of $T_1(t)$ and $T_3(t)$ and inserting them into (3.60). Simplifying $\alpha(t)$ and $\beta(t)$ as in Chapter 3.2.2, the torque delivery equation from the motor- to the distal-joint-side can be derived as follows:

$$\tau_{Jn}(t) = \frac{r_{Jn}}{r_M}\tau_M(t)\cosh(\sigma\mu\Theta(t)) - \frac{2r_{Jn}EA\sinh(\sigma\mu\Theta(t))}{l_{us} + 4EA/k_L}\Delta l(t)\quad (3.63)$$

As EA is much larger than l_{us} in most tendon-sheath actuation systems, (3.63) can be simplified further as follows:

$$\tau_{Jn}(t) = \frac{r_{Jn}}{r_M}\tau_M(t)\cosh(\sigma\mu\Theta(t)) - r_{Jn}\sinh(\sigma\mu\Theta(t))\Delta l(t)k_L/2\quad (3.64)$$

Similarly, the pretension can be calculated by combining (3.40), (3.35), (3.38), (3.57), (3.58), (3.61) and (3.59) as follows:

$$T_p(t) = k_L\Delta l(t)/4\quad (3.65)$$

(3.64) can be expressed as a function of $T_p(t)$ by inserting (3.65) into (3.64) as follows:

$$\tau_{Jn}(t) = \frac{r_{Jn}}{r_M}\tau_M(t)\cosh(\sigma\mu\Theta(t)) - 2r_{Jn}T_p(t)\sinh(\sigma\mu\Theta(t))\quad (3.66)$$

(3.65) implies that the pretension change depends on the change in length of the tendon path, as in a conventional double-tendon-sheath actuation system, but the extent of change is determined by k_L rather than the physical properties of tendon as shown in (3.56). Thus, the change in pretension can be significantly reduced by selecting linear springs with appropriate k_L values. The torque delivery equation of the proposed system implies that the estimation of, or compensation for, frictional torque is possible if $\mu\Theta(t)$ is identified, as $\mu\Theta(t)$ is the only unknown parameter in (3.66). As the sheath

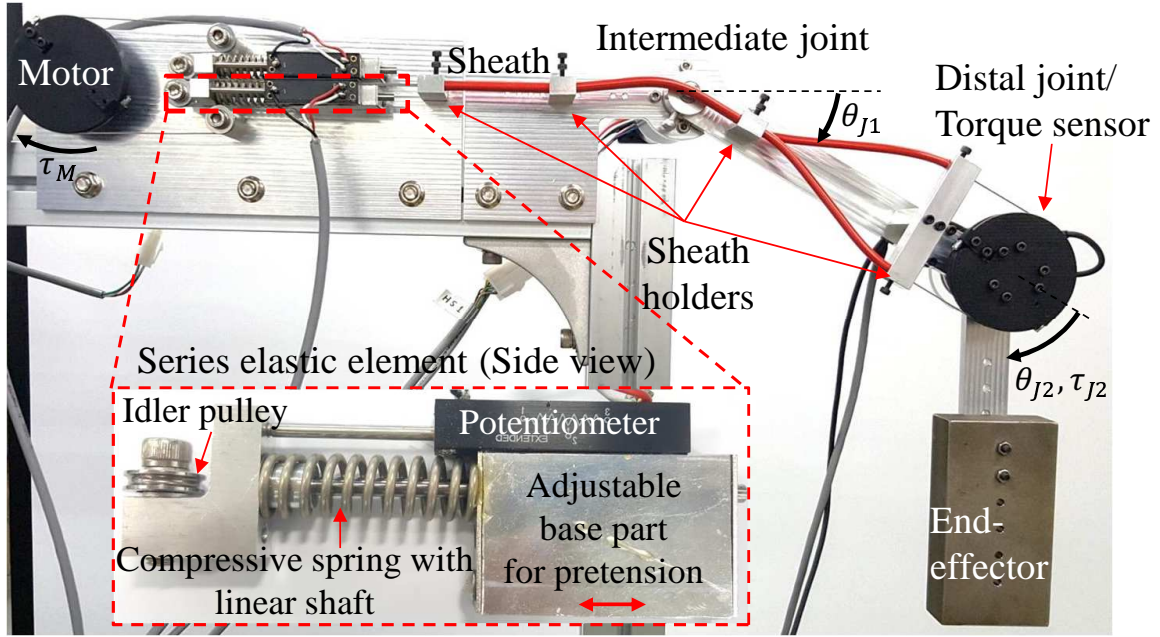


Figure 3-23: A prototype manipulator used to verify the performance of the proposed mechanism.

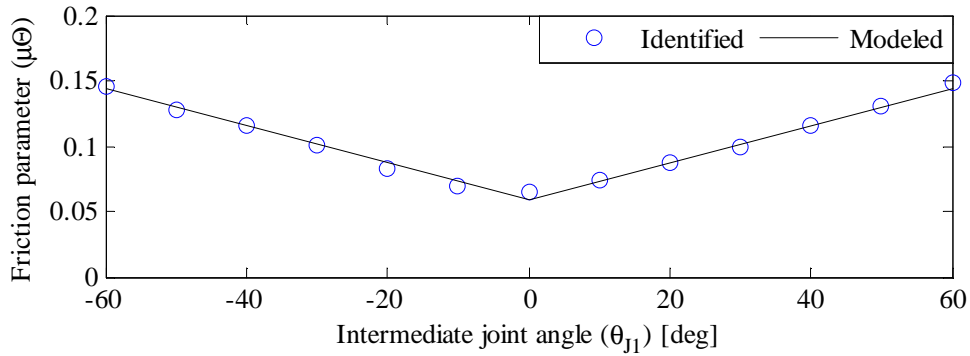


Figure 3-24: Identified and modeled friction parameter.

configuration is dependent on the intermediate joint angles, $\mu\Theta(t)$ can be experimentally identified as a function of intermediate joint angles as follows:

$$\mu\Theta(t) = f(\theta_{J1}(t), \dots, \theta_{Jn-1}(t)) \quad (3.67)$$

A feedforward torque control structure was developed as Fig. 4-2 to make the distal joint torque $\tau_{Jn}(t)$ follow the desired torque $\tau_d(t)$. Assuming the friction parameter is updated in real-time, the frictional torque $\tau_f(t)$ can be estimated as $\hat{\tau}_f(t)$ using (3.66) as follows:

$$\hat{\tau}_f(t) = \left(\frac{r_M}{r_{Jn}} \operatorname{sech}(\sigma\mu\Theta(t)) - 1 \right) \tau_d(t) + 2r_M T_p(t) \tanh(\sigma\mu\Theta(t)) \quad (3.68)$$

The estimated frictional torque is added to the desired torque to compensate for $\tau_f(t)$. The reference torque $\tau_{ref}(t)$ serves as the input of a motor torque controller. As friction is estimated and feedforwardly compensated by $\hat{\tau}_f(t)$, $\tau_{Jn}(t)$ follow $\tau_d(t)$.

3.2.4 Experimental Verifications

3.2.4.1 Verification of the Proposed Mechanism

To verify the performance of the proposed mechanism and control algorithm, a 2-DOFs manipulator was manufactured (Fig. 3-23). The overall structure was the same as that shown in Fig. 3-21, but with $n = 2$. In this system, the intermediate joint was actuated by a directly attached motor, which was later replaced with tendon-sheath actuated joints in the application. A torque sensor was placed at the distal joint to identify the friction parameter and verify the feedforward torque control. The series elastic elements were attached to the base, and were movable to allow adjustment of the initial pretension. The lengths of compressive linear springs were measured by precision potentiometers. Braided steel cables and spiral type sheaths with low-friction inner sleeves were employed for high force transmission efficiency and durability. The sheaths were routed through the tops of the linkages and the intermediate joint. As the sheaths were securely held by sheath holders on the linkages, the sheath configuration depended on the intermediate joint angle without large oscillations. The detailed specifications are listed in Table 3.5.

The friction parameter $\mu\Theta$ in (3.66) was experimentally identified and modeled as a function of the intermediate joint angle (θ_{J1}). An arbitrary torque was applied by the motor, and the motor- and distal-side torques were measured as the intermediate joint angle was varied in 10° steps. For each intermediate joint angle, the $\mu\Theta$ value that minimizing the root mean square modeling error was identified with the aid of (3.66). As shown in Fig. 3-24, the friction parameter exhibited a symmetrical linear relationship with the intermediate joint angle, and was appropriately modeled using the least squares method to allow implementation of the friction parameter in the control algorithm.

Torque transmission experiments with/without feedforward friction compensation were performed using the control structure of Fig. 4-2. An empirically tuned PD controller was applied to the motor torque controller. A user arbitrarily moved the end-effector, while τ_d delivered a sinusoidal signal of magnitude 1 Nm. The intermediate joint angle was also sinusoidally varied during actuation, at an amplitude of 50° .

Table 3.5: Specifications of the 2-DOFs system

	Specification
Motor	Maxon EC-4pole Gear ratio : 74:1 Nominal speed : 22.5 rad/s Nominal torque : 6.767 Nm
Driver	Maxon ESCON 70/10
Tendon	AISI314 stainless steel 0.8mm diameter, 7x7 braided
Sheath	Jagwire, Spiral type
Pulley diameters	$r_M = r_{J2} = 32.5$ mm
Potentiometer	ETI Systems LCP12-25
Torque sensor	FUTEK TFF500
DAQ	National Instruments PCIe-7841R and PCIe-6363
Encoder	US Digital Incremental, 2500 CPR
CPU	Intel i7-3770
Operating System	Microsoft Windows 7
Softwares	National Instruments LabVIEW 2015

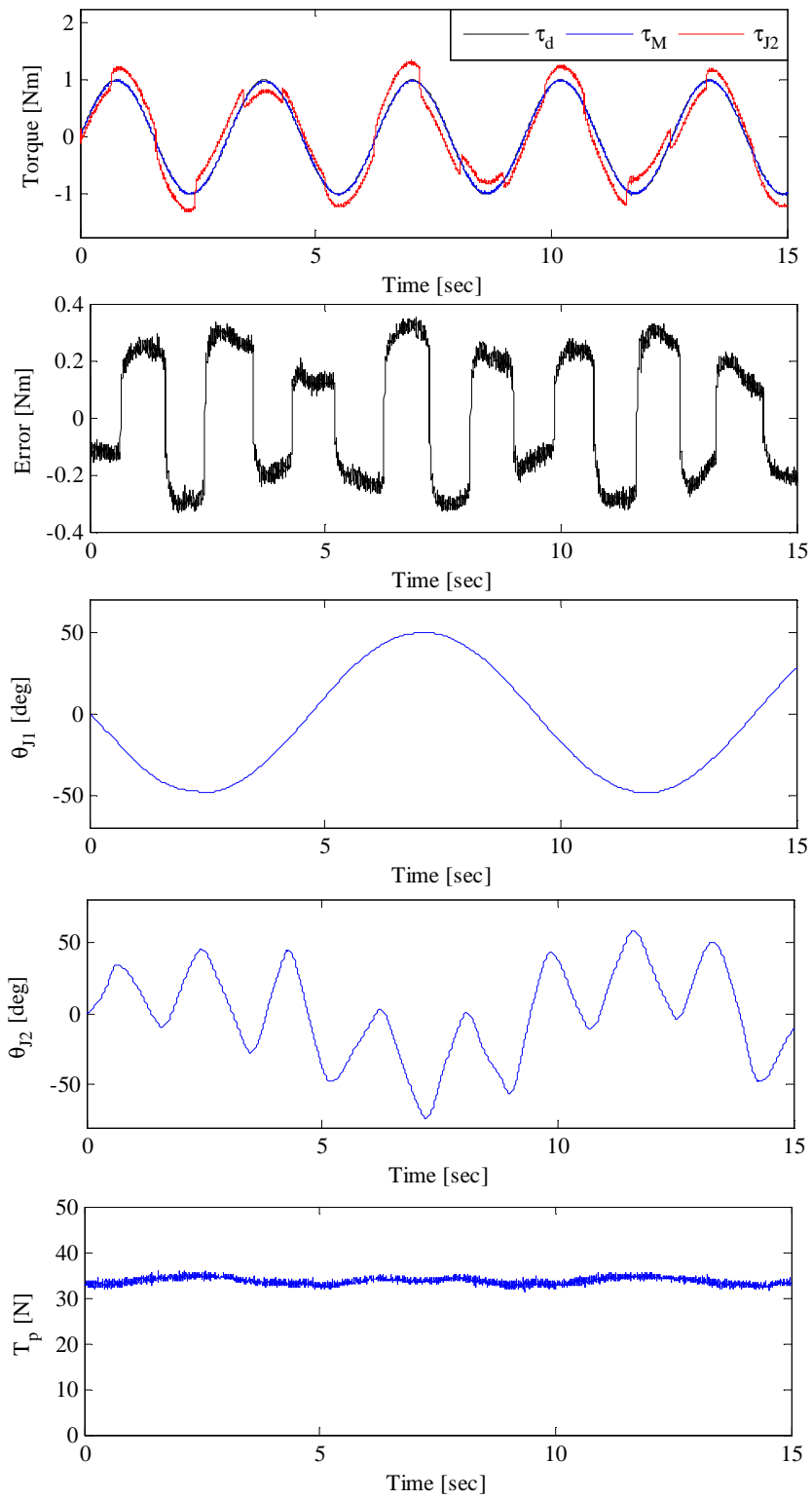


Figure 3-25: Experimental result in the absence of friction compensation.

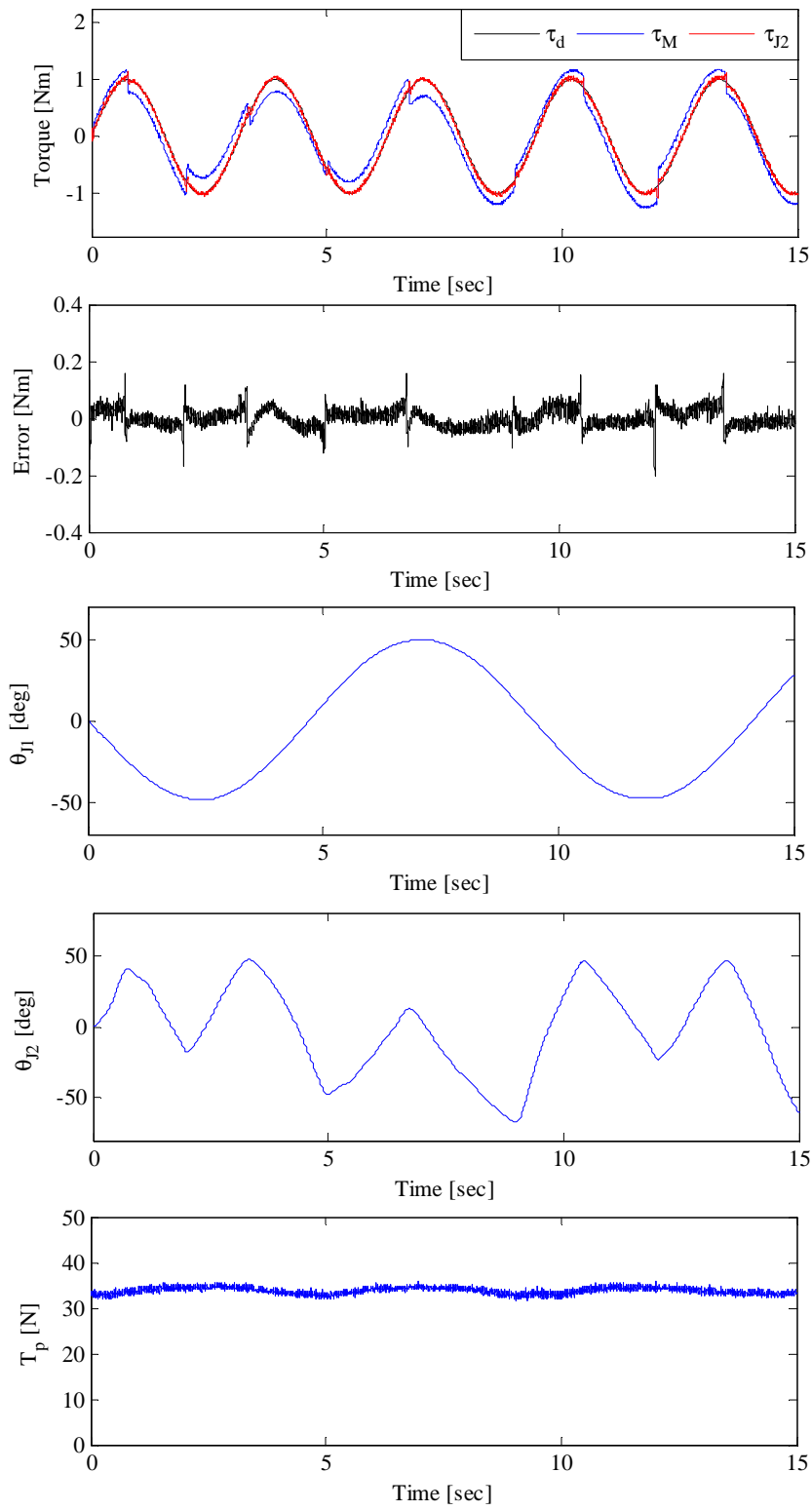


Figure 3-26: Experimental result in the presence friction compensation.

The experimental results in the absence of feedforward friction compensation are shown in Fig. 3-25. Here, the desired torque τ_d served as the reference torque τ_{ref} . τ_{J2} differed greatly from τ_d because of friction, and the direction of friction changed as the rotational direction of the distal joint changed. The error magnitudes varied as the intermediate joint angle changed, again because the friction parameter changed [Root mean square error (RMSE): 0.2228 Nm, Maximum absolute error: 0.3507 Nm]. On the other hand, the addition of feedforward friction compensation afforded good torque tracking (Fig. 3-26). Although the sheath configuration changed on actuation of intermediate joint, τ_{J2} remained in good agreement with τ_d when the friction was feedforwardly compensated. Some tracking error splashes were evident when the direction of movement of the distal joint changed, because the output torque could not be estimated or controlled when the tendons were at static state. Nevertheless, both the RMSE errors and the maximum error magnitudes were smaller than those without the feedforward control. [RMSE : 0.0315 Nm, Maximum absolute error : 0.2022 Nm] The results imply that the friction and friction parameter models are effective for the friction compensation control of tendon-sheath actuation systems. The series elastic elements limited the maximum pretension change to 4.4 N in both experiments, which is sufficiently low for neither tendon slack nor wear to be of concern.

3.2.4.2 A Tele-operation Control Interface with the Proposed Mechanism

A tele-operation control interface (Fig. 3-27) was developed using the proposed tendon-sheath actuation mechanism for the control of a tele-operated robot [13]. The control interface measured user's hand and finger movements and provided force feedback that allowed intuitive control of the remotely controlled robot. Although an exoskeleton structure was developed in Chapter 2, the structure was appropriate to deliver forces to arm segments rather than the hand. Thus, a different type of structure, which can deliver desired forces to a hand, was developed in this chapter. The developed system featured three actively controlled joints that can generate 3-DOFs force feedback to the user's hand. The mass of actuated parts of the system was 2.0 kg. A wearable hand interface was combined with the system to measure the positions of the user's fingers and to provide physical information of manipulated objects [108]. Three 4-DOFs finger structures in the wearable hand interface measured the motions of the thumb, index and middle finger. The finger structures were actuated by DC motors attached on the wearable device, affording force feedback and information on object's size, shape and stiffness. The wearable hand interface was originally developed to transmit forces only to the fingers. In this application, it was modified to deliver the force also to the

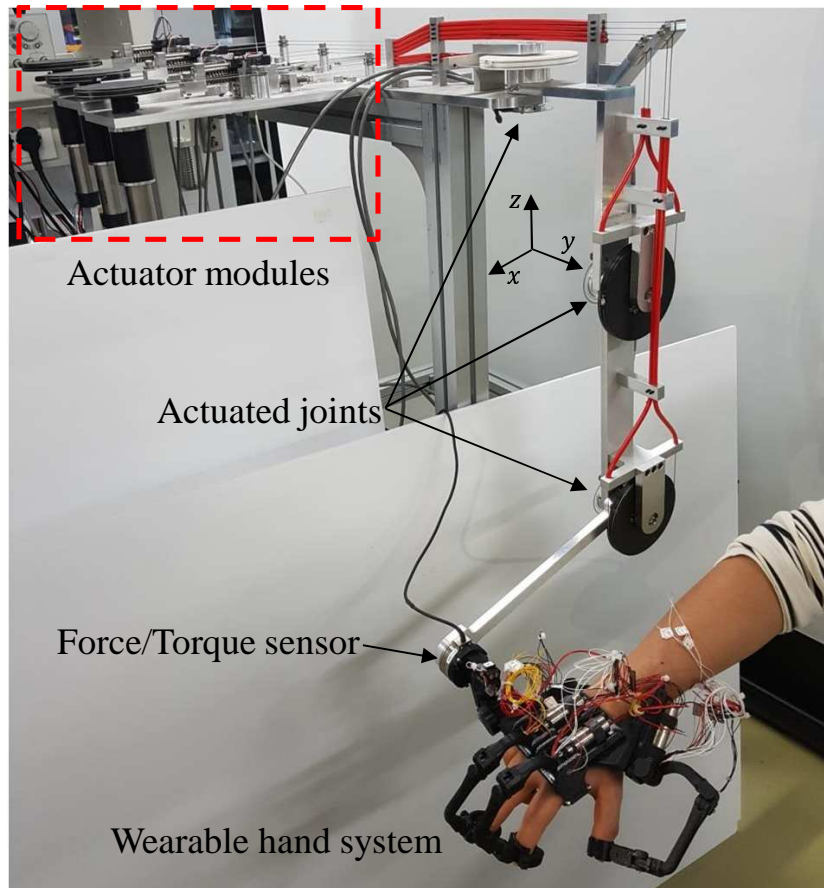


Figure 3-27: A tele-operation control interface featuring the proposed tendon-sheath actuation mechanism.

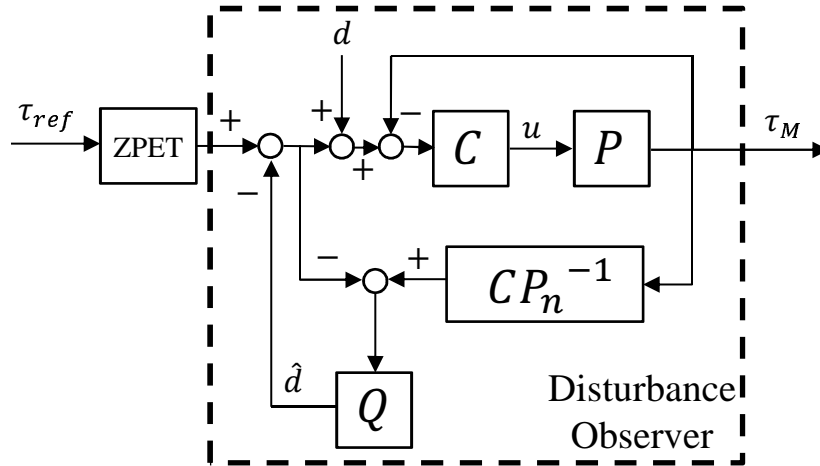


Figure 3-28: Motor torque controller with DOB and ZPET controller. d and \hat{d} are the disturbance and the estimate thereof. Q is the Q filter of DOB. P is the plant that includes the tendon-sheath system, the geared motor, and the series elastic elements of motor side. C and u are, respectively, the controller inside the disturbance observer and the input to the motor.

palm. A 3-DOFs passive rotational joint was fitted to the side of the wearable hand system, which was then tightly fastened to the user’s palm using two velcro straps on the front and back side of the system. Thus, the user could freely move his/her fingers; there was no need to hold the interface. A 6-axis force/torque sensor was placed between the end-effector and wearable hand interface to confirm that the desired forces were delivered to the user’s hand.

To control the torque of each actuated joint, the friction parameter of the tendon-sheath system was modeled as in Chapter 3.2.4.1 The friction parameter of the first joint was constant, because the sheath configuration did not change. The friction parameters of second and third joint were modeled as symmetrical linear functions of intermediate joint angles. The torque of each joint was controlled by a disturbance observer (DOB)-based torque controller combined with a zero phase error tracking (ZPET) controller as shown in Fig. 3-28, improving torque tracking performance by rejecting disturbances such as human motions and modeling uncertainties [98, 109, 110]. The cutoff frequency of the Q filter was set to 10 Hz given that the bandwidths of human joints are about 4-8 Hz [111].

The force delivery performance of the developed control interface was tested experimentally. First, back-drivability of the interface, which ensures free motion of user’s hand, was tested without/with the feedforward friction compensation. In this test, the user moved the hand wearing the control interface. The desired force at the end-effector was set to zero, and the required torques of the joints were calculated kinematically. The weight of the system and bending stiffness of sheaths

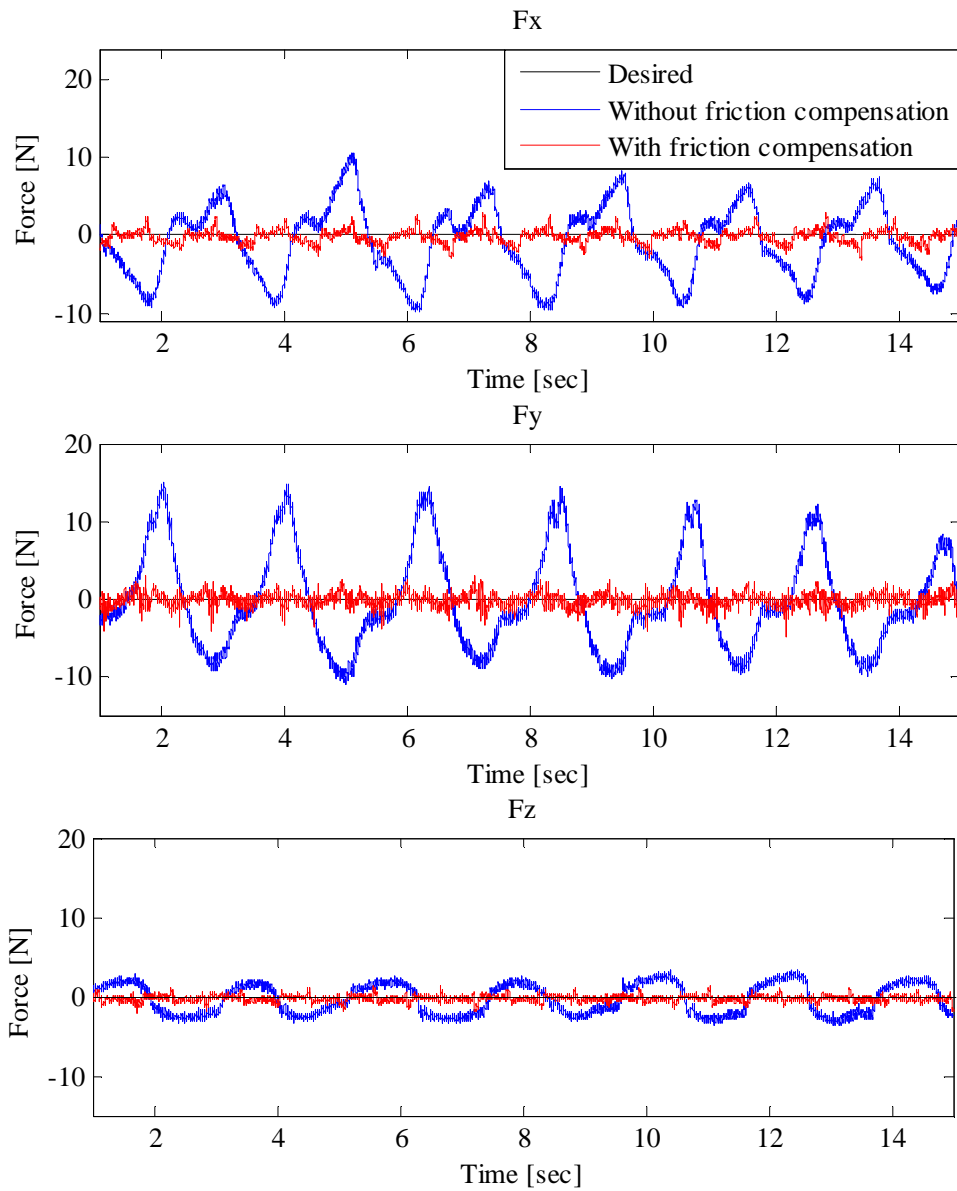


Figure 3-29: Back-drivability test results of the tele-operation control interface.

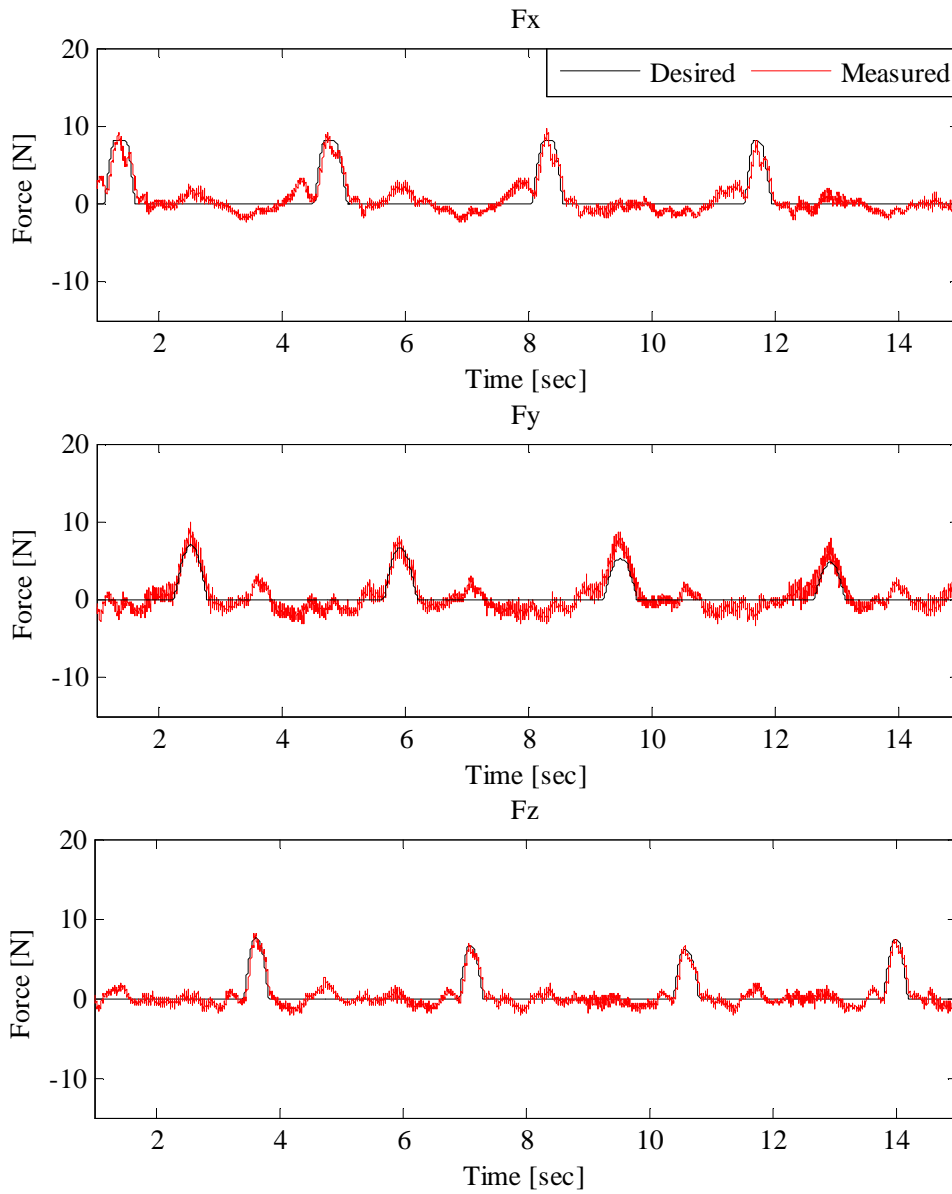


Figure 3-30: Experimental results obtained during interaction with the virtual walls of the tele-operation control interface.

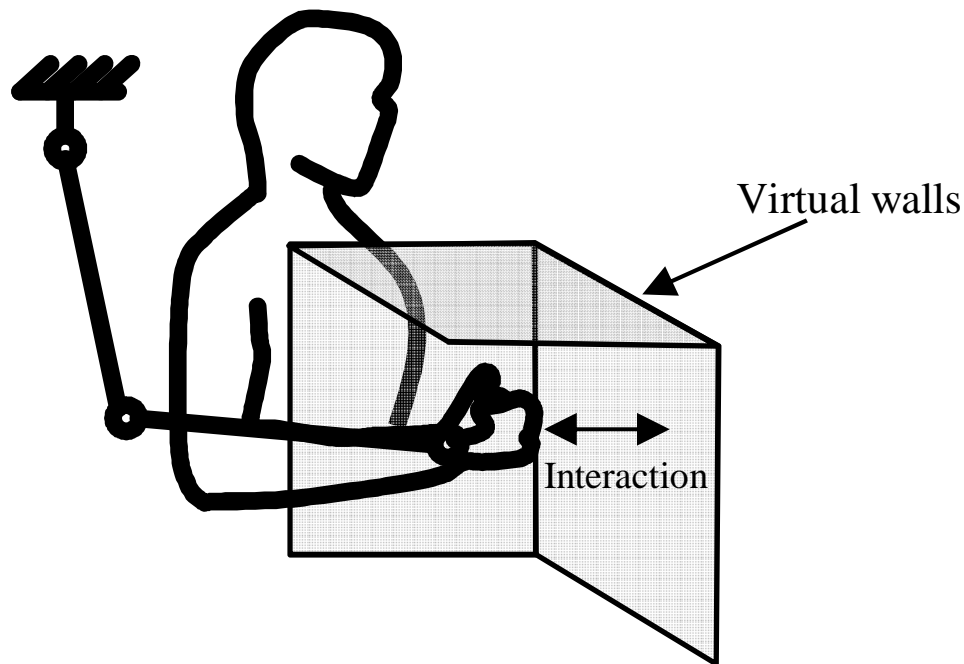
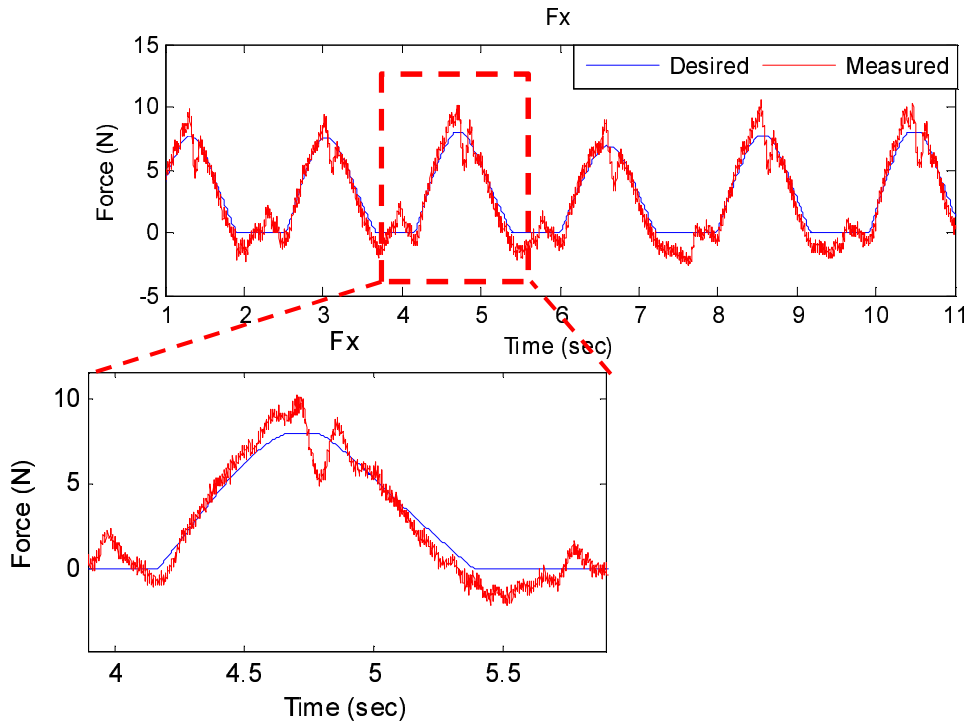


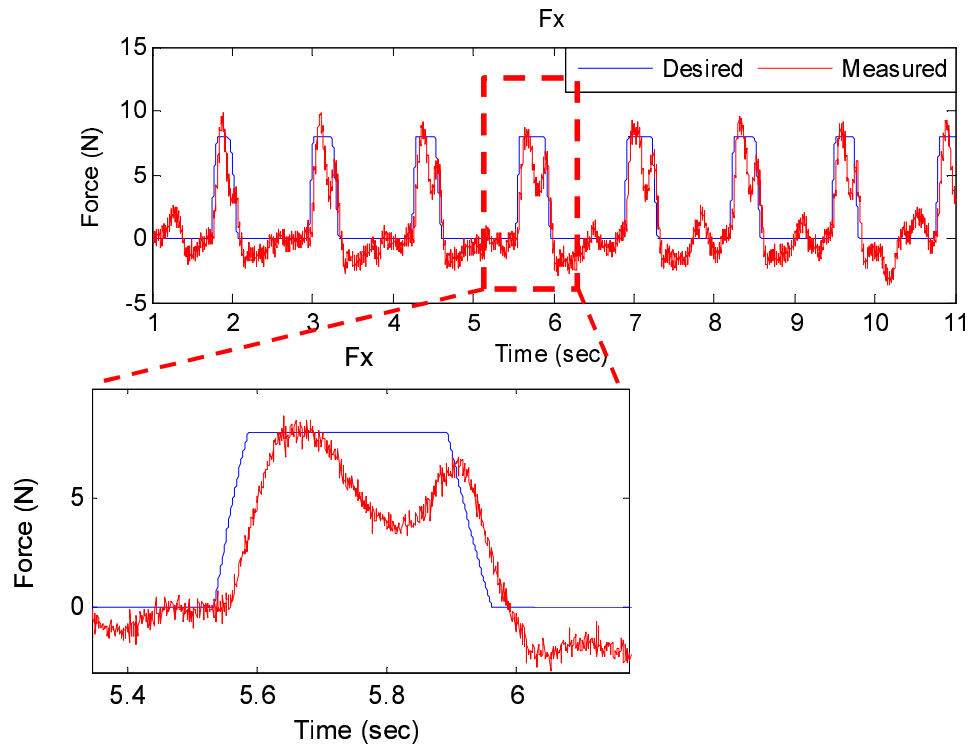
Figure 3-31: Experimental settings for the interaction with the virtual walls.

were compensated. Inertia of the system was ignored because the system is lightweight. The forces delivered to the wearable hand interface were measured by the 6-axis force/torque sensor. Figure 3-29 shows the measured forces without/with feedforward friction compensation, converted to forces in the world coordinate shown in Fig. 3-27. The results in the absence of the friction compensation showed large resistance caused by friction in the tendon-sheath system. [RMSE (Nm) : 4.6325 (Fx), 6.2626 (Fy), 1.9286 (Fz)] On the other hand, the user could move the hand without much resistance when the friction was compensated in a feedforward manner. [RMSE (Nm) : 0.8620 (Fx), 0.7821 (Fy), 0.4534 (Fz)] Also, the error splashes of friction-compensated results evident in Fig. 3-26 were absent, being smoothed by the inertia of the system and the elasticity of user's flesh.

The second test was an interaction test with virtual walls. In this experiment, three virtual walls of stiffness of 0.5 N/mm were set on the x, y and z planes as shown in Fig. 3-31. The user interacted with the three virtual walls while wearing the interface. Figure 3-30 shows the forces measured during the interactions. As the user touched the virtual walls, the desired forces were increased and the interface generated those forces. Compared to the back-drivability test, there are larger errors due to the dynamics of the system, but the desired forces were delivered to the user's hand with only small errors. [RMSE (Nm) : 1.1554 (Fx), 1.1602 (Fy), 0.7495 (Fz)] The experiment was repeated with different virtual wall stiffness. Fig. 3-32 shows the desired and measured forces



(a) Virtual wall stiffness = 0.5 N/mm.



(b) Virtual wall stiffness = 5 N/mm.

Figure 3-32: Experimental results with different virtual wall stiffness.

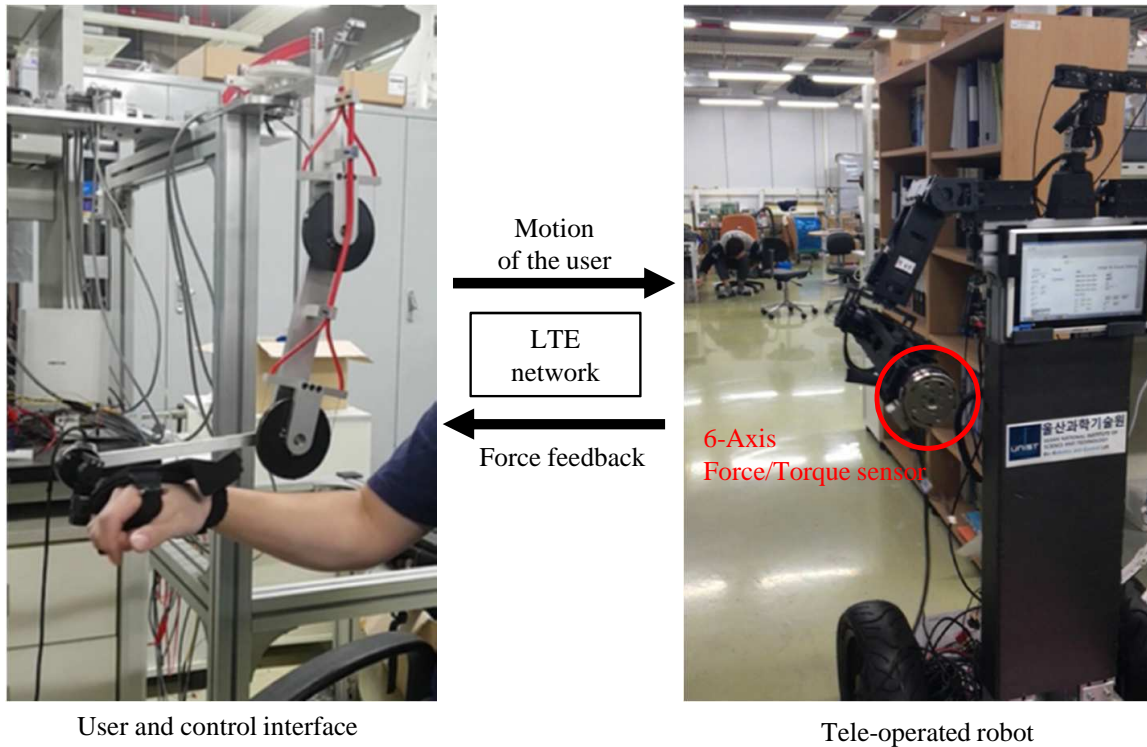


Figure 3-33: Tele-operation experimental setup.

in x-direction when the user interacted with the y-z plane with different virtual wall stiffness (0.5 N/mm and 5 N/mm). As shown in the figures, the measured force follows the desired force in the case of low stiffness wall (0.5 N/mm). [RMSE (Nm) : 0.9064] On the other hand, the measured force showed delayed results from the desired force in the case of high stiffness wall (5 N/mm), with larger errors. [RMSE (Nm) : 1.6663] This is because of the limitation of force bandwidth of the series elastic tendon-sheath actuation system. The linear springs not only lower the pretension change by reducing pretension stiffness, but also lower the torsional stiffness of the system, which leads to low torque bandwidth. This trade-off relationship limits the torque delivery performance of the system. The result also could be affected by the inertia of the system, although the system is lightweight. Thus, modeling and feedforward cancelation of the inertial force are required to improve the force delivery performance.

Preliminary tele-operation experiments were performed with the developed control interface and a robot developed for tele-operations [13]. The robot has two 7-DOF robot arms so that it can follow the user's arm motion. Fig. 3-33 shows the setup for the tele-operation experiment. The user wore the control interface, and moved the robot arm. A robot arm followed user's motion, and the interaction forces between the robot arm and objects were measured by a 6-axis force/torque

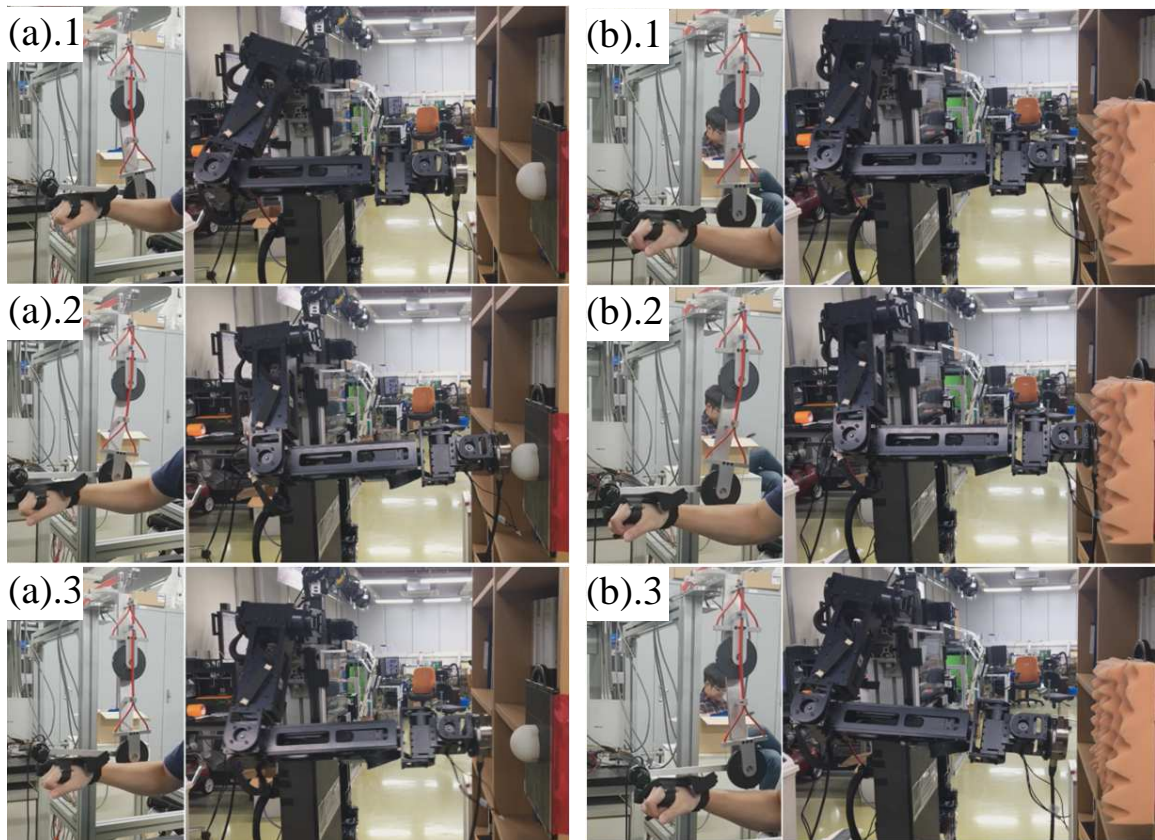


Figure 3-34: Interactions with objects that have different stiffness. (a) A hard silicon, (b) A sponge for packing weak objects. The numbers represent the order in which the scene was captured.

sensor. The measured forces were transmitted to the user side, and the haptic control interface generated the forces. The communication between the user and the robot was performed by a long term evolution (LTE) network to enable long-distance operations. The user interacted with two objects that have different stiffness using the tele-operation system to investigate the interaction performance of the system with unknown environments. In this test, the user moved the robot hand and touched an object in front of the robot. The user turned back the hand after feeling the object. All procedures were performed without providing any visual feedback to the user. As shown in Fig. 3-34, the user could touch and feel unknown objects (a hard silicon and a sponge.) without significant problem. However, the robot moved a little more forward than the user expected, since the interaction force was delivered to the user with network delays. This resulted in a larger interaction forces than the user expected, which might cause stability problem if the environment was much stiffer than the tested objects. Also, as the provided user-side impedance is different from the robot-side impedance, the user may have problems in manipulating objects in a desired way. Such limitations in tele-operation require more investigations in the stability analysis and haptic rendering strategy including the tele-communication network.

3.3 Summary

In Chapter 3, two cable-driven mechanisms were developed for the force control of the haptic interface with lightweight and compact structure. In Chapter 3.1, an asymmetric cable-driven mechanism for the force control of exoskeleton systems was developed. In the proposed mechanism, a linear spring pulled a cable for the joint, while the other cable was driven by the motor. A series elastic mechanism was used for the joint to enable force-mode control of the exoskeleton. A prototype of the exoskeleton for an elbow joint was manufactured to confirm the performance of the proposed mechanism. A proportional and differential (PD) controller with optimal gains for the nominal model of the position control system was used for control of the proposed system. Disturbance observer (DOB) and zero phase error tracking (ZPET) controller were applied in the control structure to compensate for the disturbances induced by the human and the system itself. The experimental results with the exoskeleton system showed that the proposed control algorithm had sufficient back-drivability and precise torque control performance, even in the interaction with a human user. The developed system could provide compact cable routing mechanism, but there were several limitations in practical applications, such as the space requirements of linear springs, decision of the force

asymmetry, and the derailment of the motor side cable in the power-off state. Thus, a different type of cable-driven mechanism was developed in Chapter 3.2.

In chapter 3.2, a series elastic double-tendon-sheath actuation mechanism was developed to overcome the limitations of conventional tendon-sheath actuation mechanisms. Precise feedforward distal joint torque control was achieved at varying sheath configurations by modeling the friction parameter and compensating the friction in a feedforward manner. The series elastic elements allowed the pretension changes to be maintained within a small range, preventing tendon slack and sheath deformation. It was experimentally verified that a desired force can be accurately delivered to a distal joint, even when the sheath configurations varied. A control interface for tele-operation systems was developed with the proposed mechanism, and the performance was tested in several experiments. A DOB-based controller similar to the controller used in Chapter 3.1 was applied for precise force control under interaction with a human user. The proposed haptic control interface was backdrivable, and could deliver desired force to the user. The haptic control interface was also tested in preliminary tele-operation experiments.

Chapter 4

A Display System for Tele-operation

4.1 Introduction

In tele-operated systems, the user observes the field using the images captured by cameras of the robot. The captured images are typically provided to the user by a monitor, which provides only 2D images to the user [112–115]. The display system is very important for the user because the user heavily relies on the visual information, which is the most intuitive information in observing environments. However, the performance of tele-operation system is limited if 3D stereoscopic images are not provided to the user, because the user cannot gauge the distance between objects.

Recently, head mounted display (HMD) systems that can provide immersive 3D visual feedback have been used for the better environment observation and manipulation task performance of the tele-operated robots [12–14]. Most HMDs have an integrated inertial measurement unit (IMU), which can measure the orientation of user's head. The user's head orientation is used to capture the field of view (FOV) in the direction of the same orientation via a robot neck-camera system or a panoramic camera of tele-operated robots. However, it is difficult to provide real-time images to the user in such tele-operated situations, because of the delay mainly caused by latency and limited bandwidth of the tele-communication network and large size of stereoscopic images. The delay and loss of data and unstable nature of wireless tele-communication network result in the time-varying delay of images, which cause simulator sickness [15–17]. The operation delay of robot neck-camera system due to its physical limitation makes the delay even larger. Providing the scene of virtual worlds constructed by point cloud data or image instead of recently captured scene from the robot camera can reduce such problem [12, 39, 40]. However, such methods require large computational burden or expensive sensors such as LIDAR.

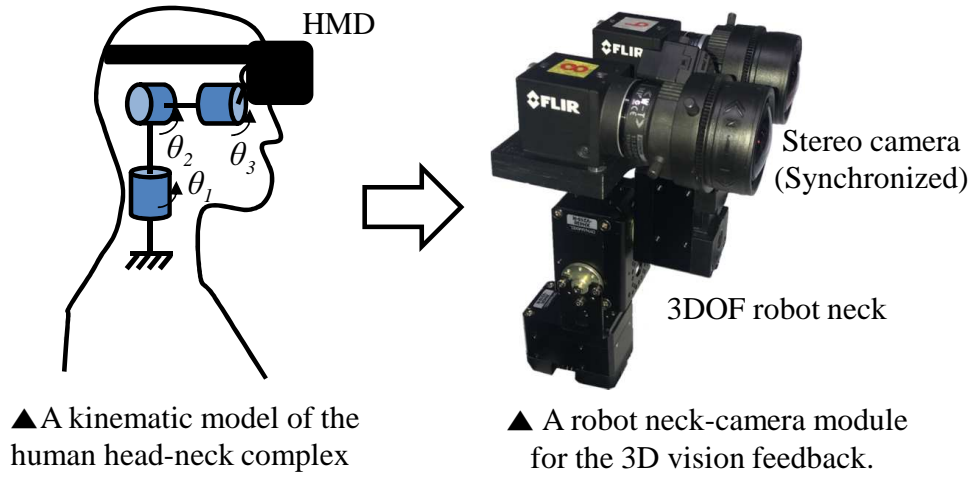


Figure 4-1: Design of a robot neck-camera module based on the kinematic model of human head-neck complex. (θ_1 , θ_2 and θ_3 are the rotation angle of each rotational joints that represents yaw, pitch and roll motion of the head, respectively)

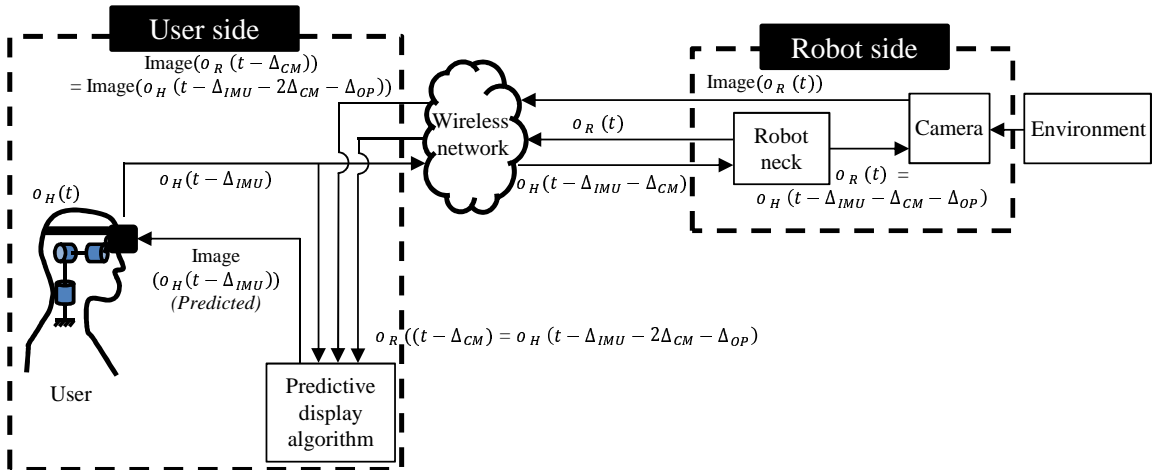
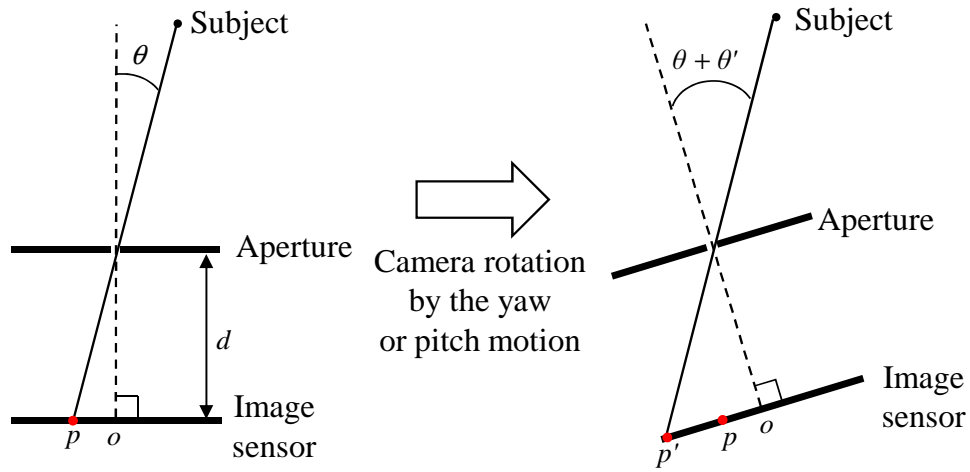
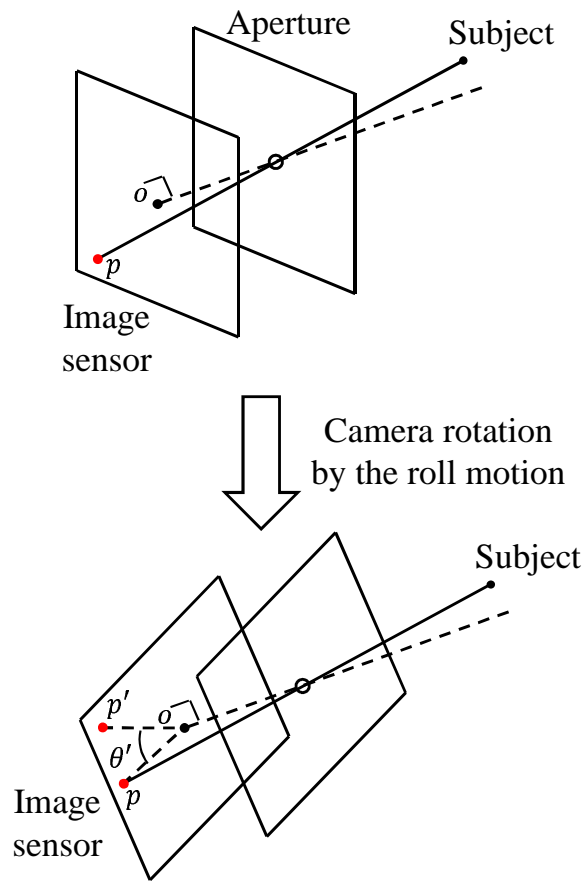


Figure 4-2: Overview of the tele-operated display system. o_H and o_R are the orientation of user's head and robot neck-camera module, respectively. Δ_{IMU} , Δ_{CM} and Δ_{OP} represent the measurement delay of user's head orientation, communication delay of the wireless network and operational delay of the robot neck, respectively.

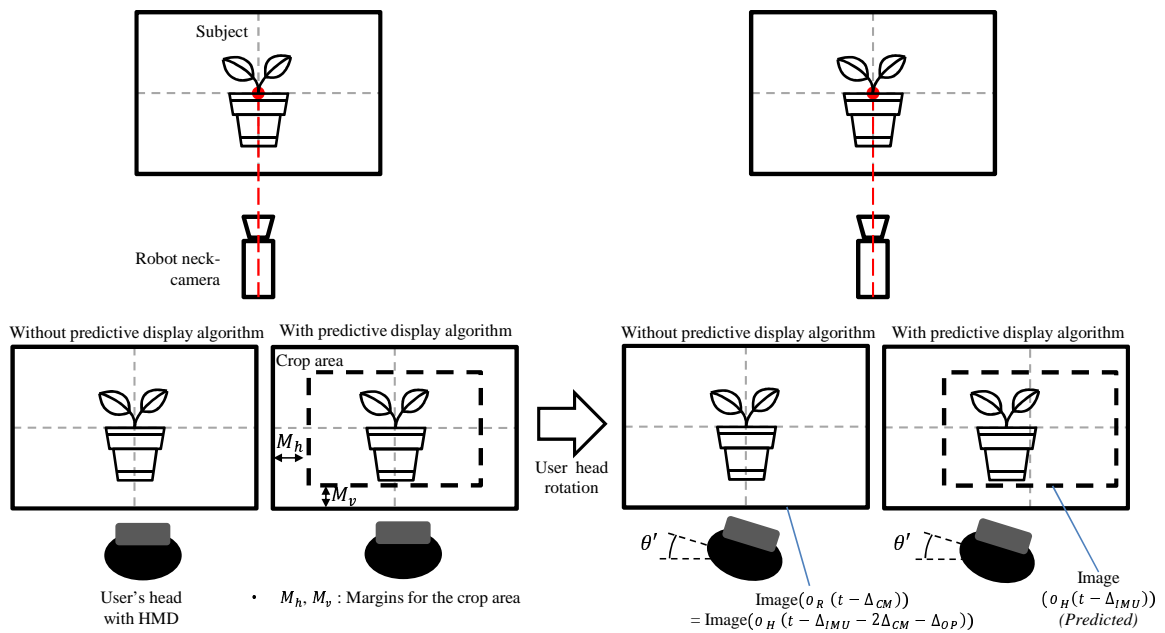


(a) Image position change by the yaw or pitch motion

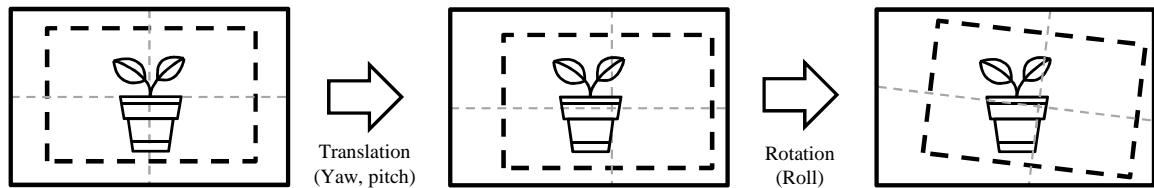


(b) Image position change by the roll motion

Figure 4-3: Simplified camera geometry and image position change of a subject by camera motions



(a) Image prediction for the yaw motion between the image update



(b) Image prediction for the yaw, pitch and roll motions between the image update

Figure 4-4: Implementation procedure of the predictive display algorithm

In this chapter, I propose a tele-operated display system and a practically usable predictive display algorithm for the compensation of the bidirectional network delay and operation delay in a tele-operation system. In the proposed display system, a robot neck-camera system is constructed based on a kinematic model of the human head-neck complex. The predictive display algorithm predicts the image in the direction of current user's head orientation using delayed image and the difference between the delayed robot neck orientation and current user's head orientation. The bidirectional communication delay and operational delay of the image were compensated by translating and rotating the delayed image using kinematic model of the human and robot neck-camera system and the geometrical model of camera.

4.2 Overview of the Display System

A display system was developed for the intuitive observation of the work site of tele-operated robots. As shown in Fig. 4-1, the human head-neck complex was simplified and modeled as a series linkage system with three revolute joints to represent the rotational motion of the head. The HMD [35] attached on the user's head measures the orientation of the head providing 3D stereoscopic images. Based on the kinematic model of the human head-neck complex, a robot neck was designed to have the same kinematic structure of the human model. Also, two cameras [116] were placed on top of the robot neck to capture stereoscopic scene of the work site. In order to prevent user's sickness caused by the time difference of the stereoscopic cameras, the cameras were synchronized by digital signals so that the two cameras capture the image at the same moment. The detailed specifications of the tele-operated display system are shown in Table 4.1.

Fig. 4-2 shows an overview of the tele-operated display system. The orientation of user's head ($o_H(t)$) is measured by an inertial measurement unit (IMU) inside the HMD, with a measurement delay of the IMU (Δ_{IMU}). The measured orientation ($o_H(t - \Delta_{IMU})$) is delivered to the robot neck-camera system through a wireless network with a communication delay (Δ_{CM}), and the robot neck follows the delivered user's head orientation ($o_H(t - \Delta_{IMU} - \Delta_{CM})$) with an operational delay (Δ_{OP}) due to the physical limitation of the actuators. The stereo camera captures stereo images in the direction of robot camera orientation ($o_R(t)$), which is the same as the human neck orientation delayed by Δ_{IMU} , Δ_{CM} and Δ_{OP} , denoted as $o_H(t - \Delta_{IMU} - \Delta_{CM} - \Delta_{OP})$. The captured images (Image($o_R(t)$)) and the orientation when the images were captured ($o_R(t)$) are delivered to the user side with an additional communication delay (Δ_{CM}).

Table 4.1: Specifications of the tele-operated display system

Specification	
HMD	Oculus VR, Oculus Rift Resolution : 960 x 1080 per eye
Motor	ROBOTIS, DYNAMIXEL XH430-V210-R Gear ratio : 212.6:1 No load speed : 52 RPM Stall Torque : 2.6 Nm
Camera	FLIR, FL3-U3-32S2C-CS Image sensor : Sony IMX036, 1/2.8", 2.5 μm Maximum resolution : 2080 x 1552 Maximum frame rate : 60 FPS Lens : FUJIFILM, YV2.8X2.8SA-2

The delivered images can be provided directly to the user through the HMD. However, as noticed in Fig. 4-2, the delivered images ($\text{Image}(o_R(t - \Delta_{CM})) = \text{Image}(o_H(t - \Delta_{IMU} - 2\Delta_{CM} - \Delta_{OP}))$) contain the measurement delay of IMU (Δ_{IMU}), bidirectional communication delay ($2\Delta_{CM}$) and the operational delay of the robot neck (Δ_{OP}). If the image is directly provided to the user, the user could suffer because of the delays. Especially, bidirectional communication delay is a time-varying delay which can cause simulator sickness [15–17]. Also, random loss of the image data, which could frequently occur due to the large data size of stereoscopic images, increases the variation of Δ_{CM} . Such delay and loss of images are not avoidable in tele-operation systems with wireless networks, unless the communication is performed in a very well-controlled situation. Δ_{OP} is also time-varying delay since it depends on the of user's head motion. Δ_{CM} and Δ_{OP} are the dominant delays in the system, because Δ_{IMU} is relatively small and constant. In order to reduce the undesirable effects of Δ_{CM} and Δ_{OP} such as sickness [15–17], we propose a delay compensation algorithm, namely a predictive display algorithm, for the tele-operated display system. The delivered images ($\text{Image}(o_R(t - \Delta_{CM}))$) are modified with the proposed algorithm using the delayed robot neck orientation ($o_R(t - \Delta_{CM})$) and the measured user's head orientation ($o_H(t - \Delta_{IMU})$) before the image is provided to the user. Δ_{CM} and Δ_{OP} , which are dominant time-varying delays of the entire system that affect to the sickness of users, are compensated by the predictive display algorithm.

4.3 A Predictive Algorithm for the Display System

4.3.1 A Predictive Display Algorithm

The geometry of a camera is analyzed to develop the predictive display algorithm. In this analysis, the camera is assumed as a pinhole camera without lens distortion for simplicity. Also, the image sensor of the camera is assumed to have a square shape. The camera model is analyzed by dividing its motions into two cases: the yaw motion or the pitch motion (motion of θ_1 or θ_2 in Fig. 4-1, respectively) and the roll motion (motion of θ_3 in Fig. 4-1) of the robot neck. Fig. 4-3 shows a simplified geometry of a camera, which is composed of an aperture and an image sensor. Fig. 4-3a shows the image formation of a subject on the image sensor and the position change of the formed image by yaw or pitch motion of the robot neck. If a subject is placed in the direction of θ from the perpendicular line of the sensor, the distance from the center of the image sensor to the formed image of the subject (\overline{op}) can be calculated and approximated as follows:

$$\overline{op} = d \tan \theta \approx d\theta \quad (4.1)$$

where d is the distance between the aperture and the image sensor of the camera. If the camera is rotated as much as θ' , the distance is changed into $\overline{op'}$ as follows:

$$\overline{op'} = d \tan(\theta + \theta') \approx d(\theta + \theta') \quad (4.2)$$

Using (4.1) and (4.2), the position change of formed image ($\overline{pp'}$) can be calculated as follows:

$$\overline{pp'} = \overline{op'} - \overline{op} = d\theta' \quad (4.3)$$

Note that the distance $\overline{pp'}$ is proportional to the translation distance of the subject in the captured image in pixel units, δ_{pixel} , which can be expressed as follows:

$$\delta_{pixel} = \alpha d\theta' \quad (4.4)$$

where α is a proportional conversion factor from the distance change of the subject image on the image sensor to that in the captured image in pixel unit. Fig. 4-3b shows the image formation of a subject on the image sensor and its position change by the roll motion of the robot neck by θ' . In

this case, the formed image on the image sensor also rotated by θ' , which leads to the rotation of subject in the captured image by θ' .

The relations between the change of camera orientation and the position change of subject in the captured image can be used to predict future images using current images. If the camera joints which corresponds to θ_1 , θ_2 and θ_3 of human kinematic model are rotated by θ'_1 , θ'_2 and θ'_3 respectively, the future image can be predicted by translating current image by $\alpha d\theta'_1$ in horizontal direction, $\alpha d\theta'_2$ in vertical direction and by rotating the image by θ'_3 . In a similar manner, the scene in the direction of current user's head orientation can be predicted using the current orientation of user's head ($o_H(t - \Delta_{IMU})$), the orientation of the camera when the delayed image was captured ($o_R(t - \Delta_{CM})$), and the delayed image (Image($o_R(t - \Delta_{CM})$)).

The concept of this predictive display algorithm is shown in the Fig. 4-4a. In this case, only the yaw motion (rotation of θ_1) of user's head is considered for the clarity of explanation. The camera captures the image in the direction of current camera orientation, which can be measured by the robot neck system, and both the image (Image($o_R(t)$)) and the robot neck orientation ($o_R(t)$) are delivered to the user side with Δ_{CM} . If the predictive display algorithm is not applied, the delivered image does not change until a new image arrives at the human side. Thus, orientation difference between the user's head orientation ($o_H(t - \Delta_{IMU})$) and the arrived camera orientation ($o_R(t - \Delta_{CM}) = o_H(t - \Delta_{IMU} - 2\Delta_{CM} - \Delta_{OP})$) are generated by the delay.

On the other hand, the predictive display algorithm provides a manipulated image to the user, rather than the original image. For the predictive display, a rectangular crop area is set to the delivered image (Image($o_R(t - \Delta_{CM})$)) with horizontal and vertical margins (M_h and M_v , respectively). If the orientation of user's head is changed, the crop area is translated by $\alpha d\theta'$ pixel in the direction of human head rotation, where θ' is the difference between current user's head orientation ($o_H(t - \Delta_{IMU})$) and delayed robot neck orientation ($o_R(t - \Delta_{CM})$). The image in the translated crop area is provided to the user through the HMD, where the degree of translation is determined by the camera model in (4.4).

In a similar manner, the predictive display algorithm can be applied to all the yaw, pitch and roll motion of the user's head as shown in Fig. 4-4b. The crop area is translated into horizontal and vertical direction by $\alpha d\theta'_1$ and $\alpha d\theta'_2$ respectively, and rotated by θ'_3 , where θ'_1 , θ'_2 and θ'_3 are the yaw, pitch and roll component of the difference between $o_H(t - \Delta_{IMU})$ and $o_R(t - \Delta_{CM})$. Since the predictive algorithm predict the image in the measured user's current head orientation ($o_H(t - \Delta_{IMU})$), the image delay effect of Δ_{CM} and Δ_{OP} is compensated. Thus, the image is

immediately changed following the rotation of user's head with just a delay of Δ_{IMU} , which is considered constant and much smaller than the time-varying delay Δ_{CM} and Δ_{OP} . Therefore, the predictive display algorithm can reduce the discomfort feelings or the sickness of the display system caused by delays.

A delay compensation algorithm was proposed in Edwards' patent with a similar approach [117]. However, the method provides an image smaller than the FOV of HMD, with negative M_h and M_v . Thus, the image shown in the HMD with the algorithm looks like a scene beyond a window that translate and rotate when the image is updated. This may negatively affect to the immersion, limiting the user-side FOV. Although they adopted similar concept with this chapter, there was no analysis about the camera geometry and image position change, which supports the validity of the proposed algorithm in this chapter. Also, there was no consideration about how much margins are necessary for their method, which will be discussed in Chapter 4.3.2.

4.3.2 Margin Analysis

The margins should be set considering the rotational speed of user's head and delay of the image caused by Δ_{CM} and Δ_{OP} . If the crop area is overlapped with the outside of image, the user cannot get a square image anymore, but will get a clipped image since there is no information outside of the image. This may decrease task performance of the tele-operation system reducing immersion of the user. Thus, it is important to set margins M_h and M_v that make the crop area does not reach to the edge of the image. However, large margins lead to small image FOV that makes the amount of provided information small. Because of this trade-off relationship, the margins should be determined as small as possible but enough large to prevent the overlapping of the crop area with the outside of image.

The required margins can be calculated from the image delay, rotational speed of user's head in yaw ($\dot{\theta}_1$), pitch ($\dot{\theta}_2$) and roll ($\dot{\theta}_3$) axis. Fig. 4-5 shows the translation and rotation of the crop area. 4 points on the corners of the crop area are denoted as A , B , C and D . Since one of these points is first point that may reach the edge of the image when the crop area start to overlap with outside of the image, it is necessary set the margins make these points stay inside of the image. The margin analysis is started from the margin of point A that have initial coordinates (x_A, y_A) . The distances between point A to the closest horizontal and vertical edge of the image are denoted to $M_{h,A}$ and $M_{v,A}$. The coordinate of point A before translating and rotating the crop area can be calculated as

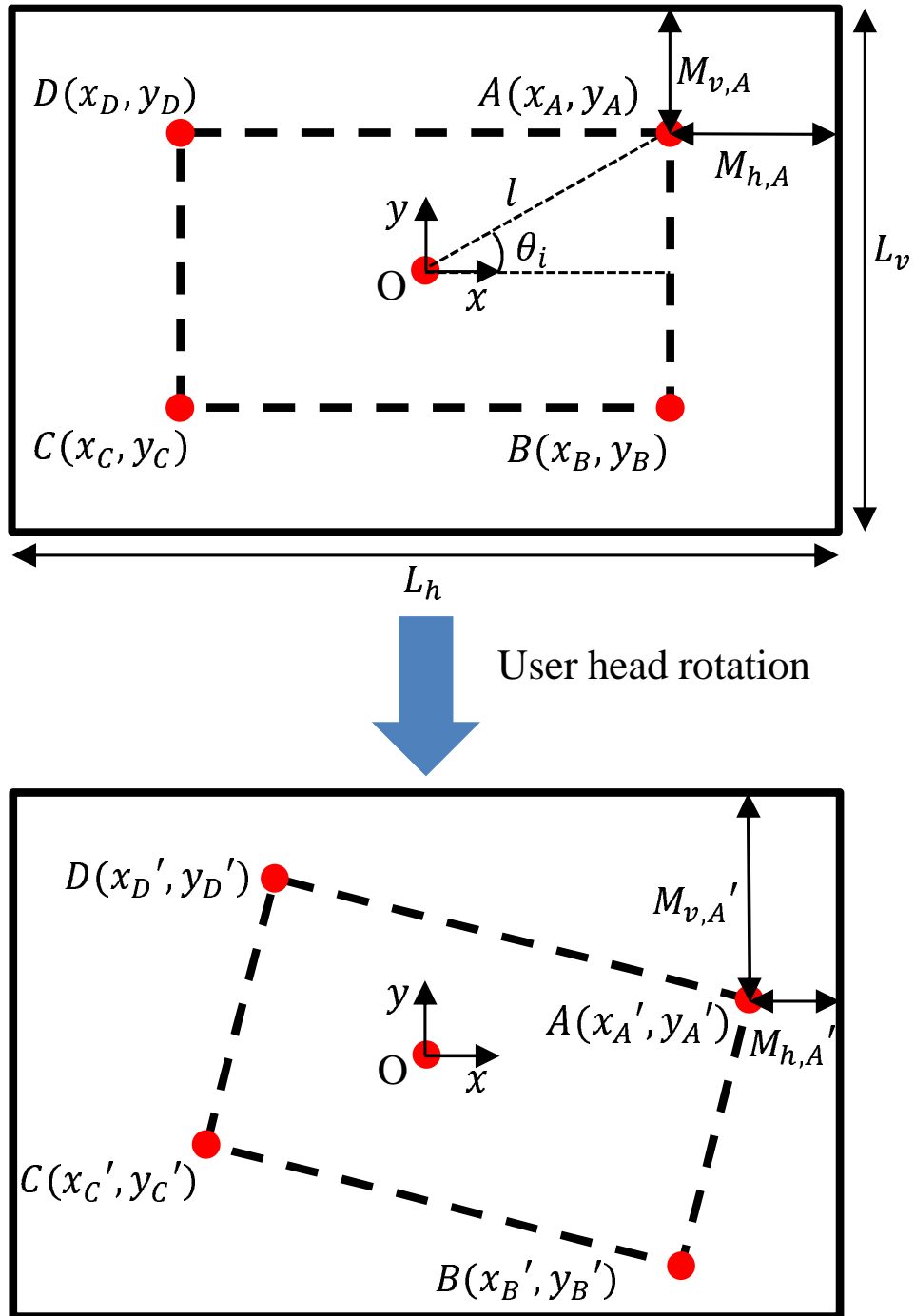


Figure 4-5: Margin changes by the translation and rotation of the crop area

follows:

$$x_A = l \cos \theta_i \quad (4.5)$$

$$y_A = l \sin \theta_i \quad (4.6)$$

where l is the distance from the center of the image to the point A , and θ_i is the angle between the horizontal line and \overline{OA} , and can be calculated using the margins and size of image as follows:

$$l = \sqrt{(L_h/2 - M_h)^2 + (L_v/2 - M_v)^2} \quad (4.7)$$

$$\theta_i = \text{atan} \left(\frac{L_v/2 - M_v}{L_h/2 - M_h} \right) \quad (4.8)$$

Before the manipulation of the crop area, $M_{h,A}$ and $M_{v,A}$ are identical to M_h and M_v . As the crop area is translated and rotated, the coordinate of point A is changed as follows :

$$x'_A = l \cos(\theta_i + \theta'_3) + \alpha d \theta'_1 \quad (4.9)$$

$$y'_A = l \sin(\theta_i + \theta'_3) + \alpha d \theta'_2 \quad (4.10)$$

Assuming the image delay is dt and the rotational speeds of users are $\dot{\theta}_1, \dot{\theta}_2, \dot{\theta}_3$ about yaw, pitch and roll axis, the position change of point A by user's motion during the delayed time dt can be calculated as follows:

$$x'_A = l \cos(\theta_i - \omega_3 dt) - \alpha d \omega_1 dt \quad (4.11)$$

$$y'_A = l \sin(\theta_i - \omega_3 dt) + \alpha d \omega_2 dt \quad (4.12)$$

The position change of point A results into the change of margins $M_{h,A}$ and $M_{v,A}$ as follows:

$$M'_{h,A} = L_h/2 - x'_A \quad (4.13)$$

$$M'_{v,A} = L_v/2 - y'_A \quad (4.14)$$

To make the crop area does not reach to the edge of the image, $M_{h,A}$ and $M_{v,A}$ must satisfy following margin criteria:

$$M'_{h,A} > 0 \quad (4.15)$$

$$M'_{v,A} > 0 \quad (4.16)$$

In a similar manner, the coordinates and margins of other three points after manipulation of the crop area can be obtained as:

$$x'_B = l\cos(\theta_i + \omega_3 dt) - \alpha d\omega_1 dt \quad (4.17)$$

$$y'_B = -l\sin(\theta_i + \omega_3 dt) + \alpha d\omega_2 dt \quad (4.18)$$

$$x'_C = -l\cos(\theta_i - \omega_3 dt) - \alpha d\omega_1 dt \quad (4.19)$$

$$y'_C = -l\sin\theta_i - \omega_3 dt) + \alpha d\omega_2 dt \quad (4.20)$$

$$x'_D = -l\cos(\theta_i + \omega_3 dt) - \alpha d\omega_1 dt \quad (4.21)$$

$$y'_D = l\sin(\theta_i + \omega_3 dt) + \alpha d\omega_2 dt \quad (4.22)$$

$$M'_{h,B} = L_h/2 - x'_B \quad (4.23)$$

$$M'_{v,B} = L_v/2 - y'_B \quad (4.24)$$

$$M'_{h,C} = L_h/2 - x'_C \quad (4.25)$$

$$M'_{v,C} = L_v/2 - y'_C \quad (4.26)$$

$$M'_{h,D} = L_h/2 - x'_D \quad (4.27)$$

$$M'_{v,D} = L_v/2 - y'_D \quad (4.28)$$

, and the margins in (4.23)-(4.28) must remain positive to make the crop area does not reach to the edge of the image. Using this margin criteria, the minimum required margins can be calculated by applying maximum angular velocity of user's head with the delay of image into the margin criteria. The problem is that the delay of image can significantly vary as the tele-communication network condition is changed. To address this problem, the margins can be calculated and applied in realtime, because the predictive display algorithm does not require large computational burden. However, the variation of margins also change the FOV of images, which may cause sickness of the user. Thus, the margins were set in an empirical manner in the following performance tests.

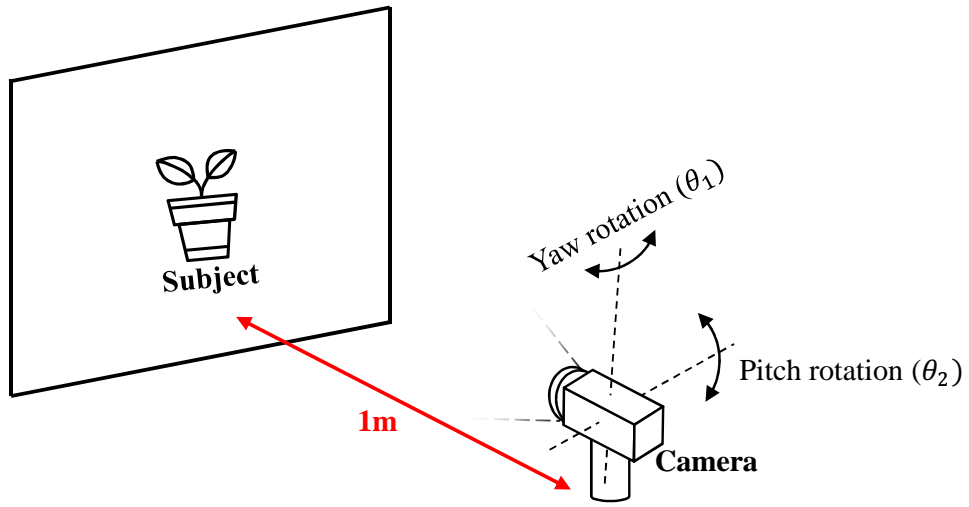
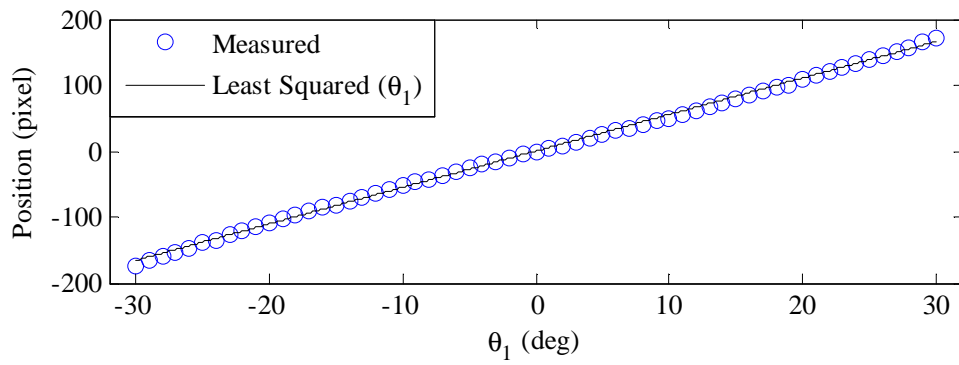
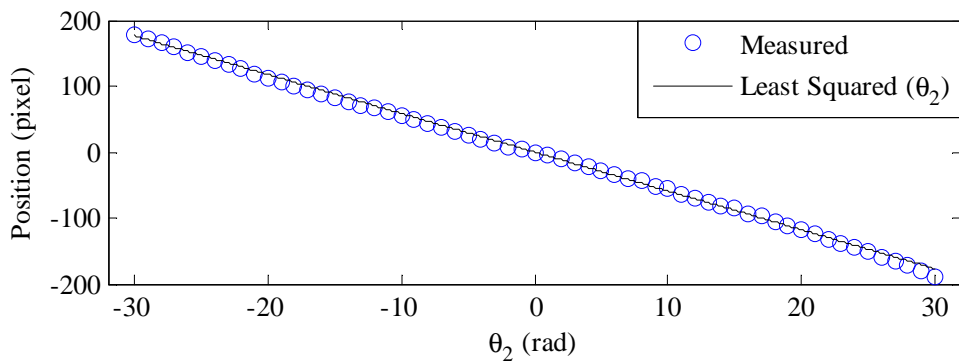


Figure 4-6: Experimental setup for the parameter identification



(a) Yaw motion



(b) Pitch motion

Figure 4-7: Identification result of camera parameter αd by yaw and pitch motions

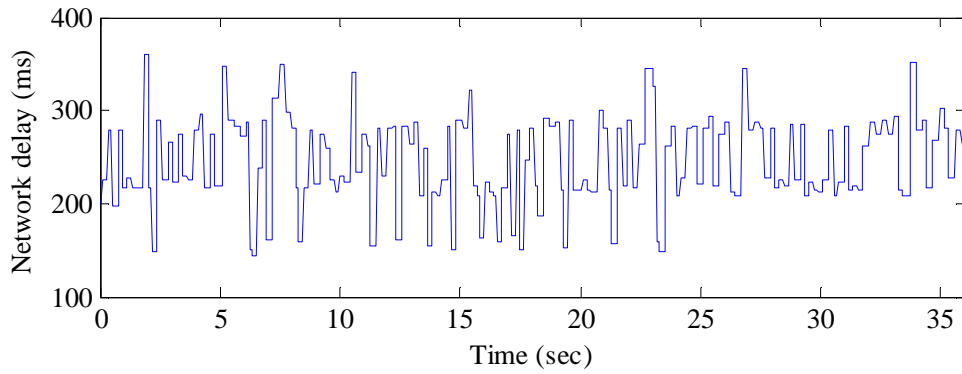
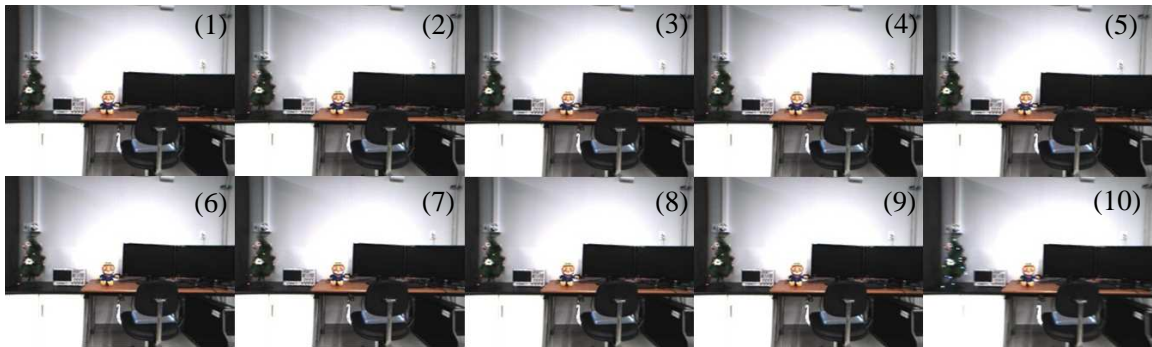
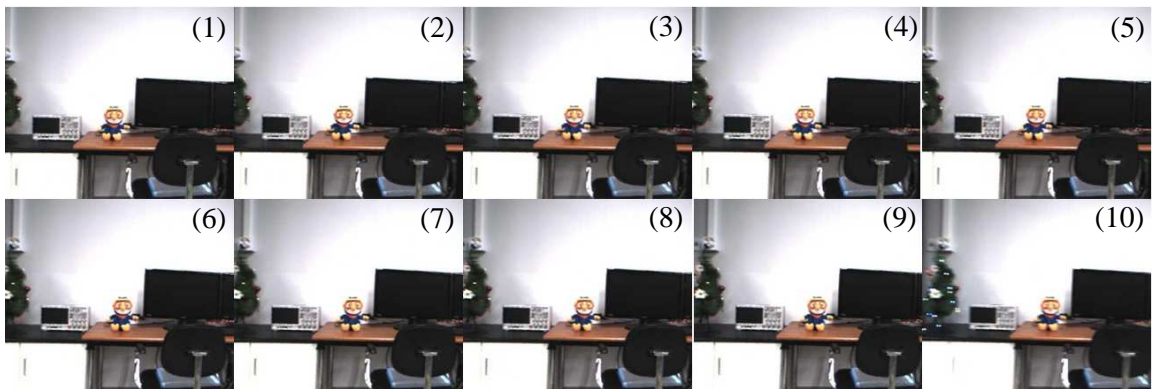


Figure 4-8: Measured network delay



(a) Images without the predictive display algorithm (No change while the image had not been updated before (10))



(b) Images with the predictive display algorithm (Continuous change even while the image had not been updated before (10))

Figure 4-9: Captured images of the tele-operation experiment

4.4 Experiments

4.4.1 Parameter Identification

To apply the predictive display algorithm, the camera parameter αd in (4.4) was identified by an experiment. Fig. 4-6 shows the experimental setup for the parameter identification. The robot neck-camera module was fixed at a place, and a subject was installed in front of the camera with a distance of 1m, to be placed at the center of the captured image when the robot neck was at initial position. The robot neck was rotated in yaw or pitch orientation from -30° to 30° in 1° of step while the camera captures images. The distances between the subject in the captured images and the center of the images were recorded in pixel units. αd was identified by linearly fitting αd to (4.4) using the recorded positions and rotation angles with least square method. As a result, αd was identified as $\alpha d = 5.5$ pixel/deg for the yaw motion, and $\alpha d = 5.9$ pixel/deg for the pitch motion. Fig. 4-7a and Fig. 4-7b show the measured positions of the subjects and the linearly fitted model for the yaw motion and pitch motion of the robot neck, respectively. As shown in the graphs, the measured data fit well with the camera model in (4.4). The identified parameters show a slight difference in yaw and pitch motion, which is considered as the effect of lens distortion or asymmetry of the image sensor shape.

4.4.2 Implementation of the Predictive Display Algorithm

The predictive display algorithm was tested in a tele-operation experiment. The experimental setup was the same as the description of Fig. 4-2. The user wore the HMD and rotated the head. The orientation of user's head was measured and delivered to the robot neck-camera module through a wireless network, and the robot neck followed user's motion while a stereo camera capture the images of the environment with a resolution of 554×413 pixels each. The captured images and the robot neck orientation when the images were delivered to the user side. A random communication delay was intentionally added to the wireless network assuming a reasonable network condition in practical applications. The resulted images without/with the proposed predictive display algorithm were recorded. In the experiment, the margins of predictive display algorithm, M_h and M_v , were set to 90 and 50 pixels, respectively. Considering the frame rate of general digital videos are 30 frames per second (FPS), the prediction of images was performed in 30 Hz. The bidirectional network delay during the experiment is shown in Fig. 4-8. The minimum, average, maximum and the standard

deviation of the delay in the experiment were 145 ms, 245 ms, 361 ms and 48 ms respectively. Fig. 4-9 shows captured images between a set of updated images, scene (1) and (10), without/with the predictive algorithm under the same experimental conditions. Without the predictive algorithm, the captured images are not changed until new images arrive to the user side as shown in Fig. 4-9a. On the other hand, the images modified by the predictive algorithm are continuously changed by the user's head rotation as shown in Fig. 4-9b. As shown in Fig. 4-9, the delay-compensated images are much smooth and natural than without the predictive display algorithm. The predicted images were also maintained desired frame rate (30 FPS) under the unpredictable time-varying delay. The results imply that the proposed display system with the predictive display algorithm can provide comfortable use of HMDs for tele-operation systems.

4.5 Summary

In this chapter, a display system with a predictive display algorithm was developed. A robot neck-camera module was designed and manufactured based on a kinematic model of human head-neck complex. The delay of an image in the tele-operation of the display system was analyzed, which may cause simulator sickness. To reduce the sickness caused by the time-varying delay of the display system, a predictive display algorithm was developed based on the camera geometry and human and robot kinematic model. The image in the current user's head orientation was predicted and provided to the user, using the difference between the current user's head orientation and delayed camera orientation. As the result, the time-varying delays in communication and operation were compensated, and it was able to provide continuous images to the user.

Chapter 5

Concluding Remarks and Open Issues

This thesis presented a wearable control interface for tele-operated robot, including (1) design of wearable control interface structures, (2) design and control of cable-driven actuation mechanisms, and (3) a tele-operated display system.

5.1 Design of Wearable Control Interface Structures

In Chapter 2, an exoskeleton structure was designed to allow user's natural motion and address singularity problem. A vertical prismatic joint was added to a traditional 3-DOF shoulder joint of exoskeleton structures, and the shoulder joint was tilted to replace the singularity position to the outside of workspace. The designed structure was analyzed by kinematic methods, and its performance was verified by experiments with a user. Since exoskeletons should be connected to the user's body segments, it is difficult to deliver desired forces only to the hand without delivering forces to other segments. Because of this fundamental limitation of exoskeleton structure, a different type of structure was developed in Chapter 3.2.

In Chapter 3.2, an end-effector type wearable control interface was designed for the verification of the tendon-sheath actuation mechanism. The interface had three actively controlled joints and three passive joints that can deliver desired force to the user's hand. A wearable hand exoskeleton was placed at the end of the interface to connect the hand to the control interface and to provide force feedback to fingers. The structure could be designed to be lightweight thanks to the tendon-sheath actuation mechanism. Although the structure could measure the user's motion and deliver desired forces to the hand, the workspace was not enough to cover the user's range of motion. Larger workspace is required to fully utilize an arm of tele-operated robots, since they usually have

similar dimensions with human's arm. Interference between the interface and user also should be adjusted to enlarge available range of motion. Replacing passive joints between the wearable hand interface and the linkage structure to active joints could improve user's sensation by providing torque feedback.

5.2 Design and Control of Cable-driven Actuation Mechanisms

Lightweight actuation mechanisms were developed utilizing flexible cables for the force transmission. In Chapter 3.1, an asymmetric cable-driven mechanism was developed to simplify cable routing structures. By replacing a cable to a linear spring, a rotational joint could be actuated routing just one cable from the actuator to the actuated joint. A rotary series elastic mechanism was adopted to enable precise force delivery. The system was controlled by a DOB-based robust control algorithm to reject the modeling uncertainties and effects from human-robot interactions. A prototype exoskeleton was developed, and it was tested in a tele-operation experiment with a commercial robot arm. The user could control a joint of the robot arm feeling the weight of an object. Although the proposed mechanism allows simple cable routing, the linear spring required certain amount of place, which could make the system bulky in multi-DOF systems. Also, it is difficult to set the asymmetry of the joint force, and the cable often derailed from the pulleys if the power of the motor is turned off. Thus, the application of the proposed mechanism in multi-DOF systems is practically difficult.

In Chapter 3.2, a new tendon-sheath actuation mechanism was developed. The proposed mechanism addressed two major problems in tendon-sheath actuation mechanisms: the friction and large pretension change under varying sheath configuration. The pretension change was reduced by adopting series elastic elements. Friction between the tendon and the sheath was analyzed and modeled. Feedforward torque control under varying sheath configuration was achieved by feedforwardly compensating the friction. The disadvantage of the proposed mechanism is that the pretension stiffness is in a trade-off relationship with the torsional stiffness of the system, which affects to the torque bandwidth. A haptic control interface with the proposed mechanism was developed and tested, and it showed good backdrivability, because the friction was successfully compensated. However, there was a limitation in rendering hard objects, because of the aforementioned torque bandwidth limitation. A modified mechanism, which decouples the pretension stiffness and the torsional stiffness, is being developed to overcome the disadvantage.

5.3 A Tele-operated Display System

In Chapter 4, a vision feedback system was developed with a head mounted display (HMD) and a synchronized stereo camera with a 3 DOFs robot neck. The robot neck follows the user's head orientation measured by the HMD, and the stereo camera captures a 3D image at the orientation. The user could get depth information of the field from the stereoscopic images provided by the HMD. A predictive display algorithm that compensates the delay in the tele-communication was developed and implemented to the vision system to prevent discomforts from the delay. The images were sent to the user together with the orientation in which the image was taken. A delay-compensated stereoscopic image, predicted using the orientation difference between the user and the robot neck, was provided to the user. The generated images showed smooth changes even under large delays and loss. Since the predictive display algorithm reduce field of view (FOV) of provided image, the user get less information when the algorithm is applied. This is a fundamental limitation of the algorithm.

Challenging tasks remain in the predictive display algorithm. The modeling uncertainties of the camera geometry, such as the tangent approximation and pinhole camera model, are needed to be reflected in the predictive display algorithm. The decision strategy of margins for the crop area, M_h and M_v , is required to be developed to decide proper margins in various tele-communication network conditions. Also, the predictive display algorithm does not instantly reflect the change of environment, because the predictive display algorithm use delayed images. Nevertheless, the proposed predictive display algorithm is practically useful for many tele-operation applications because of its simple algorithm and low cost in terms of computational burden. User evaluation in various situations is necessary to quantitatively evaluate the improvement of user's comfortableness by the predictive display algorithm, which requires much effort.

5.4 Issues in Tele-operation

This thesis focused on the development of an intuitive control interface for tele-operation systems. The developed control interface itself somewhat properly functioned, but applications of the interface to tele-operation systems could be more challenging works. Since the control interface and tele-operated robot will communicate with wireless communication networks in the supposed applications, delay and loss of data packet are inevitable. Such disturbances will negatively affect to

the transparency and stability of the tele-operation system. Since the robot follows the delivered user's motion with network delay, and the interaction force with the environment is transmitted to the user side with additional delay, the environment that the user feels will be different from real environment. In Chapter 4, the similar delay effect in the visual feedback system was compensated by a camera model and kinematic models of human and robot neck. However, it is difficult to apply such method in the force feedback, since every environment has different properties unlike the camera geometry and human and robot neck kinematics. Modeling the physical property of the environment (e.g. size, shape and mechanical impedance) in real time may be a solution. By generating the model in a virtual space and providing it to the user via a haptic interface, the user can feel the physical properties of the environment without delay effect. However, performing dexterous tasks with such model will be difficult, because the actual position and force of the robot become different from user's force and position.

The performance of tele-operation system can be improved by teaching frequently required tasks to the robot, and let the robot perform the task by itself. The importance of the control interface could be reduced in such case, but it will be still useful to deliver user's intentions to the robot, which is important in various tasks required in unpredictable disaster sites. For example, the user can use the interface to command specific orders for a task, such as where and when to start, how large should be the trajectory, how fast the task should be performed or how much force should be applied in the task. Commanding such requirements with traditional control interfaces will take at least a few minutes, but it can be performed in few seconds with intuitive haptic interfaces.

References

- [1] Y. Jung and J. Bae, “Kinematic analysis of a 5-dof upper-limb exoskeleton with a tilted and vertically translating shoulder joint,” *IEEE/ASME Transactions on Mechatronics*, vol. 20, pp. 1428–1439, 2015.
- [2] —, “Kinematic analysis of a 5 dof upper-limb exoskeleton with a tilted and vertically translating shoulder joint,” in *Proceedings of IEEE/ASME International Conference on Advanced Intelligent Mechatronics (AIM)*, 2013, pp. 1643–1648.
- [3] —, “Performance verification of a kinematic prototype 5-dof upper-limb exoskeleton with a tilted and vertically translating shoulder joint,” in *Proceedings of IEEE/ASME International Conference on Advanced Intelligent Mechatronics (AIM)*, 2014, pp. 263–268.
- [4] —, “An asymmetric cable-driven mechanism for force control of exoskeleton systems,” *Mechatronics*, vol. 40, pp. 41–50, 2016.
- [5] —, “An asymmetric cable-driven mechanism for force control of exoskeleton systems,” in *Proceedings of IEEE/RSJ International Conference on Intelligent Robots and Systems (IROS)*, 2016, pp. 273–278.
- [6] —, “Simulation analysis on friction compensation of a double tendon-sheath actuation system,” in *Proceedings of International Conference on Ubiquitous Robots and Ambient Intelligence (URAI)*, 2016, pp. 510–514.
- [7] —, “Torque control of a double tendon-sheath actuation mechanism in varying sheath configuration,” in *Proceedings of IEEE International Conference on Advanced Intelligent Mechatronics (AIM)*, 2017, pp. 1352–1356.
- [8] L. Bevere, R. Sharan, S. Barrett, and C. Honegger, *Natural catastrophes and man-made disasters in 2016*. Swiss Re Institute, 2017.

- [9] D. Guha-Sapir, P. Hoyois, P. Wallemacq, and R. Below, *Annual Disaster Statistical Review 2016: The Numbers and Trends*. Centre for Research on the Epidemiology of Disasters (CRED), 2017.
- [10] J. Chestnutt and P. Michel, “An intelligent joystick for biped control,” in *Proceedings of the IEEE International Conference on Robotics and Automation (ICRA)*, 2006, pp. 860–865.
- [11] A. Nawab and K. Chintamani, “Joystick mapped augmented reality cues for end-effector controlled tele-operated robots,” in *Proceedings of the IEEE Virtual Reality Conference*, 2007, pp. 263–266.
- [12] M. Schwarz, D. D. T. Rodehutsors and, M. Beul, M. Schreiber, N. Araslanov, I. Ivanov, C. Lenz, J. Razlaw, S. Schuller, D. Schwarz, A. Topalidou-Kyniazopoulou, and S. Behnke, “Nimbro rescue: Solving disaster-response tasks with the mobile manipulation robot marmo,” *Journal of Field Robotics*, vol. 34, pp. 400–425, 2017.
- [13] S. Park, Y. Jung, and J. Bae, “An interactive and intuitive control interface for a tele-operated robot (avatar) system,” vol. 55, pp. 54–62, 2018.
- [14] C. L. Fernando, M. Furukawa, T. Kurogi, S. Kamuro, K. Sato, K. Minamizawa, and S. Tachi, “Design of telesar v for transferring bodily consciousness in telexistence,” in *Proceedings of the IEEE/RSJ International Conference on Intelligent Robots and Systems (IROS)*, 2012, pp. 5112–5118.
- [15] J. J. Golding, D. Phil, and H. M. Markey, “Effect of frequency of horizontal linear oscillation on motion sickness and somatogravic illusion,” *Aviation, space, and environmental medicine*, vol. 67, pp. 121–126, 1996.
- [16] M. E. S. Pierre, S. Banerjee, A. W. Hoover, and E. R. Muth, “Simulator sickness depends on frequency of the simulator motion mismatch: An observation,” *Presence: Teleoperators and Virtual Environments*, vol. 17, pp. 584–593, 2008.
- [17] —, “The effects of 0.2 hz varying latency with 20° – 100 ms varying amplitude on simulator sickness in a helmet mounted display,” *Displays*, vol. 36, pp. 1–8, 2015.
- [18] T. Hulin and J. K. Salisbury, “The phantom haptic interface: A device for probing virtual objects,” in *Proceedings of the ASME winter annual meeting, symposium on haptic interfaces for virtual environment and teleoperator systems*, 1994, pp. 295–300.

- [19] D. Systems. (2018) Touch. [Online]. Available: <https://www.3dsystems.com/>
- [20] A. Tobergte, P. Helmer, U. Hagn, P. Rouiller, S. Thielmann, S. Grange, A. Albu-Schaffer, F. Conti, and G. Hirzinger, “The sigma.7 haptic interface for mirosurge: A new bi-manual surgical console,” in *Proceedings of the IEEE/RSJ International Conference on Intelligent Robots and Systems (IROS)*, 2011, pp. 3023–3030.
- [21] F. Dimension. (2018) Sigma.7. [Online]. Available: <http://www.forcedimension.com/>
- [22] C. Systems. (2018) Cyberforce. [Online]. Available: <http://www.cyberglovesystems.com/>
- [23] HAPTION. (2018) Inca 6d. [Online]. Available: <https://www.haption.com/>
- [24] T. Hulin, K. Hertkorn, P. Kermer, S. Schatzle, J. Artigas, M. Sagardia, F. Zacharias, and C. Preusche, “The dlr bimanual haptic device with optimized workspace,” in *Proceedings of the IEEE International Conference on Robots and Automation (ICRA)*, 2011, pp. 3441–3442.
- [25] T. Endo, H. Kawasaki, T. Mouri, Y. Ishigure, H. Shimomura, M. Matsumura, and K. Koketsu, “Five-fingered haptic interface robot: Hiro iii,” *IEEE Transactions on Haptics*, vol. 4, pp. 14–27, 2011.
- [26] G. Lee, S. Hur, and Y. Oh, “High-force display capability and wide workspace with a novel haptic interface,” *IEEE/ASME Transactions on Mechatronics*, vol. 22, pp. 138–148, 2017.
- [27] J. C. Perry, J. Rosen, , and S. Burns, “Upper-limb powered exoskeleton design,” *IEEE/ASME Trans. Mechatron.*, vol. 12, pp. 408–417, 2007.
- [28] A. Frisoli, F. Salsedo, M. Bergamasco, B. Rossi, and M. C. Carboncini, “A force-feedback exoskeleton for upper-limb rehabilitation in virtual reality,” *Applied Bionics and Biomechanics*, vol. 6, pp. 115–126, 2009.
- [29] A. Schiele and G. Hirzinger, “A new generation of ergonomic exoskeletons-the high-performance x-arm-2 for space robotics telepresence,” in *Proceedings of the IEEE/RSJ International Conference on Intelligent Robots and Systems (IROS)*, 2011, pp. 2158–2165.
- [30] Y. Mao, X. Jin, G. G. Dutta, J. P. Scholz, and S. K. Agrawal, “Human movement training with a cable driven arm exoskeleton (carex),” *IEEE Transactions on Neural Systems and Rehabilitation Engineering*, vol. 23, pp. 84–92, 2015.

- [31] M. Kaneko, M. Wada, H. Maekawa, and K. Tanie, "A new consideration on tendon-tension control system of robot hands," in *Proceedings of the IEEE International Conference on Robotics and Automation (ICRA)*, 1991, pp. 1028–1033.
- [32] G. Palli, G. Borghesan, and C. Melchiorri, "Modeling, identification, and control of tendon-based actuation systems," *IEEE Transactions on Robotics*, vol. 28, pp. 277–290, 2012.
- [33] V. Agrawal, J. Peine, and B. Yao, "Modeling of transmission characteristics across a cable-conduit system," *IEEE Transactions on Industrial Robotics*, vol. 26, pp. 914–924, 2010.
- [34] Q. Wu, X. Wang, L. Chen, and F. Du, "Transmission model and compensation control of double-tendon-sheath actuation system," *IEEE Transactions on Industrial Electronics*, vol. 62, pp. 1599–1609, 2015.
- [35] Facebook. (2018) Rift. [Online]. Available: <https://www.oculus.com/>
- [36] HTC. (2018) Vive. [Online]. Available: <https://www.vive.com/>
- [37] S. I. Entertainment. (2018) Playstationvr. [Online]. Available: <https://www.playstation.com/>
- [38] F. Brizzi, L. Peppoloni, A. Graziano, E. D. Stefano, C. A. Avizzano, and E. Ruffaldi, "Effects of augmented reality on the performance of teleoperated industrial assembly tasks in a robotic embodiment," *IEEE Transactions on Human-machine Systems*, vol. 48, pp. 197–206, 2018.
- [39] K. Theofilis, J. Orlosky, Y. Nagai, and K. Kiyokawa, "Panoramic view reconstruction for stereoscopic teleoperation of a humanoid robot," in *Proceedings of the IEEE-RAS International Conference on Humanoid Robots*, 2016, pp. 242–248.
- [40] M. Jagersand, A. Rachmielowski, D. Lovi, N. Birkbeck, A. Hernandez-Herdocia, A. Shademan, D. Cobzas, and K. Yerec, "Predictive display from computer vision models," in *Proceedings of the International Symposium on Artificial Intelligence, Robotics and Automation in Space*, 2010.
- [41] A. Zoss, H. Kazerooni, and A. Chu, "Biomechanical design of the berkeley lower extremity exoskeleton (BLEEX)," *IEEE/ASME Trans. Mechatronics*, vol. 11, pp. 128–138, 2006.
- [42] R. Riener, L. Lunenburger, S. Jezernik, M. Anderschitz, G. Colombo, and V. Dietz, "Patient-cooperative strategies for robot-aided treadmill training: first experimental results," *IEEE Trans. Neural Syst. Rehabil. Eng.*, vol. 13, pp. 380–394, 2005.

- [43] S. K. Banala, S. H. Kim, S. K. Agrawal, and J. P. Scholz, "Robot Assisted Gait Training With Active Leg Exoskeleton (ALEX)," *IEEE Trans. on Neural System Rehabilitation Engineering*, vol. 17, pp. 2–8, 2009.
- [44] J. F. Veneman, R. Kruidhof, E. E. Hekman, R. Ekkelenkamp, E. H. V. Asseldonk, and H. van der Kooij, "Design and Evaluation of the LOPES Exoskeleton Robot for Interactive Gait Rehabilitation," *IEEE Trans. on Neural System Rehabilitation Engineering*, vol. 15, pp. 379–386, 2007.
- [45] D. Wang, K.-M. Lee, J. Guo, and C.-J. Yang, "Adaptive Knee Joint Exoskeleton Based on Biological Geometries," *IEEE/ASME Trans. Mechatronics*, vol. 19, pp. 1268–1278, 2014.
- [46] P. Staubli, T. Nef, V. Klamroth-Marganska, and R. Riener, "Effects of intensive arm training with the rehabilitation robot armin ii in chronic stroke patients: four single-cases," *Journal of NeuroEngineering and Rehabilitation*, vol. 6, pp. 1–10, 2009.
- [47] N. G. Tsagarakis and D. C. Caldwell, "Development and control of a 'soft-actuated' exoskeleton for use in physiotherapy and training," *J. Autonomous Robots*, vol. 15, pp. 21–33, 2003.
- [48] E. Rocon, J. Belda-Lois, A. Ruiz, M. Manto, J. Moreno, and J. Pons, "Design and validation of a rehabilitation robotic exoskeleton for tremor assessment and suppression," *IEEE Transactions on neural systems and rehabilitation engineering*, vol. 15, pp. 367–378, 2007.
- [49] D. Reinkensmeyer, L. Kahn, M. Averbuch, A. McKenna-Cole, B. Schmit, and W. Rymer, "Understanding and treating arm movement impairment after chronic brain injury: progress with the arm guide," *J Rehabil Res Dev*, vol. 37, pp. 653–662, 2000.
- [50] B. R. Brewer, S. K. McDowell, and L. C. Worthen-Chaudhari, "Poststroke upper extremity rehabilitation : A review of robotic systems and clinical results," *Topics in stroke rehabilitation*, vol. 14, pp. 22–44, 2007.
- [51] M. Mihelj, T. Nef, and R. Riener, "ARMin II - 7 dof rehabilitation robot: mechanics and kinematics," in *Proceedings of the IEEE International conference on Robotics and Automation*, 2007, pp. 4120–4125.

- [52] M. Bergamasco, B. Allotta, L. Bosio, L. Ferretti, G. Parrini, G. Prisco, F. Salsedo, and G. Sartini, "An arm exoskeleton system for teleoperation and virtual environments applications," in *IEEE International Conference on Robotics and Automation*, 1994, pp. 1449–1454.
- [53] A. H. Stienen, E. E. Hekman, H. ter Braak, A. M. Aalsma, F. C. van der Helm, and H. van der Kooij, "Design of a rotational hydro-elastic actuator for an active upper-extremity rehabilitation exoskeleton," in *Proceedings of the 2nd Biennial IEEE/RAS-EMBS International Conference on Biomedical Robotics and Biomechatronics*, 2008, pp. 881–888.
- [54] C. Carignan and M. Liszka, "Design of an arm exoskeleton with scapula motion for shoulder rehabilitation," in *International Conference on Advanced Robotics*, 2005, pp. 524–531.
- [55] T. Nef and R. Riener, "Shoulder actuation mechanisms for arm rehabilitation exoskeletons," in *Proceedings of the 2nd Biennial IEEE/RAS-EMBS International Conference on Biomedical Robotics and Biomechatronics*, 2008, pp. 862–868.
- [56] J. Klein, S. Spencer, J. Allington, K. Minakata, E. Wolbrecht, R. Smith, J. E. Bobrow, and D. J. Reinkensmeyer, "Biomimetic orthosis for the neurorehabilitation of the elbow and shoulder (bones)," in *Proceedings of the 2nd Biennial IEEE/RAS-EMBS International Conference on Biomedical Robotics and Biomechatronics*, 2008, pp. 535–541.
- [57] A. Frisoli, F. Rocchi, S. Marcheschi, A. Dettori, F. Salsedo, and M. Bergamasco, "A new force-feedback arm exoskeleton for haptic interaction in virtual environments," in *Symposium on Haptic Interfaces for Virtual Environment and Teleoperator Systems*, 2005, pp. 195–201.
- [58] A. H. Stienen, E. E. Hekman, F. C. V. der Helm, G. B. Prange, M. J. Jannink, A. M. Aalsma, and H. V. der Kooij, "Dampace: dynamic force-coordination trainer for the upper extremities," in *Proceedings of the IEEE International Conference on Rehabilitation Robotics*, 2007, pp. 820–826.
- [59] L.-Q. Zhang, H.-S. Park, and Y. Ren, "Developing an intelligent robotic arm for stroke rehabilitation," in *Proceedings of the International Conference on Rehabilitation Robotics*, 2007, pp. 984–993.
- [60] T. Moeslund, C. Madsen, and E. Granum, "Modelling the 3d pose of a human arm and the shoulder complex utilizing only two parameters," *Integrated Computer-Aided Engineering*, vol. 12, pp. 159–175, 2005.

- [61] J. Cheng, S. Leung, B. Chiu, P. Tse, C. Lee, A. Chan, G. X. G, A. Leung, and Y. Xu, “Can we predict body height from segmental bone length measurements? a study of 3,647 children.” *J Pediatr Orthop.*, vol. 18, pp. 387–393, 1998.
- [62] B. Siciliano, L. Sciavicco, L. Villani, and G. Oriolo, *Robotics: Modeling, Planning and Control*. Springer, 2009.
- [63] L. Sciavicco and B. Siciliano, “A solution algorithm to the inverse kinematic problem for redundant manipulators,” *IEEE Journal of Robotics and Automation*, vol. 4, pp. 403–410, 1988.
- [64] W. B. Green and J. D. Heckman, *The clinical measurement of joint motion*. American Academy of Orthopaedic Surgeons, 1994.
- [65] J. Kiusalaas, *Numerical Methods in Engineering with MATLAB*. Cambridge university press, 2010.
- [66] D. Tolani, A. Goswami, and N. I. Badler, “Real-time inverse kinematics techniques for anthropomorphic limbs,” *Graphical Models*, vol. 62, pp. 353–388, 2000.
- [67] ATI Industrial Automation. (2014) Mini45. [Online]. Available: <http://www.ati-ia.com/>
- [68] NaturalPoint. (2014) s250e. [Online]. Available: <http://www.naturalpoint.com/optitrack/>
- [69] S. Ma, S. Hirose, and H. Yoshinada, “Design and experiments for a coupled tendon-driven manipulator,” *Control Systems, IEEE*, vol. 13, pp. 30–36, 1993.
- [70] M. Zinn, B. Roth, O. Khatib, and J. K. Salisbury, “A new actuation approach for human friendly robot design,” *The international journal of robotics research*, vol. 23, pp. 379–398, 2004.
- [71] P. Srl, *IH2 Azzurra*, 2015. [Online]. Available: <http://www.prensilia.com/>
- [72] B. Massa, S. Roccella, M. C. Carrozza, and P. Dario, “Design and development of an underactuated prosthetic hand,” *Proceedings of the IEEE International Conference on Robotics and Automation (ICRA)*, pp. 3374–3379, 2002.
- [73] M. C. Carrozza, G. Cappiello, S. Micera, B. B. Edin, L. Beccai, and C. Cipriani, “Design of a cybernetic hand for perception and action,” *Biological cybernetics*, vol. 95, pp. 629–644, 2006.

- [74] R. Conti, E. Meli, and A. Ridolf, “A novel kinematic architecture for portable hand exoskeletons,” *Mechatronics*, vol. 35, pp. 192–207, 2016.
- [75] H. Rifaï, S. Mohammed, W. Hassani, and Y. Amirat, “Nested saturation based control of an actuated knee joint orthosis,” *Mechatronics*, vol. 23, pp. 1141–1149, 2013.
- [76] Y. Kim, “Anthropomorphic low-inertia high-stiffness manipulator for high-speed safe interaction,” *IEEE Transactions on Robotics*, vol. 33, pp. 1358–1374, 2017.
- [77] K. Salisbury, W. Townsend, B. Ebrman, and D. DiPietro, “Preliminary design of a whole-arm manipulation system (WAMS),” in *Proceedings of the IEEE International Conference on Robotics and Automation (ICRA)*, 1988, pp. 254–260.
- [78] G. L. Smidt, “Biomechanical analysis of knee flexion and extension,” *Journal of biomechanics*, vol. 6, pp. 79–92, 1973.
- [79] L. J. Askew, K. An, B. F. Morrey, and E. Y. S. Chao, “Isometric elbow strength in normal individuals,” *Clinical orthopaedics and related research*, vol. 222, pp. 261–266, 1987.
- [80] B. Sofia, N. Anna, P. Eja, B. Ann, and T. Carina, “Relationship between finger flexion and extension force in healthy women and women with rheumatoid arthritis,” *Journal of rehabilitation medicine*, vol. 44, pp. 605–608, 2012.
- [81] N. Viteiello, T. lenzi, S. M. D. Rossi, S. Roccella, and M. C. Carrozza, “A sensorless torque control for antagonistic driven compliant joints,” *Mechatronics*, vol. 20, pp. 355–367, 2010.
- [82] B. Vanderborght, N. G. Tsagarakis, R. B. Ham, I. Thorson, and D. G. Caldwell, “Maccepa 2.0: compliant actuator used for energy efficient hopping robot chobino1d,” *Autonomous Robotics*, vol. 31, pp. 55–65, 2011.
- [83] T. Lens, J. Kunz, and O. von Stryk, “Biorob-arm: A quickly deployable and intrinsically safe, light-weight robot arm for service robotics applications.” *International Symposium on Robotics (ISR)*, pp. 905–910, 2010.
- [84] M. Grebenstein, M. Chalon, W. Fried, S. Haddadin, T. Wimböck, G. Hirzinger, and R. Siegwart, “The hand of the dlr hand arm system: Designed for interaction,” *The International Journal of Robotics Research*, vol. 31, pp. 1531–1555, 2012.

- [85] U. Jeong, H. In, H. Lee, , B. B. Kang, and K. Cho, “Investigation on the control strategy of soft wearable robotic hand with slack enabling tendon actuator,” *Proceedings of the IEEE International Conference on Robotics and Automation (ICRA)*, pp. 5004–5009, 2015.
- [86] L. Cappello, D. K. Binh, S. Yen, and L. Masia, “Design and preliminary characterization of a soft wearable exoskeleton for upper limb.” *Proceedings of IEEE RAS/EMBS International Conference on Biomedical Robotics and Biomechanics (BioRob)*, pp. 623–630, 2016.
- [87] R. Walkler, “Developments in dextrous hands for advanced robotic applications,” *Proceedings of the Sixth Biannual World Automation Congress*, pp. 123–128, 2004.
- [88] A. Chiri, N. Vitiello, F. Giovacchini, and S. Roccella, “Mechatronic design and characterization of the index finger module of a hand exoskeleton for post-stroke rehabilitation,” *IEEE/ASME Transactions on Mechatronics*, vol. 17, pp. 884–894, 2012.
- [89] H. In and K. Cho, “Jointless structure and under-actuation mechanism for compact hand exoskeleton,” *Proceedings of the IEEE International Conference on Rehabilitation Robotics (ICORR)*, pp. 1–6, 2011.
- [90] N. Hogan, “Impedance control: An approach to manipulation: Part I - theory, part II - implementation, part III - applications,” *Journal of dynamic systems, measurement, and control*, vol. 107, pp. 1–24, 1985.
- [91] K. Kong, J. Bae, and M. Tomizuka, “Control of rotary series elastic actuator for ideal force-mode actuation in human-robot interaction applications,” *IEEE/ASME Trans. Mechatron.*, vol. 14, pp. 105–118, 2009.
- [92] J. Bae, K. Kong, and M. Tomizuka, “Gait phase-based control for a rotary series elastic actuator assisting the knee joint,” *ASME Journal of Medical Devices*, vol. 5, p. 031010, 2011.
- [93] J. E. Pratt, B. T. Krupp, C. J. Morse, and S. H. Collins, “The roboknee: an exoskeleton for enhancing strength and endurance during walking,” *Proceedings of the IEEE International Conference on Robotics and Automation (ICRA)*, pp. 2430–2435, 2004.
- [94] D. Ragonesi, S. Agrawal, W. Sample, and T. Rahman, “Series elastic actuator control of a powered exoskeleton,” *Annual International Conference of the IEEE EMBS*, pp. 3515–3518, 2011.

- [95] F. E. Zajac, “Muscle and tendon: properties, models, scaling, and application to biomechanics and motor control,” *Critical reviews in biomedical engineering*, vol. 17, pp. 359–411, 1989.
- [96] H. Lee and M. Tomizuka, “Robust motion controller design for high-accuracy positioning systems,” *IEEE Trans. Ind. Electronics*, vol. 43, pp. 48–55, 1996.
- [97] P. D. Neilson, “Speed of response or bandwidth of voluntary system controlling elbow position in intact man,” *Medical and Biological Engineering*, vol. 10, pp. 450–459, 1972.
- [98] M. Tomizuka, “Zero phase error tracking algorithm for digital control,” *Journal of Dynamic Systems, Measurement, and Control*, vol. 109, pp. 349–354, 1987.
- [99] Kinova. (2015) Mico. [Online]. Available: <http://www.kinovarobotics.com/>
- [100] P. Agarwal, J. Fox, Y. Yun, and M. K. O’Malley, “An index finger exoskeleton with series elastic actuation for rehabilitation: Design, control and performance characterization,” *The International Journal of Robotics Research*, vol. 34, pp. 1747–1772, 2015.
- [101] T. L. Nguyen, S. J. Allen, and S. J. Phee, “Direct torque control for cable conduit mechanisms for the robotic foot for footwear testing,” *Mechatronics*, vol. 51, pp. 197–149, 2018.
- [102] K. Kong, J. Bae, and M. Tomizuka, “Torque mode control of a cable-driven actuating system by sensor fusion,” *ASME Journal of Dynamic Systems, Measurement, and Control*, vol. 135, p. 031003, 2013.
- [103] S. J. Phee, S. C. Low, Z. L. Sun, K. Y. Ho, W. M. Huang, and Z. M. Thant, “Robotic system for no-scar gastrointestinal surgery,” *The International Journal of Medical Robotics and Computer Assisted Surgery*, vol. 4, pp. 15–22, 2008.
- [104] T. N. Do, T. Tjahjowidodo, M. W. S. Lau, and S. J. Phee, “Position control of asymmetric nonlinearities for a cable-conduit mechanism,” vol. 14, pp. 1515–1523, 2017.
- [105] ———, “Nonlinear friction modelling and compensation control of hysteresis phenomena for a pair of tendon-sheath actuated surgical robots,” *Mechanical Systems and Signal Processing*, vol. 60-61, pp. 770–784, 2015.
- [106] H. Olsson, K. J. Astrom, C. C. de Wit, M. Gafvert, and P. Lischinsky, “Friction models and friction compensation,” *European Journal of Control*, vol. 4, pp. 176–195, 1998.

- [107] Z. Zhang, Q. Xue, W. Liu, and W. Shen, “Friction and wear behaviors of several polymers under oil-lubricated conditions,” vol. 68, pp. 2175–2182, 1998.
- [108] Y. Park, I. Jo, J. Lee, and J. Bae, “A wearable hand system for virtual reality,” in *Proceedings of the IEEE/RSJ International Conference on Intelligent Robots and Systems (IROS)*, 2017, pp. 1052–1057.
- [109] K. Ohishi, K. Ohnishi, and K. Miyachi, “Torque–speed regulation of dc motor based on load torque estimation method,” in *Proceedings of the IEEJ International Power Electronics Conference*, 1983, pp. 1209–1218.
- [110] L. Yi and M. Tomizuka, “Two-degree-of-freedom control with robust feedback control for hard disk servo systems,” *IEEE/ASME Transactions on Mechatronics*, vol. 4, pp. 17–24, 1999.
- [111] D. A. Winter, *Biomechanics and Motor Control of Human Movement*. Wiley, 2009.
- [112] J. Lim, I. Lee, I. Shim, H. Jung, H. Joe, H. Bae, O. Sim, J. Oh, T. Jung, S. Shin, K. Joo, M. Kim, K. Lee, Y. Bok, D. Choi, B. Cho, S. Kim, J. Heo, I. Kim, J. Lee, I. Kwon, and J. Oh, “Robot system of drc-hubo+ and control strategy of team kaist in darpa robotics challenge finals,” *Journal of Field Robotics*, vol. 34, pp. 802–829, 2017.
- [113] S. Yi, S. G. McGill, L. Vadakedathu, Q. He, I. Ha, H. S. J. Han, M. Rouleau, B. Zhang, D. Hong, M. Yim, and D. D. Lee, “Team thor’s entry in the darpa robotics challenge trials 2013,” *Journal of Field Robotics*, vol. 32, pp. 315–335, 2015.
- [114] M. Johnson, B. Shrewsbury, S. Bertrand, D. Calvert, T. Wu, D. Duran, D. Stephen, N. Mertins, J. Carff, W. Rifenburg, J. Smith, C. Schmidt-Wetekam, D. Faconti, A. Graber-Tilton, N. Eyssette, T. Meier, I. Kalkov, N. P. T. Craig, G. W. S. McCrory, B. Layton, P. Neuhaus, and J. Pratt, “Team ihmc’s lessons learned from the darpa robotics challenge: Finding data in the rubble,” *Journal of Field Robotics*, vol. 34, pp. 241–261, 2017.
- [115] S. Gray, R. Chevalier, D. Kottfis, B. Caimano, K. C. II, A. Rubin, and K. Fregene, “An architecture for human-guided autonomy: Team trooper at the darpa robotics challenge finals,” *Journal of Field Robotics*, vol. 34, pp. 852–873, 2017.
- [116] FLIR. (2018) Flea3. [Online]. Available: <https://www.flir.com/>

[117] E. C. Edwards, "Method and system for time/motion compensation for head mounted displays," Canada Patent 7 312 766, Dec. 25, 2007.

Acknowledgements

I would like to express deep appreciation to my advisor, Professor Joonbum Bae. It was the greatest fortune in my academic life to research under his guidance. His knowledge and passion in research was a great role model to me. This dissertation could not be realized without his valuable advice and support.

I deeply grateful to my dissertation committee members: Professor Hungsun Son, Professor Hyondong Oh, Professor Gwanseob Shin and Professor Tsz-Chiu Au. Their valuable comments improved the quality of this dissertation.

My special thanks go to Bio-Robotics and Control (BiRC) Laboratory members. Especially thanks to tele-operation research group members: Sungman Park, Junsoo Kim and Kyutaek Han. I also express thanks to all current and former BiRC Lab members: Inseong Jo, Jihoon Kim, Suin Kim, Younkyu Park, Jeongsoo Lee, Bokeon Kwak, Hoyeon Yeom, Dr. Dang Xuan Ba, Wookeun Park, Minhyuk Lee, Hyeonjun Kim, Dahee Jeong, Inkyu Lee, Hongwoo Park, Dongyoung Lee, Sungmin Seo, Heeyeop Kim, Jeongsoon Hong, and all others. I could get many ideas from discussions with BiRC members. I hope we all can contribute to humankind's happiness with the experiences in BiRC Laboratory.

I wish to express my sincere gratitude to my friends in UNIST. Special thanks go to Jungwoo Heo, Hochur Lee, Joonghwan Jeong, Seongeun Choi, for their supports and encouragements in hard times. I would also like to thank all my old friends.

I express my thanks to UNIST Design & Manufacturing Center members for advice on manufacturing techniques. Especially thanks to Kang-uk Kwon, Jin-sik Kim and Jae-hoon Cha.

I would also like to thank the National Research Foundation of Korea (NRF) for its support with Global Ph.D. Fellowship during my study in UNIST. Its financial support made me focus on research.

Lastly, I wish to thank my family, Gun Yong Jung, Miyeong Bak, Yeonghun Jung, for their love and support.

